INVESTIGATION ON THE CAPABILITIES OF SMART TRANSFORMER ON POWER DISTRIBUTION SYSTEMS

A THESIS

submitted by

HRISHIKESAN V M

for the award of the degree

of

DOCTOR OF PHILOSOPHY

DEPARTMENT OF ELECTRONICS AND ELECTRICAL ENGINEERING

INDIAN INSTITUTE OF TECHNOLOGY GUWAHATI, GUWAHATI, INDIA

APRIL 2021

To My Mother

THESIS CERTIFICATE

This is to certify that the thesis entitled **"INVESTIGATION ON THE CAPABILITIES OF SMART TRANSFORMER ON POWER DISTRIBUTION SYSTEMS"** submitted by **HRISHIKESAN V M** to the Indian Institute of Technology Guwahati, Guwahati, India for the award of the degree of Doctor of Philosophy is a bonafide record of the research work done by him under my supervision. The contents of this thesis, in full or in parts, have not been submitted to any other Institute or University for the award of any degree or diploma.

Place: Guwahati
Date: 09.04.2021

Dr. Chandan Kumar
Research Guide
Assistant Professor
Department of Electronics and Electrical Engineering
IIT-Guwahati, 781 039

ACKNOWLEDGEMENTS

I take this opportunity to acknowledge my heartfelt gratitude to all those people who directly or indirectly helped me to carry out this research work successfully.

I am heartily thankful to my supervisor, Dr. Chandan Kumar, for the encouragement, guidance and support during my research work. I express my gratitude for his willingness to help and timely advices on the issues I faced during the doctoral studies.

I also acknowledge Visvesaraya PhD scheme for selecting me as a research scholar under "Visvesvaraya PhD Scheme, MeitY, Govt. of India MEITY-PHD-1228" and supporting me technically and financially. I express my gratitude to the ASEAN-India collaborative research project entitled "Design, control and management of distributed generation in microgrid", and grant "ECR/2017/001564" under Science & Engineering Research Board (SERB) for providing technical and financial support during my research days.

I would like to acknowledge the financial, academic and technical support of the Indian Institute of Technology Guwahati for this research. I am thankful to the Heads of the Department during the course of my study. I am sincerely grateful to Dr. Praveen Tripathy, Dr. Sanjib Ganguly, and Dr. Ravindranath Adda, for assessing the work and giving invaluable suggestions as members of Doctoral Committee. I also thank Dr. H B Gooi, Dr. Saad Mekhilef, and Prof. Marco Liserre for their technical advice on the various issues.

Also, I would like to thank Dr. M.P. Selvan of National Institute of Technology Trichy for his constant support.

I would like to express gratitude to the services being offered by Mr. Paban Bujor Barua, Mr. Rakesh Singha, staff of power electronics laboratory and Mr. Mukut Baruah, and Mr. Dasarath Das, office staff of Electronics and Electrical Engineering department.

The Smart Energy Conversion group members have contributed immensely to my personal and professional time during my stay in the institute. I especially thank Dwijasish

Das, Sourav Kumar Ghosh and Anup Kumar Deka for their valuable help during my research. I am extremely thankful for the support extended by the friends Manokumar R, Arunima Dutta, Devendra Kumar, Ravi Kumar Gaddala, Gaurav Gautam, Manoranjan, Abhishek Paikray, Pramit Nandi and all my other friends from Power and Control Lab II.

I am thankful to my friends Jiss J Nallikuzhy, Vasudevan, Vivek Lukose, Dileep, Vijith, Christy, Sandeep, Sonu, Anoop, Sajith, Arun Mathew, Vishnu, Thomas, Mathew, Naveen, Aswathy, Jith, Gadha, Riya, Abhjith, Faizal, Kiran, Nikhil V, Akhil, Shahabaz, Subhash, Manu, Rafi, Rishi Shreedhar, Gokul, Aneez, Vyzakh, Ashmil, Ranchal, Amarjith, Aswani, Arun, Albert, Suvin, Piyoosh, Sreejith Muralidhar, Sagar, Sachin, Maneesh, Nithin P, Abhijith, Tahir, Adil, Hrishi, Shibili, Manoj, Richu and all other friends of malayali community for sharing beautiful moments during my life in IIT Guwahati.

I am also grateful to the professors of malayali community Dr. A. Rajesh, Dr. Benny George K, Dr. Ganesh Natarajan, Dr. Ravi K, Dr. Vibin Ramakrishnan, Dr. Suresh Kartha, Dr. Tony Jacob, and their families.

Many thanks to my parents, for always encouraging me to pursue my dreams. I thank my sister Chithra, brother Hari and my late grandfather for their loving care and support all these years. Last but not the least I would like to thank my partner Parvathy who always stayed at my side with unceasing love and care.

Hrishikesan V M

ABSTRACT

KEYWORDS: Smart transformer (ST); solid-state transformer (SST); voltage support; meshed hybrid microgrid.

The power distribution system is under major transformation due to the increased integration of renewable energy sources (RESs) and electric vehicles (EVs). Major challenges due to this transformation are: voltage magnitude variations, limited load and generation hosting capability of distribution system, operation and control of islanded and grid-connected microgrids, intermittent power production from RESs, current and voltage harmonics, increased fault currents, varying demand characteristics of loads, etc. These problems are addressed using the solutions such as transformer on-load tap changer (OLTC), enhanced control of distributed generation (DG) sources, AC/DC hybrid distribution grids, and custom power devices like distribution static compensator (DSTATCOM), dynamic voltage restorer (DVR), unified power quality conditioner (UPQC), etc. The OLTCs are having a limited range of operation, whereas integrating extra control in DG converters increases the complexity of the operation. Effectiveness of custom power device operation largely depends on the grid parameters. Due to all these factors, researchers have identified the need for a central controller in the distribution grid for the continuous and reliable operation.

Solid-state transformer (SST), which is a power electronic-based transformer, is gaining attraction in power distribution system. An SST with intelligent control integration is termed as a smart transformer (ST), and it can function as a central controller in distribution grid. A three-stage ST is best suited in the distribution grid applications due to the availability of DC links at medium voltage (MV) and low voltage (LV) levels. The ST can perform voltage transformation operation similar to conventional power transformer (CPT). In addition, it can maintain balanced sinusoidal voltages at the ST LVAC terminal and balanced sinusoidal unity power factor currents at the ST MVAC terminal. Since the CPT is a high efficient and simple solution to voltage transformation, its replacement with ST can only be justified with the more ancillary services that ST can

offer in the distribution grid.

Voltage variations are considered to be critical problem in the distribution system. The reactive power injection capability of ST MV converter is useful for voltage support. Enhancing the reactive power injection capacity improves the impact of ST in MVAC grid. This thesis proposes a method to coordinate the operation of ST LV converter and battery energy storage system (BESS) during MVAC grid voltage sag and swell. The coordinated operation improves the voltage support from ST with a lower-rated BESS. Further to the operation during voltage sag and swell, the load and generation hosting capability of a power distribution system is often restricted by the voltage limit violations. The hosting capacity enhancement of radial distribution grid helps for accommodating more RES and loads. Moreover, along with the reactive power support, the ST with BESS integration has the capability to exchange the active power with the MVAC grid. This thesis proposes a sensitivity based ST and BESS sizing method to improve the load and generation hosting capacity of a distribution grid. The method is proposed with the capability to achieve the desired hosting capability with active and reactive power support independently or with a flexible combination of both. The proposed method can be adapted to improve the hosting capability of any distribution grid irrespective of the nature of grid impedance. Another aspect requiring immediate attention is the power management capability of a distribution system. This is important to achieve better reliability and operational flexibility. The hybrid distribution grids are gaining attraction due to their improved reliability and enhanced power management capability. The MVDC based distribution systems are suitable for the establishing hybrid grids, and ST's MVDC links are capable of forming MVDC interconnections. An MVDC based meshed hybrid microgrid is proposed using ST, and the operation is analyzed in different grid conditions. The MVAC grid and ST MV converter failure conditions are analyzed in this configuration and enhanced operational freedom is achieved for the proposed system. The performance of the system is compared with the existing topologies to show its advantages. In addition, the operation of this system with the integrated BESS is studied during adverse grid operating conditions. The peak loading, peak generation and MVAC voltage sag conditions are analyzed. The proposed method provides an improved power management solution. It flattens the load curve by managing the spikes in the load curve. The voltage rise conditions are avoided using the reverse power flow control. The continuous operation during MVAC voltage sags

improves the reliability of power supply to the LVAC loads. All the operations are validated in the simulation environment. In addition, an experimental prototype is built in the laboratory, and all the proposed methods are tested.

TABLE OF CONTENTS

LIST OF TABLES

LIST OF FIGURES

ABBREVIATIONS

AC	Alternating Current
ADC	Analogue to Digital Converter
APF	Active Power Filter
BESS	Battery Energy Storage System
BTB	Back-To-Back
CPD	Custom Power Device
CPT	Conventional Power Transformer
DAC	Digital to Analogue Converter
DC	Direct Current
DER	Distributed Energy Resource
DG	Distributed Generation
DSTATCOM	Distribution Static Compensator
DAB	Dual Active Bridge
DVR	Dynamic Voltage Restorer
EV	Electric Vehicle
IEEE	Institute of Electrical and Electronics Engineers
IGBT	Insulated Gate Bipolar Transistor
LEF	Lead Element Filter
LV	Low Voltage
MAB	Multiple Active Bridge
MV	Medium Voltage
NPC	Neutral Point Clamped
OLTC	On-Load Tap Changer
PCC	Point of Common Coupling
PET	Power Electronic Transformer
PI	Proportional Integral
PLL	Phase Locked Loop
PSCAD	Power System Computer Aided Design

PQ	Power Quality
PV	Photovoltaic
RES	Renewable Energy Source
rms	Root Mean Square
SR	Series Resonant
SST	Solid-State Transformer
ST	Smart Transformer
SOC	State of Charge
SVC	Static Var Compensator
THD	Total Harmonic Distortion
UPQC	Unified Power Quality Conditioner
VSI	Voltage Source Inverter

NOTATIONS

C_{lv}, C_{lv1}, C_{lv2}	ST LV converter AC filter capacitor value
C_{lv-dc}, C_{lv-dc1}, C_{lv-dc2}	ST LVDC capacitor value
C_{mv}, C_{mv1}, C_{mv2}	ST MV converter AC filter capacitor value
C_{mv-dc}, C_{mv-dc1}, C_{mv-dc2}	ST MVDC capacitor value
f_{dc}	ST DC-DC converter switching frequency
f_{sw}	Switching frequency
i_{dmv}, i_{qmv}	Instantaneous ST MV converter AC currents in $d-q$ reference frame
i^*_{dmvr}	Instantaneous d component ST MV converter AC reference current for LVAC active power transfer
i^*_{dmv}, i^*_{qmv}	Instantaneous ST MV converter AC reference currents in $d-q$ reference frame
i_{lva}, i_{lvb}, i_{lvc}	Instantaneous ST LVAC currents in phase-a, b and c, respectively
i_{lva1}, i_{lvb1}, i_{lvc1}	Instantaneous ST-1 LVAC currents in phase-a, b and c, respectively
i_{lva2}, i_{lvb2}, i_{lvc2}	Instantaneous ST-2 LVAC currents in phase-a, b and c, respectively
i_{mva}, i_{mvb}, i_{mvc}	Instantaneous ST MV converter AC currents in phase-a, b and c, respectively
i_{mva1}, i_{mvb1}, i_{mvc1}	Instantaneous ST-1 MV converter AC currents in phase-a, b and c, respectively
i_{mva2}, i_{mvb2}, i_{mvc2}	Instantaneous ST-2 MV converter AC currents in phase-a, b and c, respectively
i^*_{mva}, i^*_{mvb}, i^*_{mvc}	Instantaneous ST MV converter AC reference currents in phase-a, b and c, respectively
i^*_{mva1}, i^*_{mvb1}, i^*_{mvc1}	Instantaneous ST-1 MV converter AC reference currents in phase-a, b and c, respectively

i^*_{mva2}, i^*_{mvb2}, i^*_{mvc2}	Instantaneous ST-2 MV converter AC reference currents in phase-a, b and c, respectively
$i^*_{mv\alpha(p)}$, $i^*_{mv\beta(p)}$	Instantaneous ST MV converter AC reference currents for active power transfer in $\alpha-\beta$ reference frame
$i^*_{mv\alpha(q)}$, $i^*_{mv\beta(q)}$	Instantaneous ST MV converter AC reference currents for reactive power transfer in $\alpha-\beta$ reference frame
$i^*_{mv\alpha}$, $i^*_{mv\beta}$	Instantaneous ST MV converter AC reference currents in $\alpha-\beta$ reference frame, respectively
I_b	BESS current
I_{mv1-r}	ST-1 MV converter rms current rating
K_{p-dc}, K_{i-dc}	ST DC-DC converter PI controller proportional and integral constants, respectively
K_{p-l}, K_{i-l}	MVDC link PI controller proportional and integral constants, respectively
K_{p-q}, K_{i-q}	Reactive power requirement PI controller proportional and integral constants, respectively
k_l	Control constant for ST-1 MV converter
k_{tr}	Control constant for MVDC active power loss
k_{Q1}, k_{Q2}	Control constant for reactive power transfer for ST-1 and ST-2 MV converters, respectively
L_b	BESS converter inductor value
L_{dc}	ST DC-DC converter inductor value
L_{lv}, L_{lv1}, L_{lv2}	ST LV converter AC filter inductor value
L_{mv}, L_{mv1}, L_{mv2}	ST MV converter AC filter inductor value
M_{pd}	Slope factor for active power
M_{qd}	Slope factor for reactive power
n	ST LV converter voltage control index
ΔP_{bi}	Change in bus-i active power
ΔP_{b4}	Change in bus-4 active power
ΔP_{b4-max}	Maximum active power change required in bus-4
$\Delta P_{loss-perc}$	Percentage reduction in losses
P^*_b	BESS power reference
P_b	Power supplied from BESS

P_{b4l}	Bus-4 LVAC active power loading
P_{b-mod}	Modified power rating of BESS
P_{dc-dc}	Power transferred between ST MVDC and LVDC links
P_{dc-rat}	Rating of ST DC-DC converter
P_{dc-lim}	Maximum MVDC power limit
P_{dc}	MVDC power transferred
P^*_{dc}	MVDC power transfer reference
P^*_{loss}, P^*_{loss1}, P^*_{loss2}	ST MVDC link power loss component
$P^*_{loss-ac}$	Active power loss on MVAC line
$P^*_{loss-dc}$	Active power loss on MVDC line
P_{lv}	ST LVAC active power
P_{li}	Active power load on bus-i
P_{llv1}	Active power loading on ST-1 LVAC bus
P_{llv2}	Active power loading on ST-2 LVAC bus
P_{glv1}	Active power generation on microgrid LVAC bus
$P_{lv1-net}$	Net active power loading on microgrid LVAC bus
P_{lv1-ll}	Predefined active power lower limit
P_{lv1-ul}	Predefined active power upper limit
P_{lv1-pv}	Active power generation from PV
P_{g1-net}	Net active power import in microgrid MVAC bus
P_{lv-mod}	Modified ST LVAC active power
P_{g1-lim}	Predefined active power export limit
P^*_{lv}	ST LVAC active power reference
P_{lv-max}	Maximum active power loading on ST LV converter
P_{opr}	Predefined active power operating point
P_{mv}	ST MV converter active power loading
P^*_{mv}, P^*_{mv1}, P^*_{mv2}	ST MV converter active power reference
P_{mv-lim}	ST MVAC active power limit
P_{mv-mod}	Modified ST MV converter reactive power capability
P_{mv-rat}	Active power rating of ST MV converter
P_{mv1-rn}, S_{mv1-rn}	ST-1 MV converter active and apparent power ratings, respectively
P_{mv1-rs}, S_{mv1-rs}	ST-1 MV converter active and apparent power ratings,

	respectively during sag
$P_{peak-lim}$	Predefined peak demand limit
P_t	Inter-feeder power transfer
$Q_{cap-perc}$	Percentage reactive power capability
ΔQ_{bi}	Change in bus-i reactive power
ΔQ_{b4}	Change in bus-4 reactive power
ΔQ_{b4-max}	Maximum reactive power change required in bus-4
Q_{DG1}, S_{DG1}	DG reactive and apparent powers
Q_{tot1}	Total reactive power availability
Q_{li}	Reactive power load on bus-i
Q_{mv}	ST MV converter reactive power loading
Q_{mv1}	ST-1 MV converter reactive power availability
Q^*_{mv}, Q^*_{mv1}, Q^*_{mv2}	ST MV converter reactive power reference
Q_{mv-req}	ST MV converter reactive power requirement
Q_{mv-lim}	ST MV converter reactive power limit
Q_{mv-mod}	Modified ST MV converter reactive power capability
R_{dcij}	DC Line resistance in Ohms per kilometre
R_{acij}	AC Line resistance in Ohms per kilometre
R_{mv}	Value of the ST MV converter damping resistance
R_s	Value of the MVAC grid resistance
S_{mv}, $S_{mv1-rat}$	ST MV converter apparent power rating
S_{BTB1}	Apparent power rating of BTB converter
V_b	BESS voltage
v_{b4a}, v_{b4b}, v_{b4c}	Instantaneous bus-4 voltage
	in phase-a, b and c, respectively
v_{bd4}, v_{bq4}	Instantaneous bus-4 voltage in $d-q$ reference frame
V_{b4-ll}	Specified lower limit of voltage magnitude
V_{b4}	Actual bus-4 voltage magnitude
V_{bill}	Bus-i voltage (L-L)
V_{dci}	MVDC link of ST-i
V_{g1-n}	Microgrid MVAC nominal rms voltage (L-L)
V_{g1-s}	Microgrid MVAC nominal rms voltage during sag (L-L)
v_{lva}, v_{lvb}, v_{lvc}	Instantaneous ST LV converter AC terminal voltage

	in phase-a, b and c, respectively
v_{lva1}, v_{lvb1}, v_{lvc1}	Instantaneous ST-1 LV converter AC terminal voltage
	in phase-a, b and c, respectively
v_{lva2}, v_{lvb2}, v_{lvc2}	Instantaneous ST-2 LV converter AC terminal voltage
	in phase-a, b and c, respectively
v^*_{lva}, v^*_{lvb}, v^*_{lvc}	Instantaneous ST LV converter reference voltages
	in phase-a, b and c, respectively
V_{lv}	Magnitude of ST LV converter terminal voltage
V^*_{lv}	Magnitude of ST LV converter reference terminal voltage
V_{lv-nom}	Magnitude of nominal ST LV converter terminal voltage
V_{lv-dc}, V_{lv-dc1}, V_{lv-dc2}	ST LVDC link voltage
V^*_{lv-dc}, V^*_{lv-dc1}, V^*_{lv-dc2}	Reference ST LVDC link voltage
V_{mv-dc}, V_{mv-dc1}, V_{mv-dc2}	ST MVDC link voltage
V^*_{mv-dc}, V^*_{mv-dc1}, V^*_{mv-dc2}	Reference ST MVDC link voltage
$\overline{V}_g$	MVAC grid voltage
V_g	Rms value of MVAC grid voltage
V_{g1-n}	Rms value of nominal microgrid MVAC voltage
V_{g1-s}	Rms value of microgrid MVAC voltage during sag
$\overline{V}_t$	MVAC PCC voltage
V_t	Rms value of MVAC PCC voltage
V^*_t	Rms value of reference MVAC PCC voltage
v^*_{mva}, v^*_{mvb}, v^*_{mvc}	Instantaneous ST MV reference voltages
	in phase-a, b and c, respectively
v_{ta}, v_{tb}, v_{tc}	Instantaneous MVAC PCC voltages
	in phase-a, b and c, respectively
v_{ta1}, v_{tb1}, v_{tc1}	Instantaneous fundamental MVAC PCC voltages
	in phase-a, b and c, respectively
$v_{t\alpha}$, $v_{t\beta}$	Instantaneous fundamental MVAC PCC voltages
	in $\alpha - \beta$ reference frame
ΔV_{b4}	Change in bus-4 voltage magnitude
ΔV_{b4-max}	Maximum deviation in bus-4 voltage magnitude
X_s	Value of the MVAC grid reactance

Greek Symbols

δ	Phase angle between grid and PCC voltages
δ^*_{dc-dc}, δ^*_{dc-dc1}, δ^*_{dc-dc2}	ST DC-DC converter reference phase angle
δ^*_b	BESS converter reference phase angle
ω	Fundamental frequency of the supply voltages in rad/sec

CHAPTER 1

INTRODUCTION

1.1 EVOLUTION OF POWER SYSTEMS

Electric power system and grid configuration are under drastic transformation in recent times. From a large centralized grid, the power system is moving towards a smaller decentralized grid with new control features [1]–[3]. This shift is driven by the increased attraction towards environment-friendly renewable energy-based generating stations instead of fossil fuel-based bulk generating plants. The non-conventional energy sources such as wind and solar photovoltaic (PV) based power plants are geographically distributed in nature. Generating stations established to harvest energy from these sources are typically termed as distributed generation (DG) plants [4], [5]. On the other side, the impact of battery energy storage systems (BESSs) on the power system is also increasing due to the improved technological advancements in this sector [6]. Another major shift is happening in the transportation industry. Fossil fuel-based locomotives and conventional transportation options are moving over to the electric vehicle (EV) technologies [7]. These changes in load and generation modified the conventional unidirectional power flow in a power distribution system to a multi-directional one. Moreover, the concept of microgrids is gaining attraction because of its operational flexibility in islanded and grid-connected mode of operations. The geographical proximity of DGs and loads in microgrids reduces the line losses for power transfer. However, the stable operation of microgrids require enhanced active and reactive power control measures [8], [9]. As a consequence of these transformations, the power distribution system's challenges have also increased exponentially.

1.1.1 Challenges in the Modern Power Distribution Systems

The stable and reliable operation of a power distribution system is essential under any operating conditions. Few of the challenges arising due to the structural changes in the power distribution system are listed as follows.

- Voltage magnitude fluctuations [10]
- Limited load and generation hosting capacity of existing distribution system [11]
- Operation and control of islanded and grid-connected microgrids [12]
- Intermittent power production by renewable energy sources (RESs) [13]
- Varying load demand characteristics [14]
- Increased fault current [15]
- Effect of harmonics [16]
- Charging dynamics of EVs [17]

Out of the various challenges mentioned above, the voltage magnitude variations are considered to be an important and frequently occurring issue that affect the normal operation of distribution system. The presence of DG in the distribution system may introduce voltage magnitude variations due to the uncontrolled reverse power flow [3], [18]. The voltage rise primarily occurs during peak DG injection times, and the regulation of the active power injection leads to the under-utilization of the RESs. However, DG operators are forced to control the active power injection in order to follow the voltage magnitude limits imposed by the grid operators [19]. The voltage rise in distribution grids can lead to permanent damage for the connected equipment in the system. The rural distribution feeders are more vulnerable to the voltage rise related issues due to their long span. In a distribution grid with PV installed houses, the feeder and the transformer impedance play a critical role in determining the rate of voltage rise [20]. The quantification of the adverse effects of high PV penetration is important for evaluating the performance of the distribution system. In Fig. 1.1, the voltage profile of a 13-bus system with and without PV penetration is shown [21]. The voltage magnitudes are well-within the limits without PV penetration as shown in Fig. 1.1(a). However, the voltage rise is visible in Fig. 1.1(b) for the PV integrated system. This case shows the impact of PV penetration on distribution system voltage profiles.

Similar to voltage rise, the voltage sags are another critical issue in the distribution system. Voltage sags are usually caused by the faults occurring in different parts of the

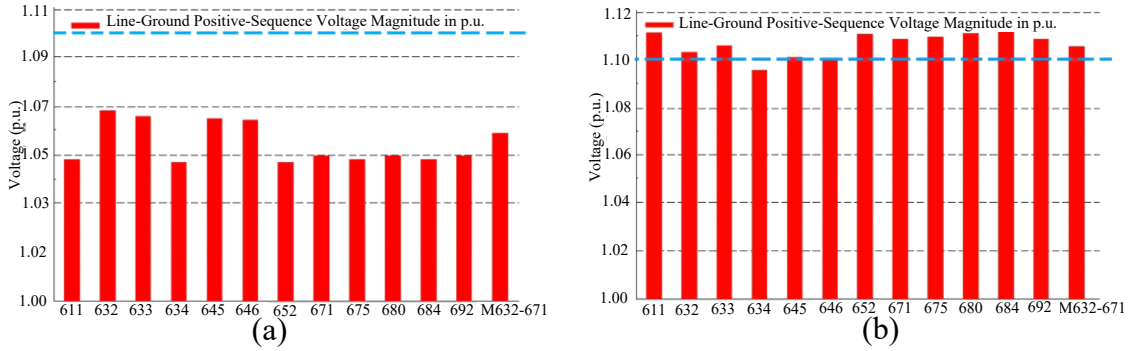

Fig. 1.1 Voltage profile of the modified 13-bus system. (a) Without PV generation. (b) With PV generation [21].

system [22]. Under-voltage magnitudes affect the performance of the connected equipment and the protection systems may force the disconnection of the equipment from the electrical network. As per the latest grid codes, the DG converters need to be controlled to ride through the low-voltage conditions [23]–[25]. The presence of EV loads introduce a stochastic nature of loading pattern in the distribution system. The uncontrolled EV charging during peak load conditions can cause unwanted load current variations, and voltage magnitude can fluctuate below the allowable limit [26]–[28]. Uncoordinated charging of EV batteries cause larger voltage deviations in the distribution grid. Charging of EV during evening hours increases the voltage drop in the system and can lead to lower voltage magnitudes at different buses. The voltage variations occurring in one side of conventional power transformer (CPT) will propagate to the other side and causes problems in the different parts of the distribution system, since it provides very limited isolation to the voltage disturbances. Such adverse effects of EV charging on distribution system are reported in [28]. The impact of voltage profile due to the uncoordinated EV charging is shown in Fig. 1.2. A random uncoordinated EV charging is simulated in the distribution system for different penetration levels of EV, and the voltage profiles of worst affected nodes are shown. As the penetration of EV increases, the voltage deviates more than the allowable limits during 1800 h to 2100 h as seen in the Fig. 1.2.

Another important aspect is hosting capacity. Hosting capability is defined as the total load or DG capacity that can be accommodated in a distribution system without the violation of operational parameter limits [29]. The hosting capability of a distribution system is often limited by the loading on the CPTs and distribution lines, and voltage limit violations. The DG penetration is limited by the violation of upper voltage magni-

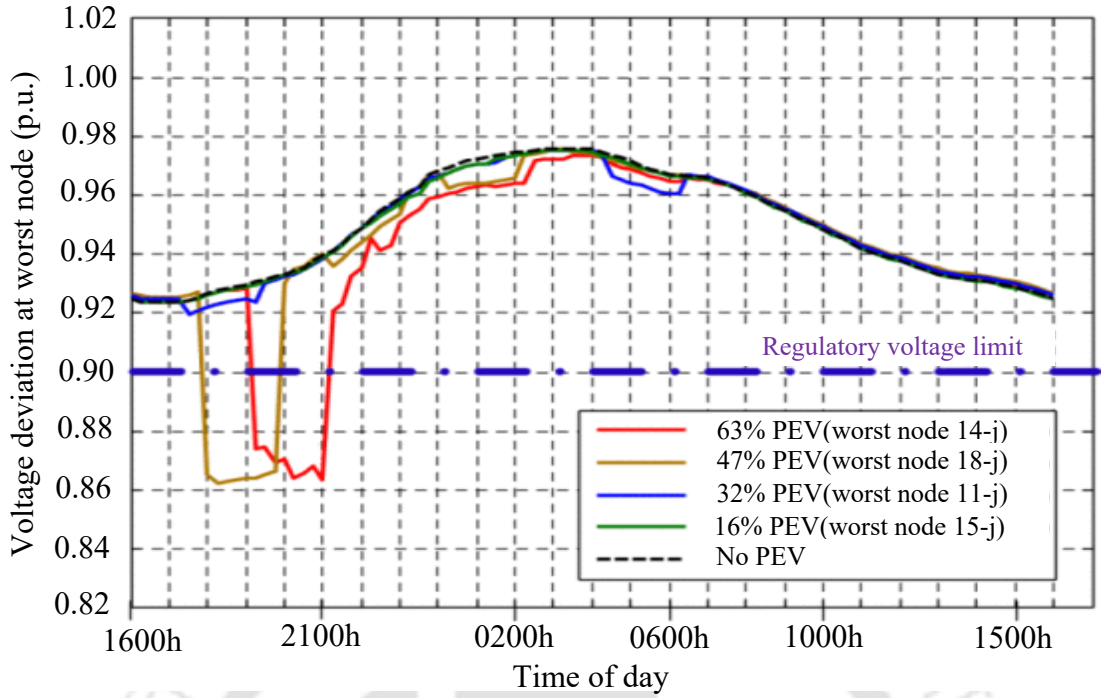

Fig. 1.2 Impact of uncoordinated EV charging on the voltage profile [28].

tude limits [29], [30]. On the other side, the load hosting capability is restricted by the violation of minimum voltage magnitude limits. The extra loading burden on the distribution grid due to the EV's integration has been reported in [7], [31], [32]. The base load on the system and extra loading due to EVs are shown in the Fig. 1.3 [33]. The curve considers the traditional EV charging loads, where the customer plugs the EV to the distribution system and once the battery is fully charged it will be disconnected. The peak demand is observed when the EV owner arrives at home in the evening, and plugs the EV for charging. This direct charging adds to the traditional peak loads, and an increased demand is observed during normal peak hours. Reinforcements in distribution network becomes an absolute necessity to safely handle these loads.

The active and reactive power control is very important to maintain the voltage and frequency within standards in a power distribution system. The CPT primarily transforms the voltage between different levels; however, its active and reactive power control capabilities are limited. In traditional distribution grids with more RES based DG sources, the reverse power flow scenarios are common. The on-load tap changers (OLTCs) offer a limited flexibility to control the reverse power flow [34]. Reverse power flow control requirements in a RES-rich distribution grid is investigated in [35]. Beyond active power flow, the presence of reactive and harmonic loads are also increasing in the distribution grid. The presence of harmonic loads on the system generates non-sinusoidal

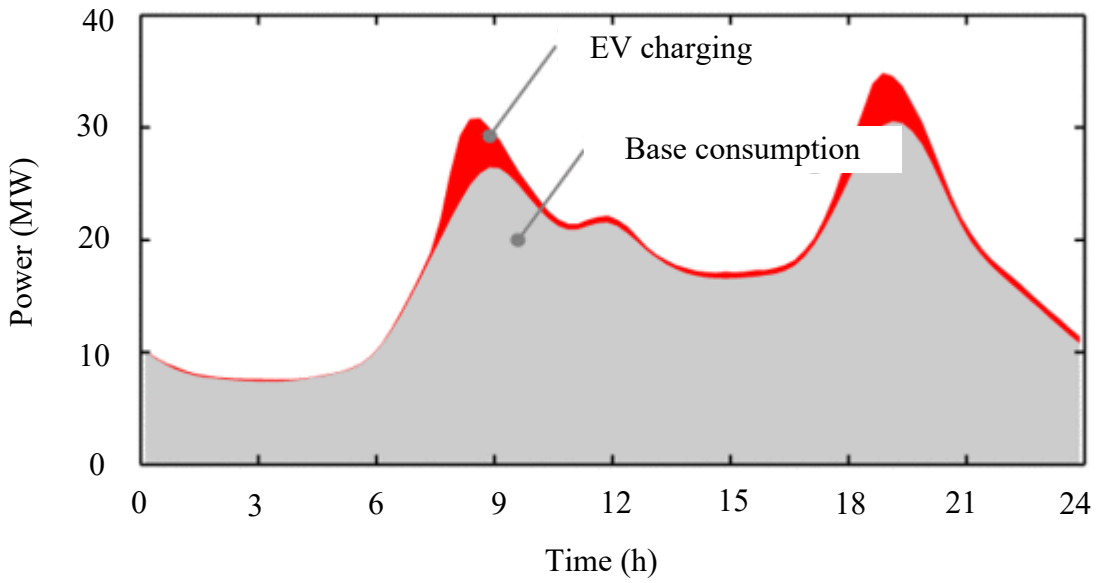

Fig. 1.3 The loading on the existing system with the uncoordinated EV charging [33].

current flow. The single-phase loads and the non-uniform loading on the phases lead to the introduction of unbalanced three-phase currents. In the absence of compensating devices, these harmonic and unbalanced currents will be absorbed from the main source. This increases the total harmonic distortion (THD) of source currents [36]. The harmonic and reactive current-flow in the distribution system introduces extra power losses in the system. Moreover, the voltage waveform quality in other parts of the system will also be affected due to the harmonic current flow. Another important aspect is regarding the integration of RES to the conventional AC system. The DG sources such as PV and BESS generate power in DC, and the integration with the conventional AC grids requires DC/AC converters [37]. The presence of both AC and DC sources, and loads require more control and integration facilities in the grid for a smooth and efficient operation. For the mitigation of these issues, multiple approaches are reported in the literature. These are discussed in the next section.

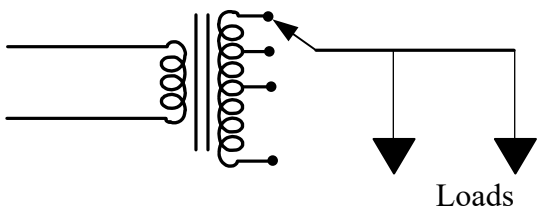

Fig. 1.4 Schematic representation of OLTC.

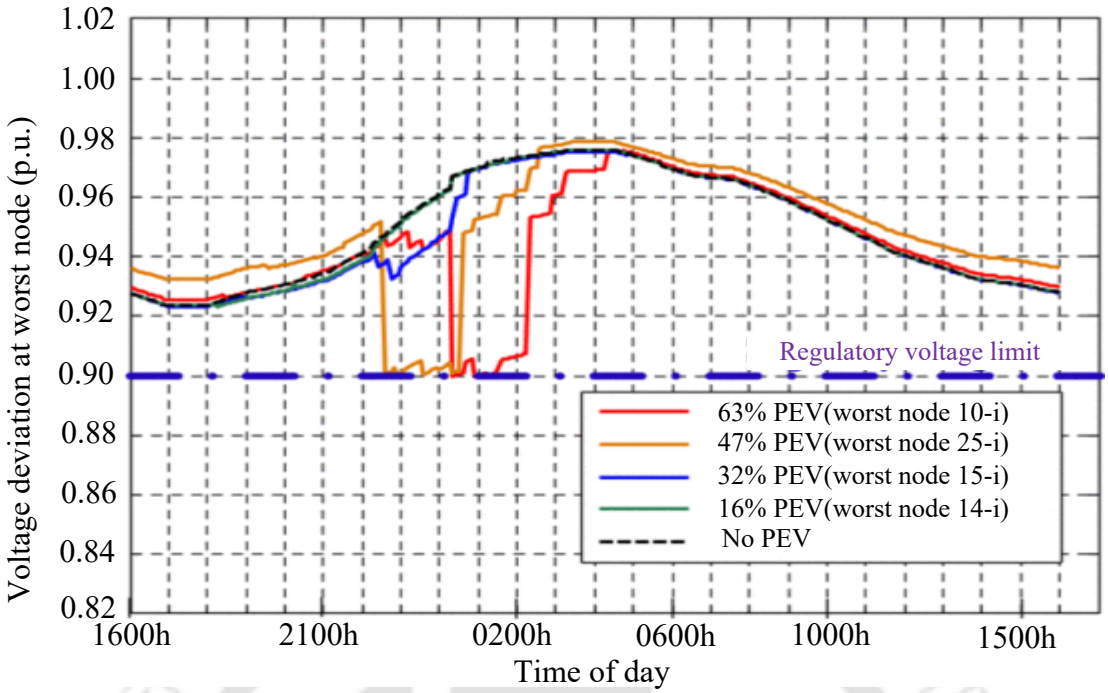

Fig. 1.5 Impact of coordinated EV charging on the voltage profile [28].

1.1.2 Solutions Proposed in the Literature

Different approaches are discussed in the literature for improving performance of electric distribution grid. The OLTC is considered to be one of the traditional voltage regulators. A schematic representation is shown in Fig. 1.4. Based on the available voltage tapping, it can be operated with variable voltage set points in a distribution system. In [38], the OLTC is combined with distributed energy storage system for voltage rise mitigation in a grid with high PV penetration. The coordinated control helps in reducing the operational stress on the OLTC. The static var compensator (SVC) can be used to compensate the reactive power in distribution system. This is suitable for both the voltage rise mitigation and load reactive power support applications. The reactive power compensation capability of SVC, and the voltage control capability of OLTC are combined to improve the hosting capability of distribution system [39]. Traditionally, the DG sources are controlled to supply the active power based on the availability of RESs. However, the voltage rise issues can be effectively mitigated using the coordinated operation of DG sources [40]. The approach does not directly control the voltage rise, instead exchanges a necessary reactive power based on the active power injections. This ensures that the DG active power injection is not causing voltage rise in the distribution system. Similarly, [41] proposes an active power-dependent strategy for voltage regulation in PV-based DG integrated grids. This method determines reactive

power based on the feed-in active power for each PV-based DG system, and an indirect control of the voltage is achieved. In the case of load, the coordinated EV charging reduces the peak loading on the distribution system [28]. The coordinated charging improves the voltage profile in worst-effected nodes as shown in Fig. 1.5. The customers are divided into low, medium and high priority, and the charging time zones are assigned based on the priority. This reduces the voltage deviation on the worst affected nodes. Often, the voltage sags are unbalanced in nature, and they are characterized by the presence of positive, negative and zero sequence components. The low-voltage ride-through (LVRT) capability is incorporated in DG converters, which maintains the grid-connectivity of DG converters during voltage sag conditions [24]. The algorithm presented in [24] ensures LVRT fulfillment, oscillating power control, and maximum grid current control.

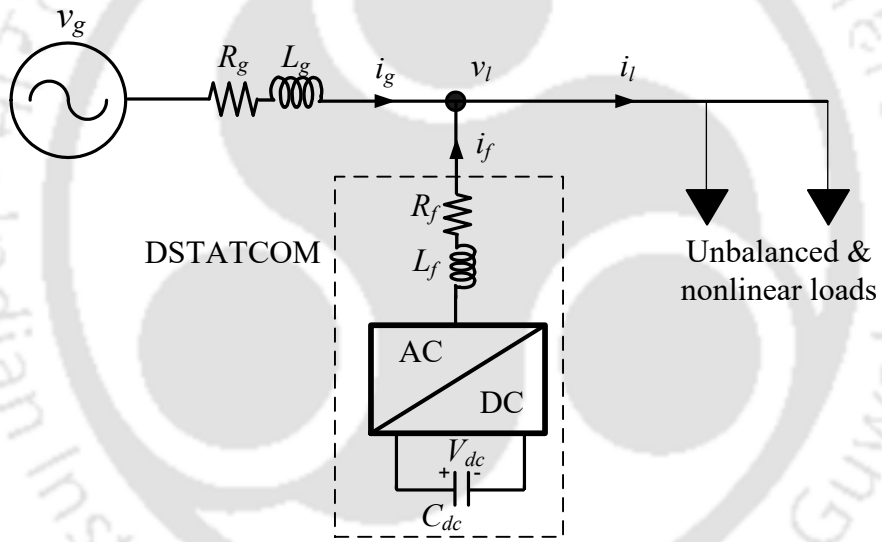

Fig. 1.6 Single-line diagram of DSTATCOM.

The introduction of a DC distribution system is considered to be an option to directly integrate PV-based DG sources, BESS and EVs [42]. The hybrid AC/DC grids are gaining attraction due to its capability to integrate sources and loads, both at AC and DC systems. This improves the power management capability in the overall distribution system. An interlinking converter is necessary for establishing such hybrid grids and a back-to-back (BTB) converter is used in [43], where PV source is integrated to the DC link. The DC bus serves to supply the DC loads, and exchanges active power with the AC grids. With the proposed control, an improved power management strategy with decentralized power distribution is achieved in AC/DC hybrid microgrid. In [44], an algorithm has been proposed to control different sources and loads in both AC and

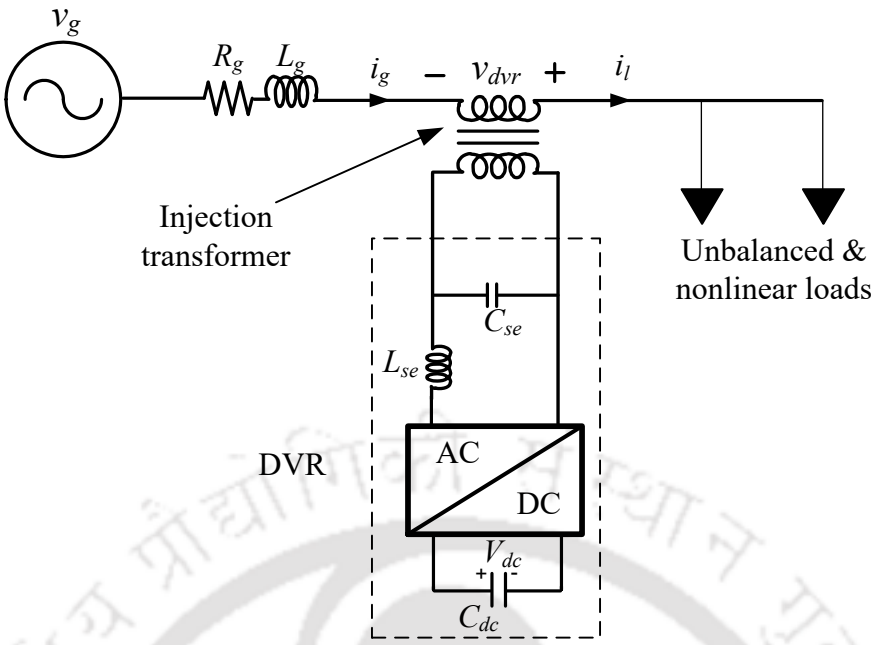

Fig. 1.7 Single-line diagram of DVR.

DC subgrids. The flexibility of proposed power flow control methodology helps in incorporating better control for DG and interlinking converters.

The custom power devices (CPDs) are power-electronic based devices employed in the power distribution system for maintaining power quality. These are utilized for various applications such as current harmonic compensation, load balancing, reactive power compensation, voltage regulation, etc. [45], [46]. Distribution static compensator (DSTATCOM), dynamic voltage restorer (DVR) and unified power quality conditioner (UPQC), etc. are CPDs employed for providing different features in the distribution system. A single-line diagram of the DSTATCOM is shown in Fig. 1.6. The DSTATCOM is a shunt connected CPD. It is capable of improving the power quality problems associated with the currents, such as harmonic filtering, power factor correction, load balancing, etc. [47]. Moreover, it can also support the load voltage by the appropriate injection of reactive currents. It injects the current using an AC/DC converter supported by a DC link voltage. A single-line diagram of DVR is shown in Fig. 1.7. The DVR is a series-connected device used to protect the critical loads from supply side voltage disturbances such as voltage sags/swells, harmonics, etc. [48]. It injects the required magnitude and phase angle of voltage in series with the distribution feeder using injection transformers and AC/DC converter supported by a DC link voltage. A single-line diagram of UPQC is shown in Fig. 1.8. The UPQC combines the series and shunt active

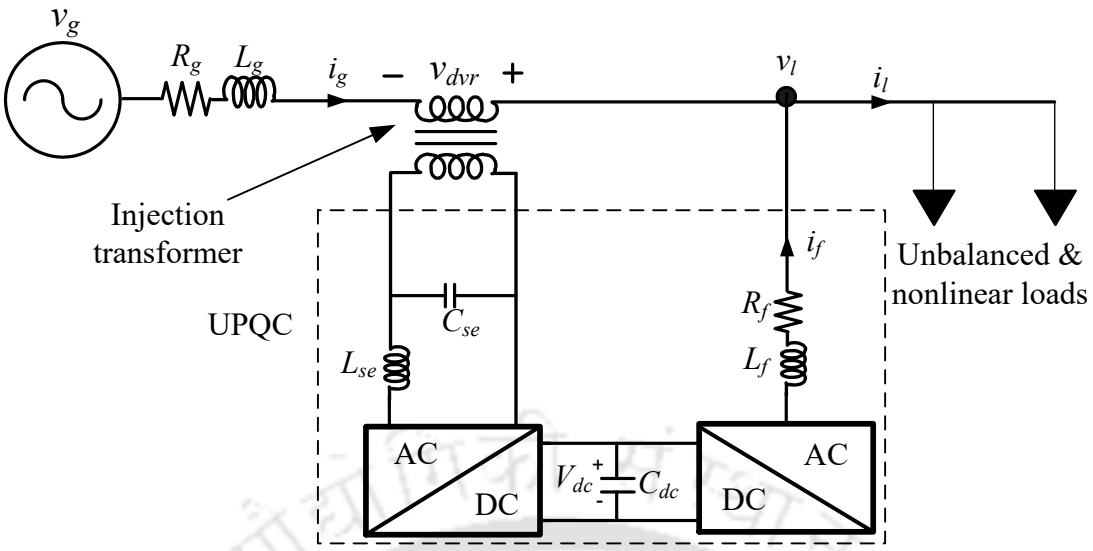

Fig. 1.8 Single-line diagram of UPQC.

power filters sharing a common DC link [49]. It is capable of simultaneously providing different services such as voltage sag/swell mitigation, harmonic current compensation, power factor correction, etc. in the distribution system.

The OLTC is a simple solution to the voltage rise/drop problems; however, the range of operation is very much limited. Integrating the reactive power control for DG converters increases the control complexity. More coordination will be required from different operators to maintain the voltages within grid-code limits. Active power curtailment methods reduce the overall energy extraction from RESs. Continuous research is being carried out on hybrid microgrids, and more structural transformations are needed to find the optimal configurations. The CPD operation largely depends on the R/X ratio of the grid, and the voltage support using reactive power is effective mainly in inductive grids.

The various challenges and the solution strategies are highlighted in the previous section. In addition, the limitations of these solutions are also discussed. From these studies, it is conclusive that multiple strategies or devices are needed to handle different challenges in the distribution grids. In this scenario, a power electronic based alternative to CPT has gained attraction, that can work as a central controller to control and coordinate different components in a distribution system. This kick-started significant focus on power electronic transformer (PET), also known as solid-state transformer (SST) [50].

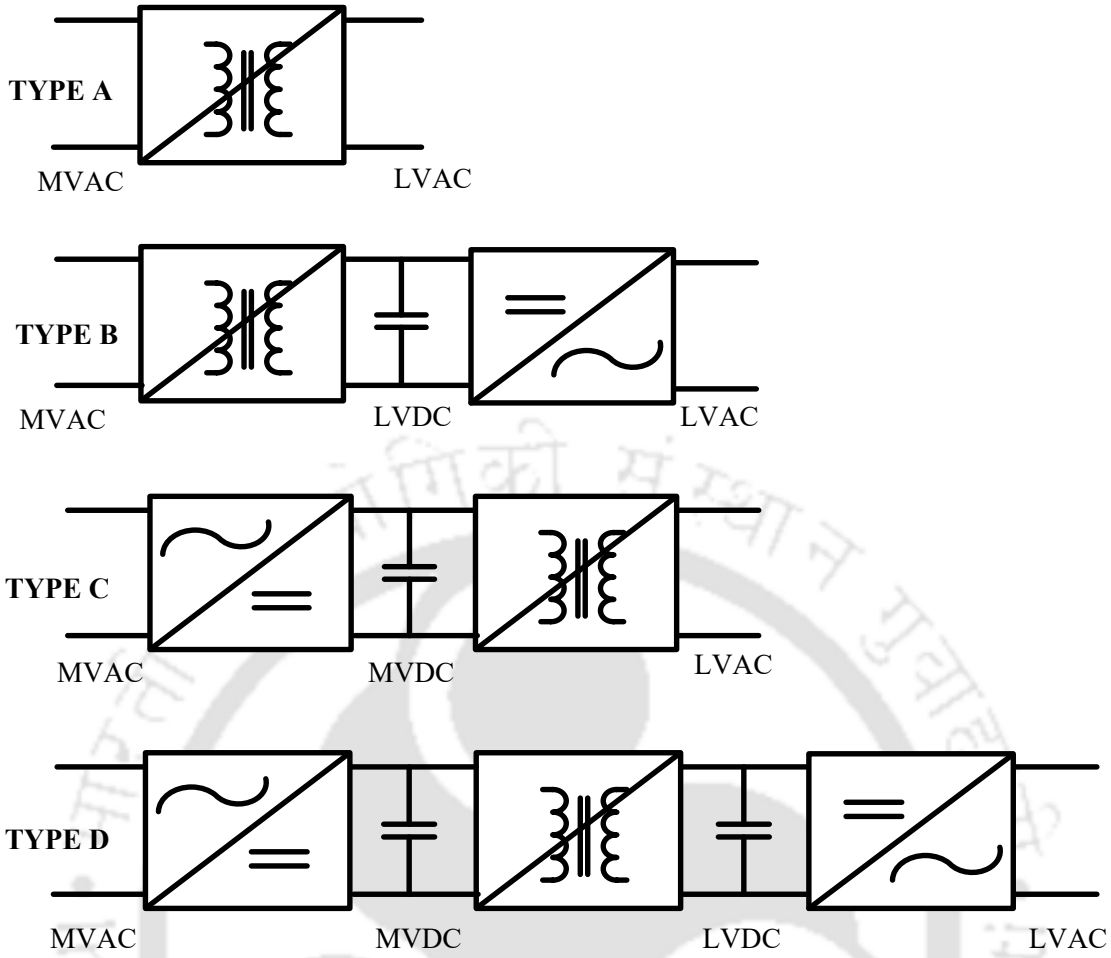

Fig. 1.9 Topologies of SST [51].

1.1.3 Solid-State Transformer

The concept of power electronics-based transformer has been proposed as a DC transformer in 1968 [52]. However, the major transformation in this concept happened after the development of power electronic switches such as insulated gate bipolar transistors (IGBTs). The first form of PET was an AC-AC single-stage conversion device [50]. Later, different topologies were proposed. Fig. 1.9 shows few of the major topologies of SST [51]. Type-A configuration operates as a direct AC to AC conversion with transformer isolation to step down from medium voltage (MV) AC to low voltage (LV) AC. This configuration presents a simple low-cost and lightweight solution. However, the absence of DC link makes this device not suitable for reactive power control operations. Type-B is a two-stage structure consisting of an isolated AC-DC conversion stage for providing the LVDC level followed by a DC-AC converter to supply the LVAC loads. This structure has a DC link that makes it suitable for reactive power compensation with suitable converter topologies. However, the unavailability of matured con-

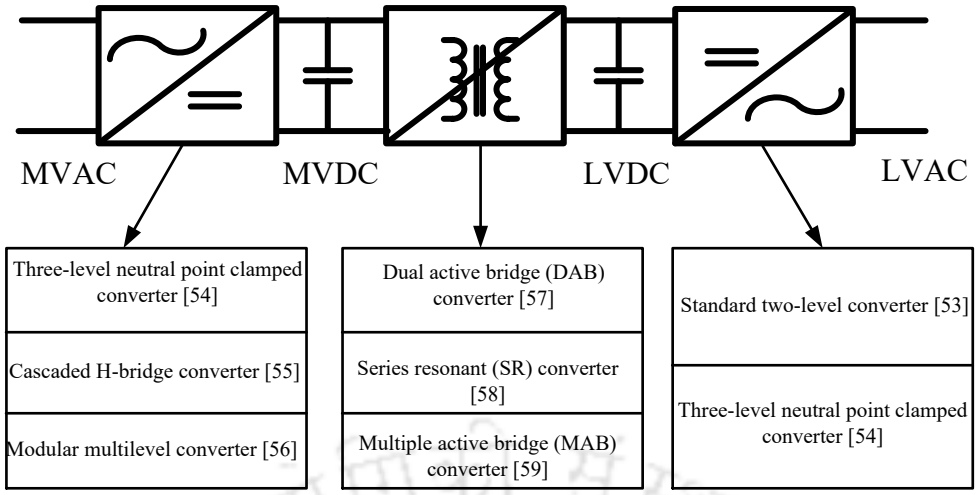

Fig. 1.10 The converter architectures identified for different stages of SST [53].

verter topologies to implement MVAC to LVDC conversion makes this structure less attractive. Type-C is also a two-stage structure; however, isolation is provided between MVDC and LVAC conversion. For this structure, the multilevel topologies are available for MVAC to MVDC conversion. This configuration also has the capability for reactive power control. However, the unavailability of DC link at the LVDC level makes this device unsuitable for renewable integration at DC link. Type-D is a three-stage conversion structure with high-frequency isolation between the MVDC and LVDC stages. There is an increased attraction towards three-stage type-D structure because of the possibility of optimization at each stage in terms of efficiency, volume, and weight. Moreover, the availability of DC links at MV and LV levels make this structure suitable for several applications such as RES and BESS integration, establishing DC distribution systems, etc. All these configurations are analyzed extensively, and various merits and demerits are detailed [51].

The three-stage SST is considered to be a flexible option to implement the modular architecture in each stage. Fig. 1.10 shows different converter architectures identified for three-stage SST [53]. For the MVAC converter, the three-level neutral point clamped (NPC) converter [54], cascaded H-bridge converter [55] and modular multilevel topologies [56] are feasible options. The multilevel topologies such as three-level NPC, is the immediate available solution for the MVAC converter because it is a well-used option in industry. The availability of DC link is another feature which makes it suitable for MVAC converter. Cascaded H-bridge converter is modular solution with low-control complexity. However, the absence of DC link at the MVDC level makes this struc-

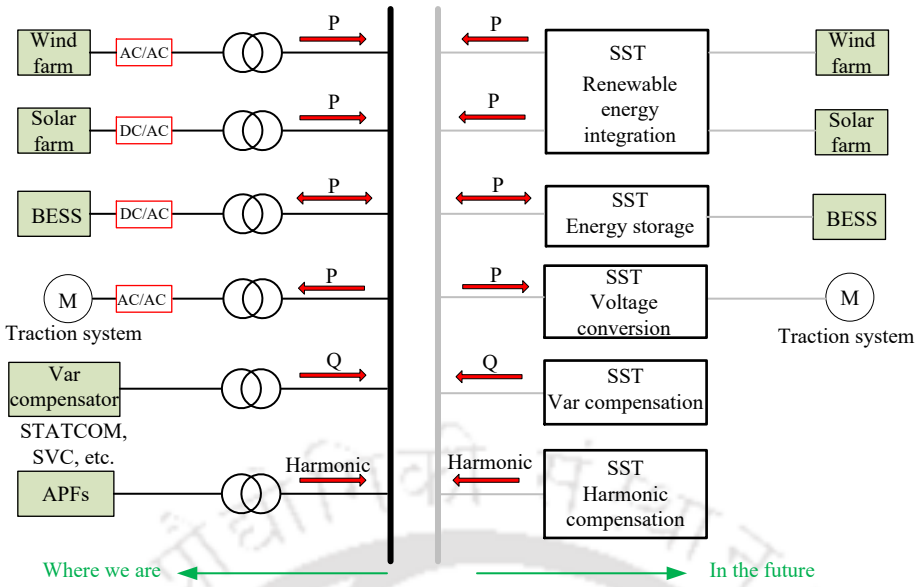

Fig. 1.11 Potential applications of SST [51].

ture less attractive. The modular multilevel topologies provide a modular option with the availability of DC link, however the suitability in MV range needs further study. Considering the availability of MVDC link and control simplicity, a three-level NPC converter is considered to be suitable option for distribution system application. For DC-DC converter, the dual active bridge (DAB) converter [57], series resonant (SR) converter [58], multiple active bridge (MAB) [59], etc. are discussed in the literature. The DAB and SR converters provide high efficiency and power density. The SR converter provides a well regulated DC voltage for a wide range of loads. The DAB is considered to be a better option if the output voltage or power flow control is required. The MAB is also a suitable option similar to DAB, and it uses a single isolation transformer for multiple active converters. The constant power flow control between MVDC and LVDC links is important for the distribution grid applications, and the DAB converter is considered to be a suitable option. For LV converter, standard two-level converter with neutral connected to the midpoint of DC link [53], and three-level NPC converter [54] are most suitable options. The two-level converter is a simplest option offering a neutral link, which is required for the three-phase four-wire LVAC distribution grid.

The laboratory-scale prototype of PET is proposed for traction applications in [60]. The weight and volume reduction was attractive in the traction applications; however, the gain margin due to this was not enough to replace the CPT in traction industry. A complete SST to CPT comparison is provided in terms of volume, weight and cost in [61]. At the present stage, the complete AC-AC conversion of SST is costlier than

the CPT and includes higher losses. However, the AC-DC conversion applications offer a better solution than CPT in terms of overall power loss, weight and volume. The use of SST for the MV/LV substation applications has been receiving more interest in the recent years, and various research projects such as 'HEART' [53], 'FREEDM' [62], etc. are under progress to explore this feature. The academic research in the field of SST has been carried out in different directions, and SST is proposed as an energy router in renewable-rich power systems [62]. In [63], an SST prototype is demonstrated for the applications in the power distribution system. The potential application of SST in the distribution system has been identified in [51], and it is shown in Fig. 1.11. The basic operation being the voltage transformation, it has the capability to replace different conventional solutions and CPDs in multiple applications. The integration of RES, BESS, harmonic and reactive power compensation, etc. are few of the identified applications. The realization of potential features in real-time applications require the incorporation of control and communication features to the basic SST structure, and this transforms SST into a smart transformer (ST) [53].

1.2 SMART TRANSFORMER

Replacing CPTs in a distribution system is a great challenge because CPT is a highly efficient and cost-effective solution to voltage transformation. Simple replacement of a CPT with ST can only be justified with the ancillary services provided by ST, along with voltage transformation [53], [64]–[67]. Fig. 1.12 shows the features of ST in distribution grid applications [64]. In the MVAC grid, ST has the capability for voltage support, power quality improvement, etc. In the MVDC link, it can integrate BESS, EV fast-charging station, PV, etc. Similarly in the LVDC link, the renewable and BESS integrations are possible. In the LVAC grid, ST is used for controlling the voltage, load, and power quality [64].

The three-stage ST configuration consists of an ST MV converter, ST DC-DC converter and ST LV converter as shown in Fig. 1.13. Each of the stages is controlled by a separate PWM controller. The ST MV converter controls the active power flow and MVDC link voltage. The ST DC-DC converter maintains a constant LVDC link voltage. The ST LV converter maintains a three-phase balanced sinusoidal voltage at the LVAC terminal irrespective of the load. The ST MV converter maintains a unity power factor current

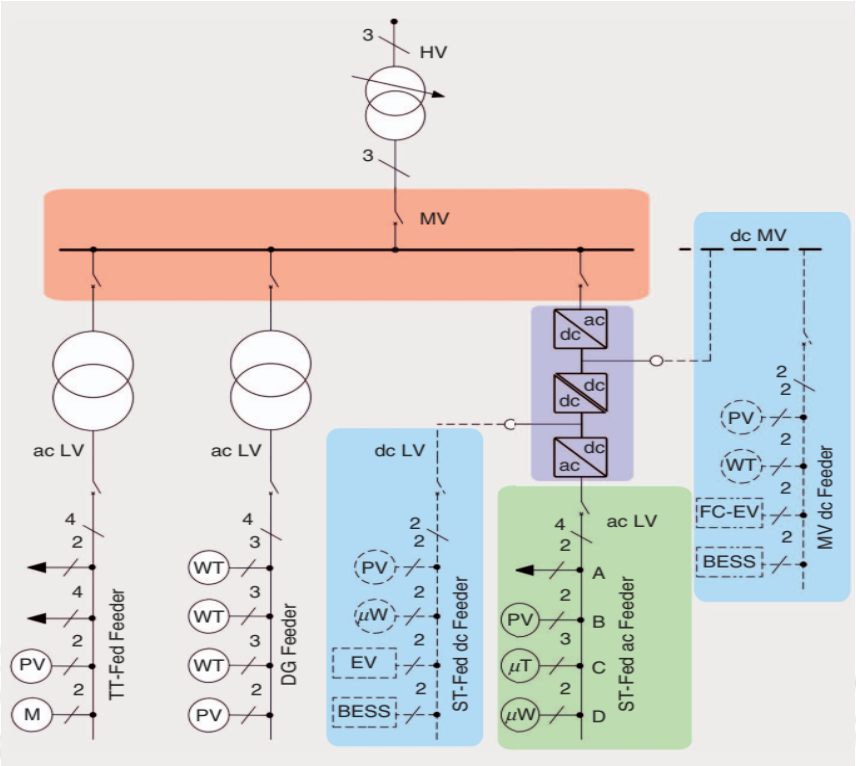

Fig. 1.12 The features of ST in distribution system [64].

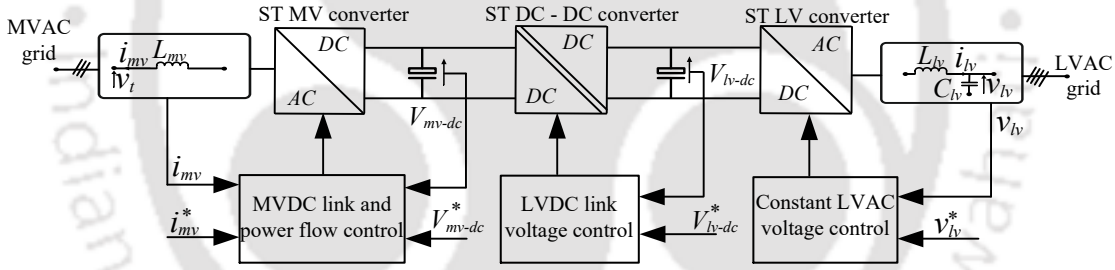

Fig. 1.13 A three-stage smart transformer with basic control block [53].

absorption from the MVAC grid, and the active power required at the LVAC side of ST is absorbed from the MVAC grid by the ST MV converter. In Fig. 1.14(a) and (b), two operational scenarios are shown. The LVAC grid voltages are unaffected by the MVAC grid voltage sags. Fig. 1.14(a) shows the ST MV converter currents, which increases due to the voltage sag to provide the active power requirement at the LVAC side. The LVAC voltages remain unaffected as seen in Fig. 1.14(a). In the second case, the operation of ST with nonlinear LVAC loads is considered as shown in Fig. 1.14(b). The nonlinear part of the LVAC loads are not reflected back to the MVAC grid currents and it is supplied from the ST LV converter. The MVAC current remain sinusoidal as seen in Fig. 1.14(b) irrespective of the nonlinear current at the LVAC grid seen in the Fig. 1.14(b).

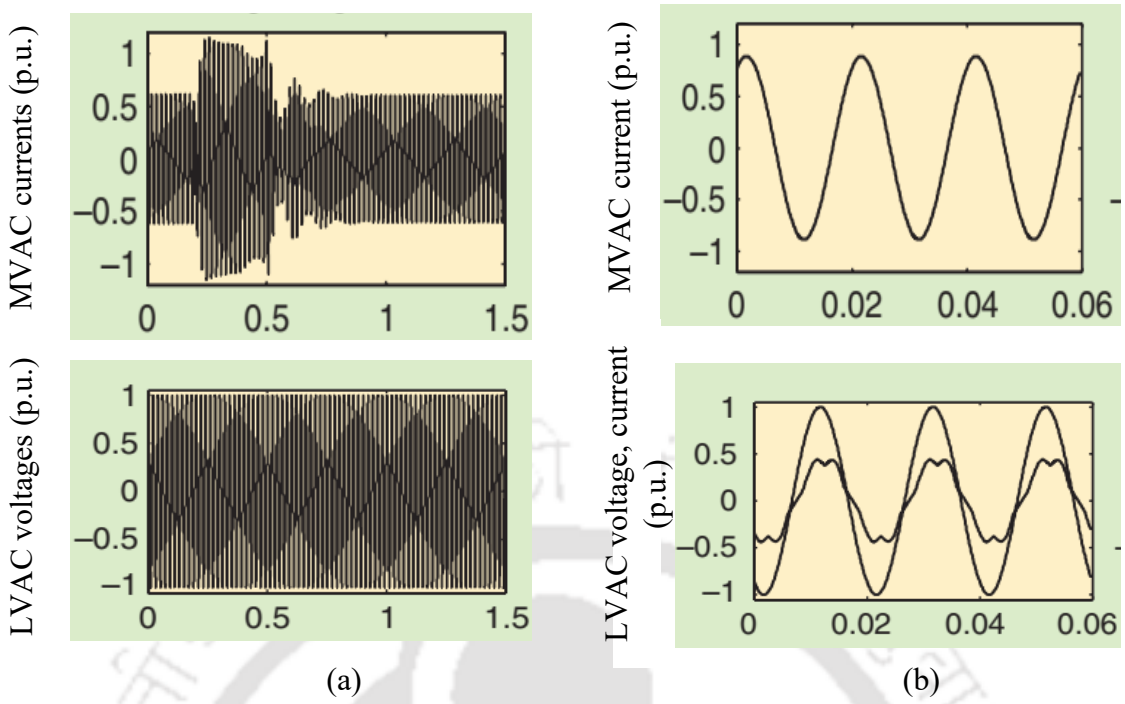

Fig. 1.14 The ST operation (a) during MVAC grid voltage sag. (b) with nonlinear LVAC load [53].

The ST MV converter is controlled as a current controlled voltage source converter. The load requirement at the LV side and converter losses are provided from the MVAC grid. Various control methods are discussed in literature for current controlled voltage source converters. All these controllers operate to minimize the error between reference and measured currents by generating appropriate PWM switching states. The current control methods can be classified as linear and nonlinear type controllers [69]. In the linear controlling schemes, the error compensation and modulation parts are separated, and this allows user to choose a constant switching frequency as per requirement. The PI based synchronous controllers are one of the linear controller. The three-phase currents are converted to their rotating synchronous d and q components. Two separate PI controllers are used for d and q to reduce the errors in respective components. The PI outputs are transformed back to three-phase voltage commands to use in PWM modulator [70]. Similarly, the currents are used in stationary coordinates, and controlled using the current controllers [69]. Other possibility for ST MV converter is the use of harmonic current controllers. The harmonic current controller helps the ST MV converter to reduce the harmonics in the current during distorted voltage conditions [70]. In the nonlinear control schemes, the hysteresis current controller [71], [72] directly provides the switching states when the error between actual and reference currents ex-

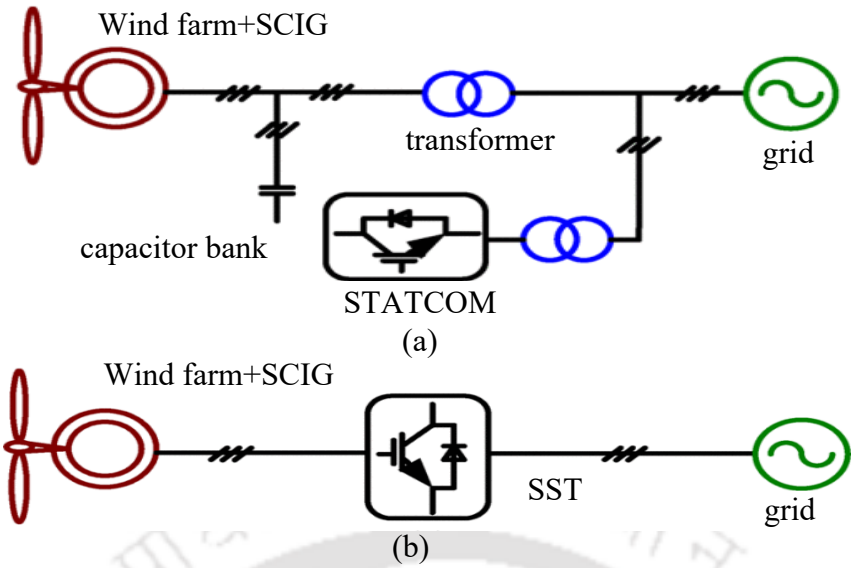

Fig. 1.15 Wind farm integration using (a) CPT. (b) SST [68].

ceed a tolerance band. The hysteresis controllers provide advantages such as simplicity in implementation, good dynamic response and low tracking error, etc. Various ST applications explored in the literature are provided as follows.

The interconnection of RESs at the ST LVAC bus is realized in multiple scenarios [68], [73], [74]. In [68], SST based wind energy conversion system has been proposed, and the SST smooths the voltage fluctuations caused by the wind transients. Fig. 1.15(a) shows the conventional wind farm system with CPT and STATCOM for reactive power compensation. The SST integration eliminates the STATCOM and CPTs as shown in Fig. 1.15(b), and an improved operation is reported [68]. In [73], a similar configuration is used for wind farm integration. The operation of the SST based configuration is verified during symmetrical and unsymmetrical fault conditions. A configuration is used in [74] for the integration of large renewable sources with a CPT-ST combined system. In this configuration, the ST MV and LV converter capabilities are utilized for harmonic and reactive power compensation.

In the LVAC grid, the ST has been utilized to reduce the load consumption by soft load reduction method [75]. This method is also used to reduce the overload on ST by the voltage control. The proposed method is applicable as an alternate to the load-shedding measures, and it effectively reduces the load depending upon the grid operator request. Fig. 1.16(a) show the ST LVAC voltages and a distant bus voltage for load control operation. The voltage is reduced, and a corresponding load reduction is shown in Fig. 1.16(b). Distribution system with high penetration of RESs lacks system inertia due to

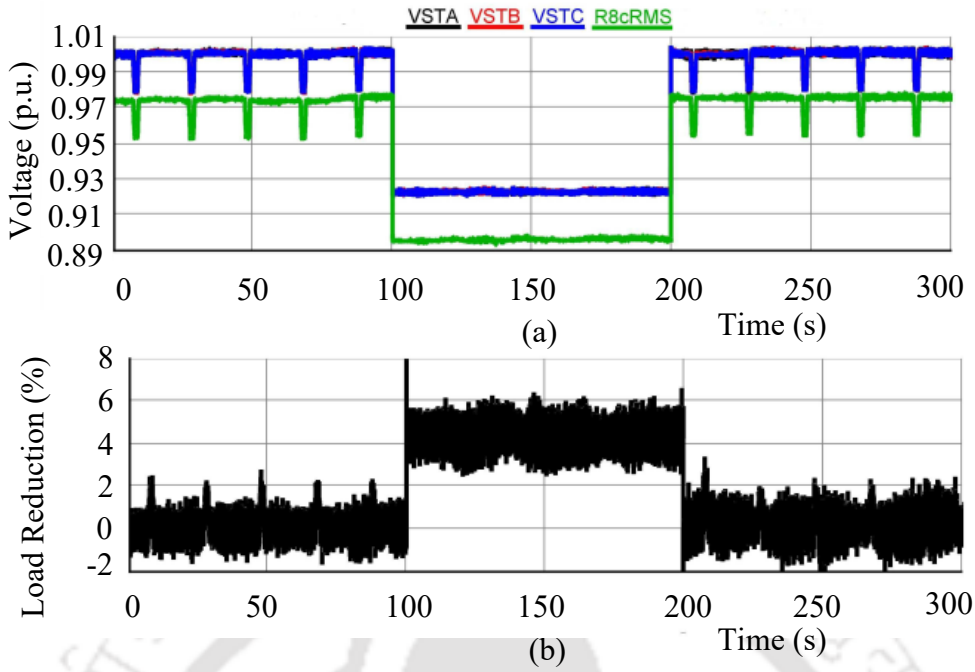

Fig. 1.16 The load control operation of ST. (a) ST LV voltage and voltage at a distant bus (green). (b) Load reduction [75].

the presence of more number of power electronic converters in place of conventional generators with rotational dynamics. Due to this characteristic, the frequency deviations are much more severe in these grids. The fast load control is a promising solution for providing inertia support, and [76] proposes a method using ST to support frequency regulation by voltage sensitivity based load power control. Single-phase to ground faults are common in the LVAC grids, and ST is capable of controlling the fault currents. The ST is capable of providing continuous operation during single-phase to ground faults with healthy phases. During this operation, the LVDC capacitor experiences larger oscillations which affect the ageing of the capacitor. In [77], a method is proposed to reduce these oscillations. Moreover, the neutral current during these faults is limited using the proposed method.

The stability of LVAC grids is important with the integration of multiple power electronic converters. The ST fed LVAC grid with multiple renewable integrations requires enhanced methods to stabilize the operation [78], [80], [81]. Fig. 1.17 shows the ST LVAC voltage and distributed energy resource (DER) current in an LVAC distribution grid. Without effective damping methods, the voltage and current remain distorted, and a lead element filter (LEF) based active damping improves the voltage and current waveforms [78]. The proposed method improves the overall stability of ST based LVAC distribution grids. The LVAC grid to MVAC grid reverse power flow is important in case

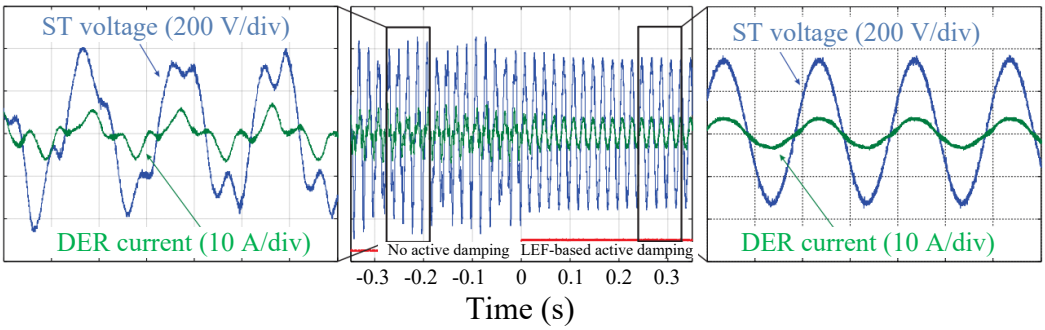

Fig. 1.17 The ST LVAC voltage and DER current with and without stabilization method [78].

of distribution grids with more number of RESs, and [79] proposes a method to control the reverse power flow using ST. The reverse power flow control reduces the voltage rise in the distribution grid. Here, the LVDC link voltage is considered as a parameter to detect reverse power flow. Based on the increase in DC link voltage magnitude, the ST LV converter regulates the LVAC frequency. The DG sources adjust the active power injection to the grid depending on the frequency. Moreover, this study explores the stability of the proposed controller. Fig. 1.18(a) shows the PLL frequency of PV-based DG connected to the distribution system. Following a DC voltage increase shown in Fig. 1.18(b), the ST controller increases the LVAC grid frequency. Depending upon the frequency characteristics, the power injection is reduced by the DG converters, as shown in Fig. 1.18(c).

The DC link of ST is used in different applications, and the operation of SST based DC microgrid is discussed in [85]–[88]. In [85], SST based DC microgrid architecture is proposed. This study focuses on the power management aspects of SST interconnected AC and DC microgrids. A zonal DC microgrid is considered in this study with loads, storage, and RESs. The interconnection to the AC microgrid is realized through SST and this improves the reliability of the DC microgrid. Different operating modes namely, passive grid interaction mode, active grid interaction mode, and islanding mode, are considered for the detailed analysis. In [86] a novel power management strategy is proposed for DC microgrid with SST integration. This proposes a communication-less intelligent control algorithm considering the state of charge (SOC) of BESS, SST AC loads, and PV based RES. In [88], for an SST based hybrid microgrid, a hierarchical power management scheme is proposed. This control scheme consists of different control layers based on different time scales and helps in operation

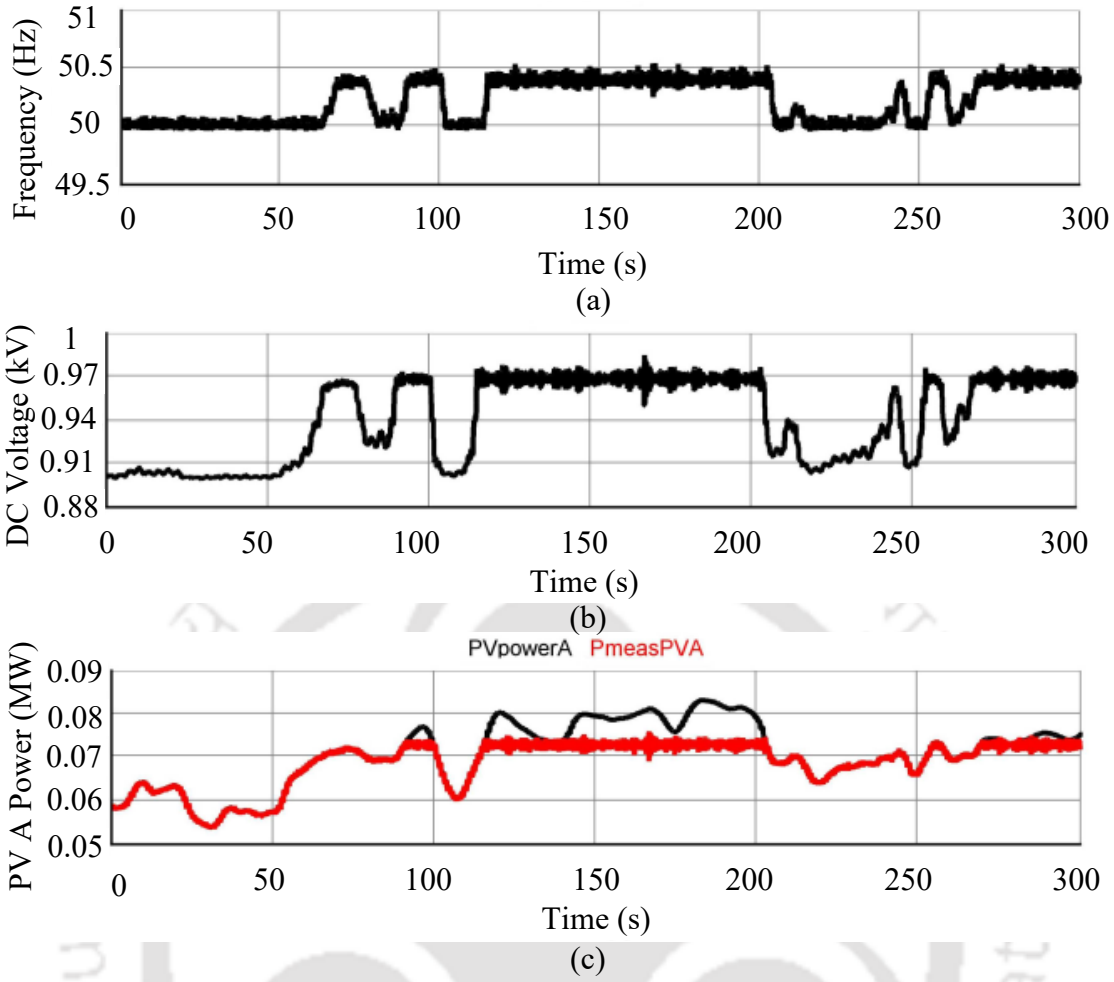

Fig. 1.18 Reverse power flow control operation of ST. (a) Frequency of PV PLL. (b) ST DC link voltage. (c) Theoretical and measured PV power [79].

during islanded and grid-connected modes of operation. The LVDC link is also used for BESS integration, and the BESS is used for AC grid support functions [82], [89]. In [89], two control objectives are analyzed. First, based on the load forecasts, a BESS dispatch plan is determined with the information about the residual charge. In the second control objective, voltages at MVAC and LVAC grids are controlled. For the MVAC grid, a reactive power control method is used to control the voltage within limits. For the LVAC grid, proper voltage set points are used such that the voltage is controlled along the feeder. A BESS charging and discharging method is proposed in [82]. The proposed method improves the efficiency of charging and discharging of BESS compared to the conventional methods. It also shows that, by the proper sizing of BESS for peak load shaving operation, the power rating of ST converters can be reduced. During MVAC grid voltage sag, the BESS supports the ST LVAC loads, and ST MV converter remains connected with the MVAC grid. The experimental results are shown in Fig. 1.19. Fig. 1.19(a) shows the MVAC voltage, whereas Fig. 1.19(b) shows different pow-

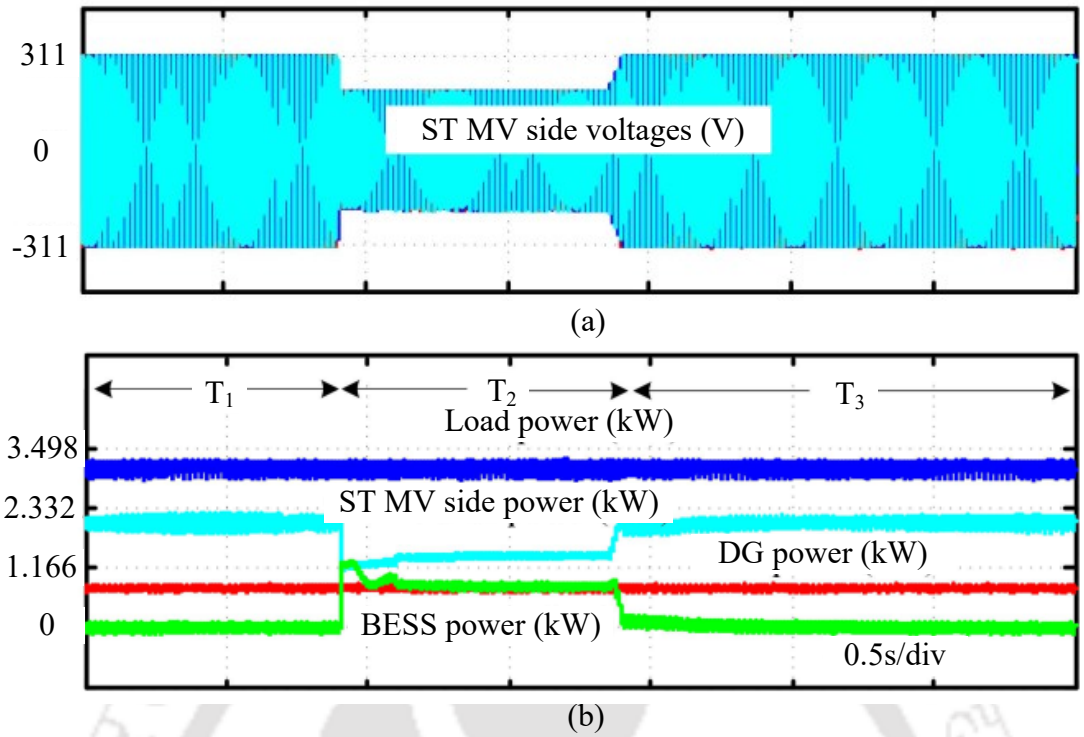

Fig. 1.19 BESS integrated ST during voltage sag. (a) MVAC grid voltage. (b) Different powers [82].

ers. The MVAC grid experiences a voltage sag as seen in Fig. 1.19(a). During sag, the ST MV converter absorbs the active power from MVAC grid as per the maximum rating to support its LVAC loads. The remaining LVAC load power is supplied by the BESS as seen in Fig. 1.19(b). The load power remain constant during the operating period.

The MVAC grid support functions are investigated for different applications [83], [84], [90]–[92]. In [83], the authors tested the voltage control operation of SST in an IEEE 34-bus system. The proposed dynamic voltage-var control algorithm helps in regulating the voltage by the exchange of reactive power. In addition, the proposed algorithm does not require any communication for its execution. The phase-*c* voltage of bus with and without control is shown in Fig. 1.20. With the volt-var control, the voltage profiles are maintained within the boundaries. In [84], reactive power support is used for loss reduction. The SST installation at different scenarios are considered, and an increased deployment of SST in distribution system can result in reduction of distribution system losses. In Fig. 1.21, the losses are plotted with the increase in the installed SST capacity. The graph shows the reduction in losses with the increase in SST penetration. A dual microgrid operation of ST is proposed in [90]. During normal operation, the ST supports the LVAC loads and exchanges the active and reactive powers with MVAC

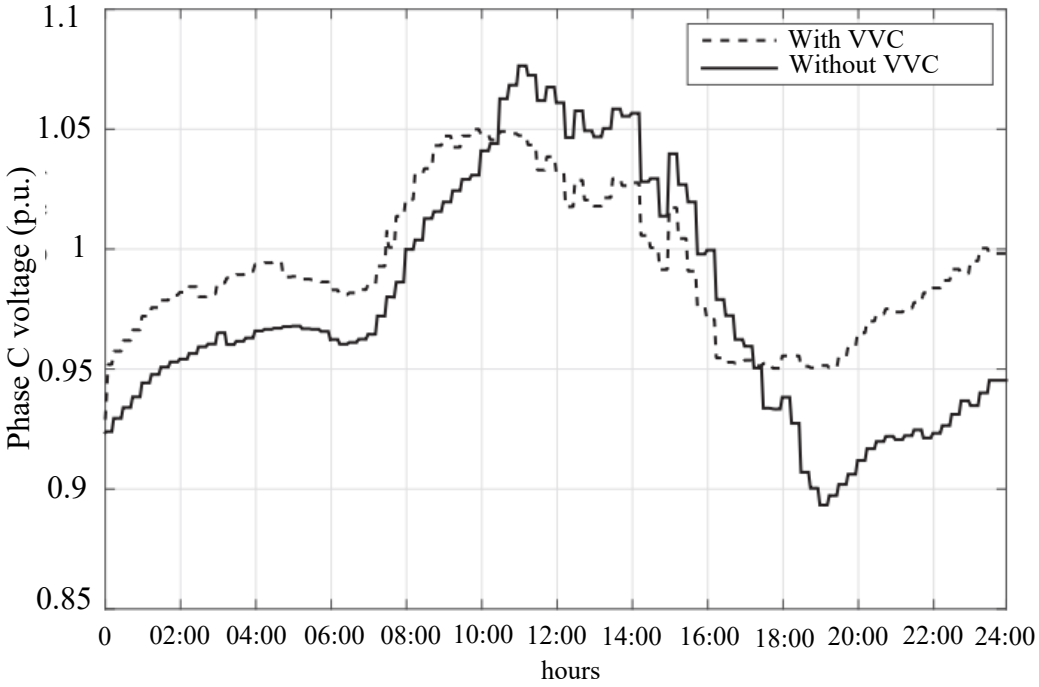

Fig. 1.20 Bus voltage of phase-*c* [83].

grid depending upon the availability of RESs. In the event of MVAC voltage disturbances, the ST supports the MVAC grid sensitive loads. The MVAC grid harmonic compensation features of ST are explored in a two-feeder system [91]. For the ST connected feeder, the ST LV converter supplies the harmonic and reactive loads. The ST MV converter supplies the active power requirement at the LVAC grid and compensates for the second MVAC feeder harmonic and reactive power loads. The source current supplies only active part of the load. In double circuit lines, during a fault on one line or transformer, the healthy line is used to supply the entire load. In this scenario, the healthy line and transformer may get overloaded. In [92], the ST supports the critical loads of the faulty feeder during fault condition. This operation improves the reliability of power supply to the loads and reduces load-shedding requirements.

1.3 MOTIVATIONS

The renewable-rich modern distribution grid is experiencing multiple challenges such as voltage magnitude variations, limited active and reactive power control capability, harmonic currents, etc. For addressing these challenges, various solutions are proposed such as active/reactive power control of DG, integration of CPDs, AC/DC hybrid micro-

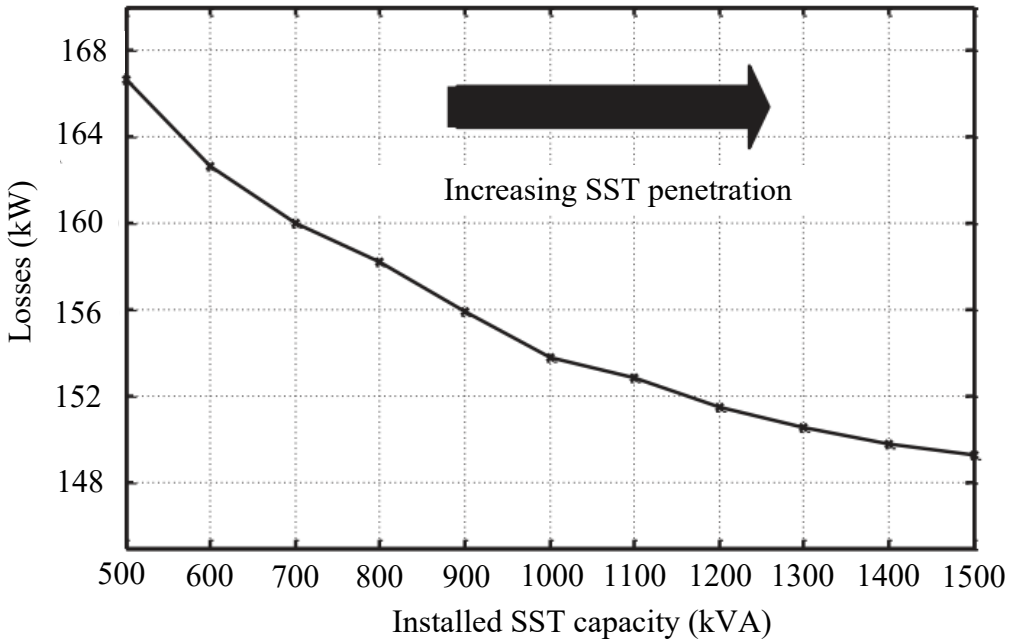

Fig. 1.21 Losses in IEEE 33-bus distribution system [84].

grids, etc. These solutions are used in different applications based on the requirement. However, a central controller can be used to coordinate and solve multiple issues in the distribution grid. This need lead to the emergence of ST. In addition to the features of CPT, the ST has potential to perform multiple grid support functions in LVAC, MVAC, and DC distribution grids. The ST features are explored in the LVAC grid during multiple scenarios. However, the MVAC grid support functions are little explored, and it requires more attention.

The reactive power support during voltage disturbance is important to maintain the stable operation of the distribution system. The ST MV converter is capable of providing necessary reactive power for the support of voltage in the MVAC grid [83]. However, the maximum amount of reactive power exchange depends on the rating of the converter. Coordinating the operation of ST LV converter and BESS capabilities during MVAC grid voltage disturbances improve the performance of ST MV converter. This aspect is not explored in the literature.

The hosting capability of a distribution grid is defined as the amount of load or generation that can be accommodated to a distribution system without the violation of network parameters such as voltage limits, thermal limits etc. The load and generation hosting capabilities are important in the modern distribution grid for accommodating more loads and RESs. The voltage magnitude variations often limit the hosting capacity of a dis-

tribution system. Active and reactive power support strategies are proposed in different studies for enhancing the hosting capacity [93], [94]. The ST with BESS integration has the capability to control the active and reactive powers in the distribution system. This feature has the potential to improve the hosting capacity in a distribution system which is not explored in the literature. This investigation can eventually expand the operational flexibility of ST in a distribution grid.

The LVDC link potential is explored in different applications such as the integration of BESS [82], [89] and enabling LVDC microgrids [86]. However, the MVDC link features are not widely explored. The MVDC based distribution system has emerged as a modern-day solution for power management problems in the conventional AC microgrids [95]. Interconnection of the AC microgrids with MVDC system leads to the formation of hybrid microgrids. Therefore, the ST MVDC link availability is an option to establish hybrid microgrids. The operation of ST-enabled MVDC interconnected systems needs to be studied and the performance required to be compared with the conventional solutions. Moreover, the performance of this system with the integration of BESS needs to be studied during different adverse grid operating conditions.

1.4 OBJECTIVES

Based on the literature and motivations, the following are the objectives of this research work:

1. To develop a strategy to coordinate the operation of ST MV converter, ST LV converter, and BESS for improving the reactive power injection capability of ST MV converter during MVAC grid voltage sag and swell.

2. To investigate the potential of BESS integrated ST in improving the hosting capacity of MVAC distribution system.

3. To explore the features of an MVDC based meshed hybrid microgrid enabled using STs, and comparison with the existing architectures.

4. To study the operation of an MVDC based meshed hybrid microgrid configuration using a BESS integrated ST during adverse grid conditions.

5. Validation of all the operating algorithms with real-time simulation studies and experimental verifications.

1.5 ORGANIZATION OF THE THESIS

Chapter 1 begins with the description about the evolution of power distribution system. The challenges faced by the modern power distribution systems, and the solutions proposed in the literature are described. The concept of SST and its evolution is explained. This is followed by the introduction of ST and their applications in the distribution systems. The motivations and main objectives of the thesis are also provided in the chapter.

Chapter 2 explains the operation of ST for the voltage support during symmetrical grid voltage sag and swell. The system configuration considered for the study is provided. The proposed control methodology is explained for ST MV, DC-DC, and LV converters and BESS. The impact of the proposed coordinated voltage support in the distribution grid is explained. The sizing of different power converters is also given in this chapter. Finally, the simulation and experimental validations of the proposed method are provided.

Chapter 3 provides the operation of ST in a radial distribution grid for the enhancement of the hosting capacity of the system. The system configuration and sensitivity analysis based converter sizing are explained in detail. The control of different power converters is discussed. The proposed method is validated with simulation and experimental results.

In **Chapter 4**, an ST based meshed hybrid microgrid operation is introduced. The conventional and restructured system configurations are provided. Different modes of operation of the meshed hybrid microgrid is discussed, and the control of converters is explained. Different parameters for the proposed system is compared with the existing technologies, and the important advantages are listed. Finally, the simulation and experimental results are explained in detail.

The operation of meshed hybrid microgrid based on ST is further analyzed in **Chapter**

5 for the operation during peak generation, peak load and voltage sag conditions. Different modes of operation and control of power converters are explained in this chapter. Detailed simulation and experimental results are also provided.

Chapter 6 presents the important conclusions from the research work and the suggestions for the future scope.

The details of the experimental setup with photographs are given in the **Appendix**.

CHAPTER 2

INCREASING VOLTAGE SUPPORT USING SMART TRANSFORMER BASED ENERGY STORAGE SYSTEM AND LOAD CONTROL

In Chapter 1, the challenges associated with the modern distribution grid and various solutions are explained. It also gives an introduction to ST and its prominent functionalities. Out of the different challenges mentioned in Chapter 1, voltage disturbances are critical power quality concern in electric distribution grid.

Voltage sag is defined as the decrease in fundamental frequency voltage magnitude between 0.9 and 0.1 p.u. for a duration of half cycle to 1 min [96]. Voltage sags are typically caused by the system faults or sudden load changes . Similarly, swell is defined as the increase in fundamental frequency voltage magnitude between 1.1 and 1.8 p.u. for a duration of half cycle to 1 min. Voltage sag and swell affect the normal operation of loads as well as DG sources and reduce the overall reliability of the system. For improving the voltage at point of common coupling (PCC), different grid codes require control of active and reactive powers through power electronic solutions. Voltage disturbances affect the normal DG operation, and may even force disconnection of DG sources from electric grid. Various solutions are proposed in the literature to keep the PCC voltage within grid codes, such as OLTC [97], DSTATCOM [96], DVR [98], UPQC [49], etc. Instead of using the additional devices, various control schemes have been developed to improve grid voltage by the effective control of DG converter active and reactive powers [99]–[101]. The BESS is considered to be an effective solution for peak load shaving operation, and it also has the potential to improve the voltage in the electric grid. Moreover, the BESS and DG coordinated operation can improve voltage regulation performance [102]. The voltage support from DG reduces the active power exchange from the converters, and thereby decreases the overall energy harvest.

The various power electronic-based solutions mentioned above are effective in providing the voltage support. Similarly, the ST is also capable of exchanging the reactive

power with the MVAC grid in addition to the supply of active power to its LVAC loads. The ST reactive power support can be utilized for improving the voltage at the MVAC grid [83]. This chapter investigates an enhancement strategy for ST's performance in MVAC grid voltage support. The integration of BESS at ST LVDC link is realized in [82], [89]. In [82], the MVAC grid voltage sag operation is analyzed; however, no voltage improvement strategies are discussed. The BESS is used to support the LVAC active power during MVAC grid voltage sag. The voltage support operations are discussed in [89] at MVAC and LVAC grids without the help of BESS. The load control features of ST LV converter is analyzed in [75]; however, the MVAC grid voltage control operations are not investigated.

From the literature mentioned above, the following details are observed:

- The reactive power capability of a grid-connected converter is important for the voltage support
- Utilizing DG converters for voltage support reduces the overall energy export from these sources
- The LVAC load support features of ST integrated BESS are explored for different applications [82], [89]; however, the service is not explored for MVAC grid voltage support
- The ST is utilized for MVAC grid voltage support [83], however the reactive power injection capability improvement is not discussed
- The load control features of ST LV converter is an important application [75], and it has the potential to improve the performance of ST MV converter as well.

This chapter explores the idea of utilizing the load power control features of ST LV converter and BESS for improving the reactive power injection capability of ST MV converter. The improved reactive power injection capability increases the voltage support from ST in MVAC grid during voltage sag and swell conditions. Moreover, the proposed scheme uses reduced rated BESS for the same voltage support capability as compared to [82], [89]. The simulation and experimental results are provided to verify the proposed operation.

2.1 SYSTEM CONFIGURATION

Fig. 2.1(a) shows the single-line diagram of a conventional distribution system. Two CPTs (T1 and T2) are connected to a 11-kV MVAC grid. The BESS is connected to

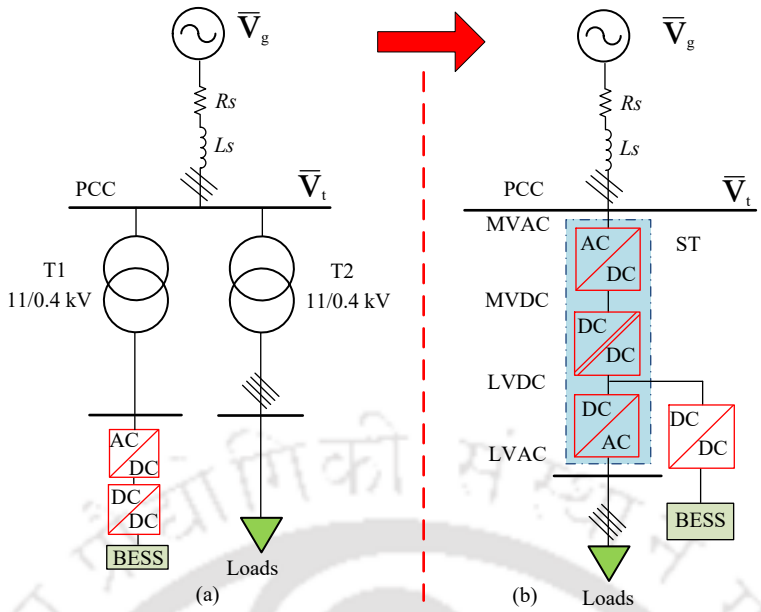

Fig. 2.1 Single-line diagram of considered system. (a) Conventional power distribution system. (b) ST based power distribution system [82].

the LVAC side of T1 through a DC-DC converter and DC-AC converter. Loads are connected to the LVAC side of T2. Fig. 2.1(b) shows an ST based configuration. The loads are connected to the ST LVAC terminal and BESS is integrated to the LVDC terminal through a DC-DC converter. This thesis uses a three-stage configuration of ST as shown in Fig. 2.2. The circuit consists of an ST MV converter, which is a three-level NPC AC-DC converter for connecting MVAC to MVDC as the first stage [54]. The second stage is a DAB converter, which connects MVDC link to the LVDC link [57]. The ST LV converter is a two-level, three-phase, DC-AC converter. It connects LVDC link to LVAC [53]. The MVAC grid is a three-phase, three-wire configuration. The isolation transformer used in DAB is used to step-down the MV level to LV level. The LVAC side is a three-phase, four-wire configuration, and the neutral conductor is necessary to connect the single-phase loads in LVAC grid.

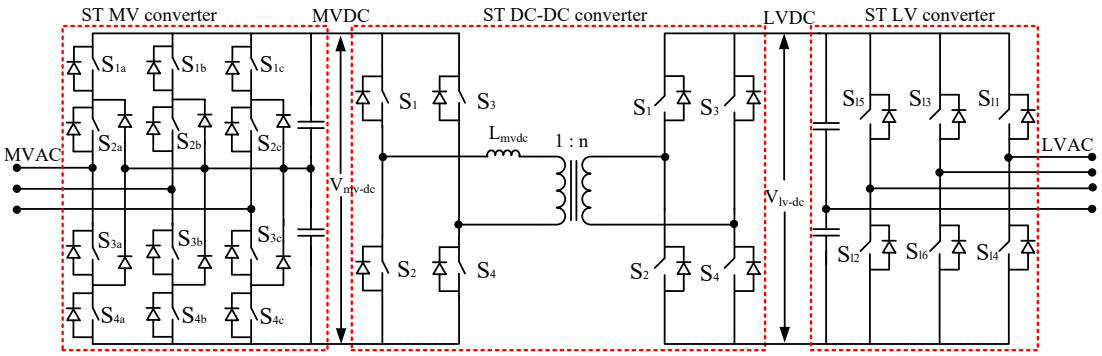

Fig. 2.2 Three-stage topology of ST.

2.2 CONTROL OF POWER CONVERTERS

In this section, control of the various power converters are explained in detail. Fig. 2.3 shows the overall control diagram of the system. i_{mva}, i_{mvb}, i_{mvc} are the three-phase ST MV converter currents. v_{ta}, v_{tb}, v_{tc} are the MVAC PCC three-phase voltages. L_{mv}, C_{mv} and R_{mv} are the filter inductance, capacitance and damping resistance of the ST MV converter. C_{mv-dc} and C_{lv-dc} are the DC link capacitance at MV and LV DC links, respectively. L_{lv}, C_{lv} are the filter inductance and capacitance of the ST LV converter, respectively. i_{lva}, i_{lvb}, i_{lvc} are the three-phase currents of ST LV converter and v_{lva}, v_{lvb}, v_{lvc} are the three-phase LVAC terminal voltages. For the ST MV converter, the reference currents (i^*_{mvabc}) are generated based on the mode of operation. These reference currents are used with a hysteresis current controller to generate necessary switching pulses for the ST MV converter. The ST DC-DC converter maintains a constant LVDC link voltage. The reference (V^*_{lv-dc}) and actual (V_{lv-dc}) voltage is used in the controller to generate the switching pulses for this converter. The ST LV converter reference voltage magnitude (V^*_{lv}) is generated based on the reference generation strategy. Based on this voltage reference, the necessary voltage is maintained by the converter. The BESS power reference (P^*_b) is generated from the control algorithm, and it is used to switch the BESS converter.

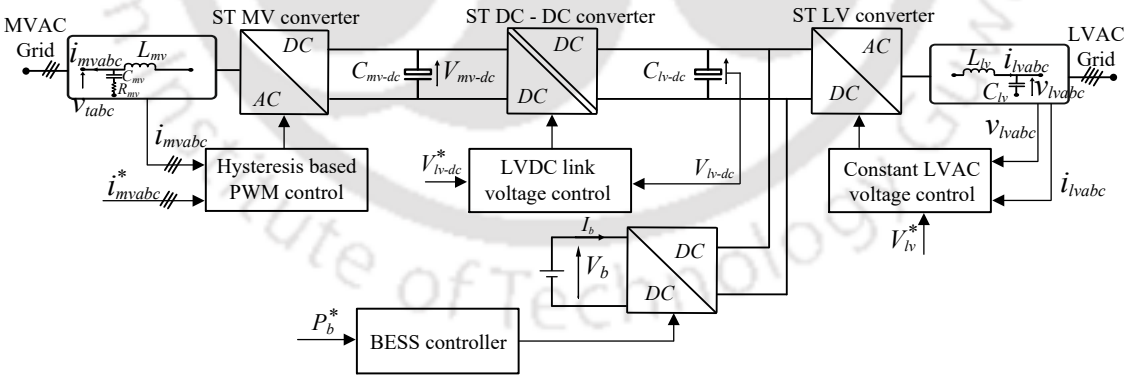

Fig. 2.3 Overall control diagram of ST and BESS.

The required voltage magnitude range for interconnection of solar PV based DG system is set between 0.88 and 1.1 p.u. [19]. On normal operating condition, when the voltage magnitude is between these limits, the ST MV converter draws only active power to supply its LVAC loads, and BESS. Moreover, no reactive power is exchanged with the MVAC grid. If the voltages violate the limits, reactive power is exchanged with the grid while maintaining the LVAC active power requirement. This operation is called as

voltage control operation. The flexible voltage support is achieved through coordinated operation of ST MV converter, LV converter and BESS. A flowchart representation of the proposed operation is shown in Fig. 2.4. Reactive power requirement at the MVAC grid is calculated to provide voltage support during voltage sag/swell. The ST continues supplying its LVAC loads. Based on the calculated active and reactive power requirement, the per phase reference currents for ST MV converter are calculated. If these currents are less than the rating of ST MV converter, the operation is continued by delivering the respective active and reactive power requirements. If the phase currents exceed the rating, the ST LVAC converter reduces the LVAC side voltage dynamically to 90% of the nominal value which is sufficient for load operation as per grid codes [103]. If the phase currents still exceed the limit, the BESS is activated to supply the active power requirement at the LVAC side. However, after coordinated control of ST MV converter, ST LV converter and BESS, if the ST MV converter currents still exceed the rating, a limiting value of reactive power is supplied to the MVAC grid. As per the Indian grid regulations, the connectivity standard is applicable to the wind generating stations, generating stations using inverters, wind-PV hybrid systems and energy storage systems [104]. The generating stations shall remain connected to the grid when the voltage at the interconnection point violates upper and lower limiting values. The station shall continue operation when the voltage at the connection point is less than or equal to 1.1 p.u. If the voltage is increased beyond this limiting value, the station may continue operation for a prescribed time depending upon the magnitude of voltage. Similarly, during voltage dips, if the voltage is greater than or equal to 0.85 p.u., the station shall remain connected with the grid. If the voltage falls below 0.85 p.u., the station shall inject the reactive current along with the active current with a magnitude depending upon the depth of voltage dip. It shall also remain connected with the grid for a prescribed amount of time . In this study, the lower and upper voltage limits used are 0.88 p.u. and 1.1 p.u., respectively. Therefore, the proposed method can be directly applied to the Indian conditions as per the requirement.

The reference generation strategy for ST MV converter, DC-DC converter, LV converter, and BESS converter are shown in Fig. 2.5, and detailed as follows.

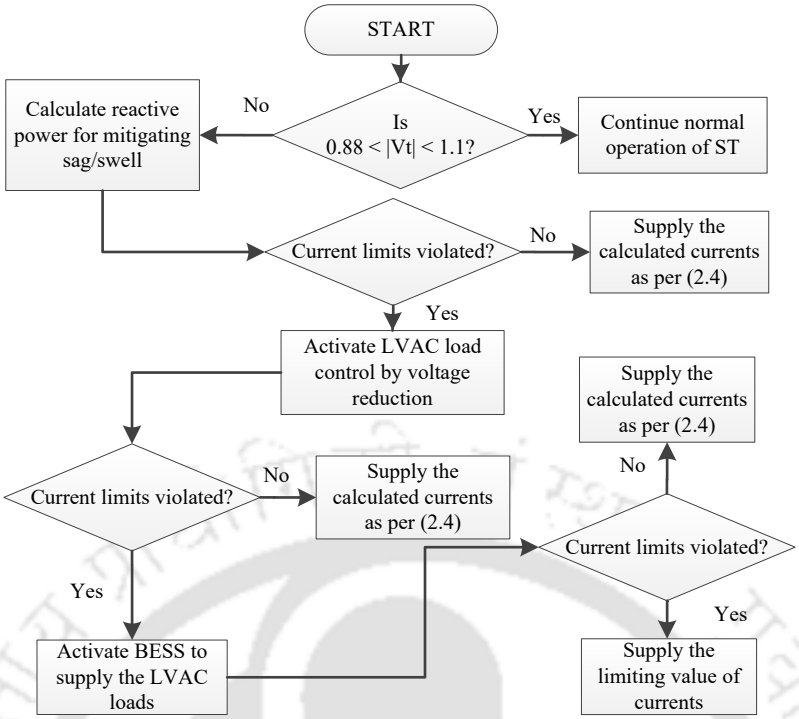

Fig. 2.4 Flowchart of the proposed control for coordinated operation of ST MV, LV converters and BESS.

2.2.1 ST MV Converter Control

The ST MV converter active power reference (P^*_{mv}) consists of the active power requirement for ST LVAC loads (P^*_{lv}), BESS charging/discharging power reference (P^*_b) and the active power loss component (P^*_{loss}) for maintaining the MVDC link voltage at a constant reference value. For the generation of P^*_{loss}, the reference MVDC voltage (V^*_{mv-dc}) is compared with the actual value (V_{mv-dc}) and passed through a PI controller as given by

$$P^*_{loss} = K_{p-l}(V^*_{mv-dc} - V_{mv-dc}) + K_{i-l}\int (V^*_{mv-dc} - V_{mv-dc})dt \tag{2.1}$$

where K_{p-l} and K_{i-l} are the proportional and integral gains of the PI controller.

For reference current generation, firstly the fundamental component of three-phase voltages (v_{ta1}, v_{tb1} and v_{tc1}) at PCC are expressed in stationary reference frame as $v_{t\alpha}$ and $v_{t\beta}$. The online estimation of fundamental components uses a moving average filter. This tracks the actual voltage since it uses a continuous averaging of a fixed number of samples with a moving window. At each sampling instant, the values of fundamental component is calculated with the data of last 'N' number of samples. For a moving

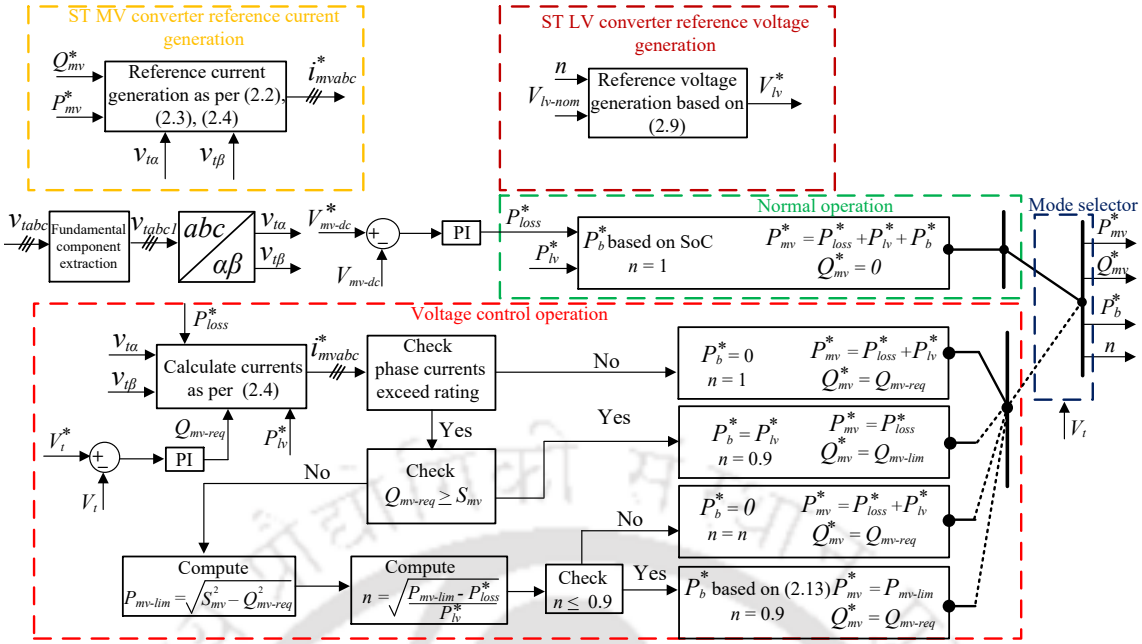

Fig. 2.5 The proposed reference generation strategy.

average filter with a window width of half the power cycle, the computation of fundamental component for any change in the actual voltage will be settled within 10 ms [71]. Therefore, it will not cause phase delay and will not affect the dynamic performance significantly. In order to facilitate the active power transfer, the current reference is calculated by [105]

$$\begin{aligned} i^*_{mv\alpha(p)} &= \frac{2}{3} P^*_{mv} \frac{v_{t\alpha}}{(v_{t\alpha})^2 + (v_{t\beta})^2} \\ i^*_{mv\beta(p)} &= \frac{2}{3} P^*_{mv} \frac{v_{t\beta}}{(v_{t\alpha})^2 + (v_{t\beta})^2} \end{aligned} \tag{2.2}$$

where $i^*_{mv\alpha(p)}$ and $i^*_{mv\beta(p)}$ are the reference currents generated in α and β axes, respectively for the active power transfer. For the reactive power transfer, the α ($i^*_{mv\alpha(q)}$) and β ($i^*_{mv\beta(q)}$) axes currents are generated as follows:

$$\begin{aligned} i^*_{mv\alpha(q)} &= \frac{2}{3} Q^*_{mv} \frac{v_{t\beta}}{(v_{t\alpha})^2 + (v_{t\beta})^2} \\ i^*_{mv\beta(q)} &= \frac{2}{3} Q^*_{mv} \frac{-v_{t\alpha}}{(v_{t\alpha})^2 + (v_{t\beta})^2} \end{aligned} \tag{2.3}$$

where Q^*_{mv} remains zero during normal operating condition. The total reference currents ($i^*_{mv\alpha}$ and $i^*_{mv\beta}$) in α and β axes are computed by adding (2.2) and (2.3). These are given

as follows

$$\begin{aligned} i^*_{mv\alpha} &= i^*_{mv\alpha(p)} + i^*_{mv\alpha(q)} \\ i^*_{mv\beta} &= i^*_{mv\beta(p)} + i^*_{mv\beta(q)}. \end{aligned} \tag{2.4}$$

The reference currents given by (2.4) ensure that the required active and reactive powers are exchanged with the MVAC distribution grid.

If the magnitude of MVAC PCC voltages violate the limits, the ST operates in voltage control mode to improve the PCC voltage. The reactive power injection capability of ST MV converter depends on the active power loading on the converter. In this chapter, the aim is to coordinate the operations of ST LV and BESS converters for improving the reactive power injection capability of ST MV converter. The rms value of the PCC voltage (V_t) is compared with the reference (V_t^*) and passed through a PI controller to generate the reactive power requirement (Q_{mv-req}) as given by [99]

$$Q_{mv-req} = K_{p-q}(V_t^* - V_t) + K_{i-q}\int (V_t^* - V_t)dt \tag{2.5}$$

where K_{p-q} and K_{i-q} are the proportional and integral gains of the PI controller. The exchange of required amount of reactive power is not ensured, because of the limitation in rating of ST MV converter. In addition, the available reactive power margin with ST MV converter depends on the ST LVAC loading at the time of sag/swell.

The reactive power injection capability of ST MV converter is improved with the help of ST LV converter and BESS. The P^*_{mv} consists of the P^*_{loss} and P^*_{lv}. Using P^*_{mv} and Q_{mv-req} which is equal to Q^*_{mv}, the total reference currents are generated using (2.4). If the currents are within the maximum current rating of the ST MV converter, the required P^*_{mv} and Q_{mv-req} are supplied by the ST MV converter. If the currents violate the rating, the magnitude of Q_{mv-req} is compared with the ST MV converter apparent power rating S_{mv}. If the Q_{mv-req} is greater than or equal to the S_{mv}, a limiting magnitude of reactive power (Q_{mv-lim}) is exchanged with the MVAC grid. The P^*_{mv} is equal to P^*_{loss} which is required for maintaining reference MVDC link voltage. The BESS provides entire active power requirement of ST LVAC loads. The ST LV converter reduces the voltage magnitude to 90% of the nominal value at the LVAC bus which effectively reduces the BESS power requirement.

If the Q_{mv-req} is lower than S_{mv}, the limiting active power magnitude (P_{mv-lim}) is found out. The voltage control at the ST LVAC side modifies LVAC power requirement. The LVAC voltage is controlled using the control index (n). From the P_{mv-lim}, the control index n is calculated as

$$n = \sqrt{\frac{P_{mv-lim} - P^*_{loss}}{P^*_{lv}}}. \tag{2.6}$$

The value of n provides the information about the requirement of load reduction for releasing the active power loading on ST MV converter. If this value is lower than 0.9, it indicates the requirement of BESS for the load support. Because, as per grid codes [103], a minimum of 90% voltage magnitude is required in the LVAC grid for satisfactory operation of loads. Therefore, minimum value of n is limited to 0.9 and if the calculated n is lesser than or equal to 0.9, then n is fixed at 0.9. In this condition, the P^*_{mv} is given as P_{mv-lim} and BESS supplies the remaining active power. Therefore, the reactive power reference Q^*_{mv} given to the controller is same as Q_{mv-req}. If the calculated n is greater than 0.9, the actual value is supplied to the ST LV converter and the voltage magnitude is maintained based on n. As per the value of n, the active power load on ST LV converter reduces. In this condition, the P^*_{mv} supplies the P^*_{loss} and modified LVAC active power. In this case also, Q^*_{mv} is equal to Q_{mv-req}.

Based on the conditions explained in the above section, the appropriate P^*_{mv} and Q^*_{mv} are selected. These reference powers are used in (2.2) and (2.3) to generate reference currents. For calculating the total reference currents, (2.4) is used. These reference currents are converted into *abc* reference frame (i^*_{mva}, i^*_{mvb}, i^*_{mvc}). The reference and actual phase currents of ST MV converter are used in a hysteresis current controller to generate the switching states for the ST MV converter as shown in Fig. 2.6 [71], [72].

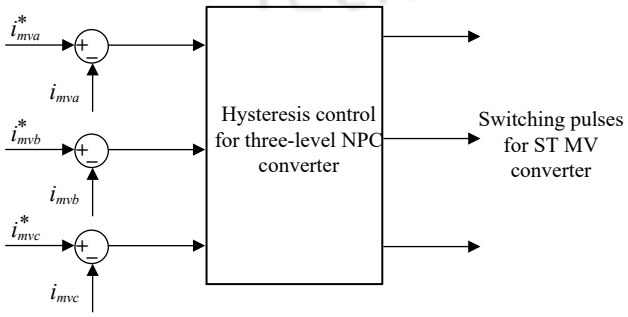

Fig. 2.6 Block-diagram of hysteresis current controller for ST MV converter [71], [72].

2.2.2 ST DC-DC Converter Control

This converter is operated to maintain the LVDC link voltage at the reference value which ensures constant power flow between MVDC and LVDC links of ST. The reference LVDC voltage (V^*_{lv-dc}) is compared with the actual value (V_{lv-dc}) and passed through a PI controller to generate a phase angle (δ^*_{dc-dc}) as given by

$$\delta^*_{dc-dc} = K_{p-dc}(V^*_{lv-dc} - V_{lv-dc}) + K_{i-dc}\int (V^*_{lv-dc} - V_{lv-dc})dt \tag{2.7}$$

where K_{p-dc} and K_{i-dc} are the proportional and integral gains of the PI controller. A phase angle difference of δ^*_{dc-dc} between the pulsed voltages of MVDC and LVDC links ensures the necessary power transfer between them. The power transferred (P_{dc-dc}) from one side of the converter to the other side is given as follows [59]:

$$P_{dc-dc} = \frac{V_{mv-dc}V_{lv-dc}}{2\pi f_{dc}L_{dc}}\delta^*_{dc-dc}(1 - \frac{|\delta^*_{dc-dc}|}{\pi}) \tag{2.8}$$

where V_{mv-dc} is the MVDC link voltage, f_{dc} is the switching frequency of the DC-DC converter, and L_{dc} is the equivalent inductance.

2.2.3 ST LV Converter Control

The ST LV converter maintains a constant voltage at the ST LVAC bus similar to a grid forming converter [9]. At any operating time, the reference rms voltage (V^*_{lv}) for ST LV converter is given by

$$V^*_{lv} = nV_{lv-nom}, \quad \text{where} \quad 1 \geq n \geq 0.9 \tag{2.9}$$

where V_{lv-nom} is the nominal voltage magnitude and n is controlled depending upon the operating scenario. During normal operating conditions, this converter maintains a three-phase sinusoidal balanced voltage with nominal rms value of 1.0 p.u, where n is maintained at 1. The coordinated operation proposed in this chapter requires the ST LV converter load control. A method is proposed in [75] for using the sensitivity identification for the load control. Considering a constant impedance load at the ST LVAC side [106], the load active power variation (ΔP_L) can be written in terms of voltage

change as

$$\Delta P_{lv} \propto V_{lv-nom}^2 - V_{lv}^2 \tag{2.10}$$

where V_{lv} is the modified rms voltage reference. Therefore, a reduction in LVAC voltage results in corresponding reduction in active power. This strategy is utilized in this chapter to control the ST LV converter during MVAC grid voltage sags/swells. During coordinated operation, the LV converter is dynamically controlled to reduce the magnitude of voltage (V_{lv}^*) from 1.0 p.u. to 0.9 p.u. depending upon the operating scenario defined in Fig. 2.4 and Fig. 2.5. The reference voltage is used to generate three-phase reference voltages (v_{lva}^*, v_{lvb}^*, and v_{lvc}^*) as given by

$$\begin{aligned} v_{lva}^* &= V_{lv}^* \sqrt{2} \sin(\omega t) \\ v_{lvb}^* &= V_{lv}^* \sqrt{2} \sin(\omega t - 2\pi/3). \\ v_{lvc}^* &= V_{lv}^* \sqrt{2} \sin(\omega t + 2\pi/3) \end{aligned} \tag{2.11}$$

The reference voltages are used in a deadbeat control to generate a reference discrete voltage control law. The voltage is regulated around a hysteresis band to generate switching pulses [96].

2.2.4 BESS DC-DC Converter Control

During the normal grid operating conditions, the BESS is charged to maintain the appropriate SOC by absorbing power from the MVAC grid. In order to ensure that the BESS is charging with the reference power, the ST MV converter absorbs the power (P_{mv}^*) from the MVAC grid given by

$$P_{mv}^* = P_{lv}^* + P_{loss}^* + P_b^* \tag{2.12}$$

where P_b^* is the BESS power reference. During the grid voltage disturbance, the BESS is activated to supply active power. Depending upon the Q_{mv-req} magnitude and ST LVAC power requirement, the BESS power requirement changes and the P_b^* in different scenarios are shown in the Fig. 2.5. In the first case, the ST does not require the support from BESS. In the second case, the modified ST LVAC active power is supplied entirely from BESS. In the third case, since the ST LV converter load control provides sufficient

reactive power margin to the ST MV converter and the BESS power requirement remains zero. In the final case, the BESS power reference is given by

$$P_b^* = P_{lv}^* + P_{loss}^* - P_{mv-lim}. \tag{2.13}$$

The BESS power reference generated is related to the battery current reference (I_b^*) and voltage across the battery (V_b) by

$$P_b^* = V_b I_b^* \tag{2.14}$$

Considering a constant voltage, the BESS power reference is compared with the actual power (P_b) and passed through a PI controller to generate the duty cycle required for generating switching pulses [107].

2.3 ANALYSIS AND IMPACT OF COORDINATED VOLTAGE SUPPORT

The voltage support strategy using the coordinated operation is given in the flowchart in Fig. 2.4, and explained through the block-diagram given in Fig. 2.5. For analyzing the effectiveness of the proposed voltage support strategy, three cases are explained in this section. The MVDC link power loss component is neglected in this analysis. The base power is chosen as 1 MVA and base voltage as 11-kV. Grid reactance and resistance are 0.1038 p.u. and 0.00826 p.u., respectively. The ST MV converter rating is considered as 1.1 p.u. Asymmetrical voltage sags/swells are not considered in this study, and it requires the control of active and reactive powers in positive and negative sequences [101]. A higher X/R ratio is chosen to show the improvement in voltage for the proposed strategy [101]. However, the concept introduced in this chapter is not dependent on the grid reactance value since it addresses the issue of improving the reactive power injection capability of the ST MV converter. A generalized expression for MVAC PCC voltage magnitude (V_t) is developed in terms of active, reactive powers, grid impedance and MVAC grid voltage magnitude (V_g). The voltage magnitude is used to analyze the effect of BESS and ST LV converter load control on the MVAC PCC voltage during symmetrical grid voltage sags and swells. In the first case, only BESS is

used to support the ST MV converter. In the second case, the ST LV converter voltage control is used with ST MV converter. Third case combines the effects of both BESS and ST LV converters, and the coordinated operation is explained.

2.3.1 Voltage Support with BESS Control

This case analyzes the operation with the support of BESS. The ST LV converter control is not considered in this analysis. P_{mv} and Q_{mv} are the active and reactive power loading at the ST MV converter, respectively. P_b is the power supplied by the BESS. R_s and X_s are the grid resistance and reactance, respectively. The MVAC grid voltage is $\overline{V}_g$ and the MVAC PCC voltage is $\overline{V}_t$. Considering the grid voltage as reference, the PCC voltage as $V_t \angle \delta$ and applying Kirchhoff's law in the circuit,

$$V_t \angle \delta = V_g - \frac{(P_{mv} - jQ_{mv})}{V_t \angle -\delta}(R_s + jX_s). \tag{2.15}$$

Expanding (2.15) to eliminate δ and rearranging in terms of V_t result in

$$V_t^4 + 2V_t^2[(P_{mv}R_s + Q_{mv}X_s) - 0.5V_g^2] + [(P_{mv}^2 + Q_{mv}^2)(R_s^2 + X_s^2)] = 0. \tag{2.16}$$

In order to solve (2.16), a temporary variable is defined as $f = V_t^2$. Therefore, (2.16) shall be written as

$$f^2 + 2f[(P_{mv}R_s + Q_{mv}X_s) - 0.5V_g^2] + [(P_{mv}^2 + Q_{mv}^2)(R_s^2 + X_s^2)] = 0. \tag{2.17}$$

Out of the two solution, the favourable solution to (2.17) is

$$f = \frac{-h_2 + \sqrt{h_2^2 - 4h_1h_3}}{2h_1}$$

where

$$\begin{aligned} &h_1 = 1, \quad h_2 = 2[(P_{mv}R_s + Q_{mv}X_s) - 0.5V_g^2], \\ &h_3 = (P_{mv}^2 + Q_{mv}^2)(R_s^2 + X_s^2). \end{aligned} \tag{2.18}$$

Considering only positive value for V_t as a realistic solution, (2.18) is re-written as

$$V_t = \sqrt{\frac{-h_2 + \sqrt{h_2^2 - 4h_1h_3}}{2h_1}}. \tag{2.19}$$

If BESS is activated to supply the LVAC load power (P_{lv}), the active power requirement from the ST MVAC side is written as

$$P_{mv} = P_{lv} - P_b. \tag{2.20}$$

The rating of ST MV converter (S_{mv}) is related to the active and reactive power as:

$$S_{mv}^2 = P_{mv}^2 + Q_{mv}^2. \tag{2.21}$$

Applying the conditions of (2.20) and (2.21) in (2.19)

$$V_t = \sqrt{\frac{-H_2 + \sqrt{H_2^2 - 4H_1H_3}}{2H_1}}$$

where

$$\begin{aligned} H_1 &= 1, \\ H_2 &= 2[(P_{lv} - P_b)R_s + (\sqrt{S_{mv}^2 - (P_{lv} - P_b)^2})X_s - 0.5V_g^2], \\ H_3 &= ((P_{lv} - P_b)^2 + (S_{mv}^2 - (P_{lv} - P_b)^2))(R_s^2 + X_s^2). \end{aligned} \tag{2.22}$$

The MVAC PCC voltage magnitude for the corresponding active and reactive power injections is calculated using (2.22). The utilization of BESS for load control improves the voltage support capability of ST MV converter during grid voltage disturbances.

2.3.2 Voltage Support with LVAC Voltage Control

The voltage control at the LVAC side can be used for load active and reactive power control [75]. We consider constant impedance load at the LVAC side and V_{lv-nom} is the magnitude of the nominal terminal voltage. The LVAC side voltage reduction results

in the proportional reduction of current and thereby reduction in active and reactive powers. If n is the control variable and grid codes allow 10% variation in voltage at the LVAC side, then

$$V_{lv} = nV_{lv-nom}, \quad \text{where} \quad 1 > n \geq 0.9. \tag{2.23}$$

This dynamic reduction of voltage results in corresponding reduction in active and reactive powers [75]. Since only active power is supplied from the MVAC grid, the following equation can be written for the new active power requirement

$$P_{lv-mod} = n^2 P_{lv}. \tag{2.24}$$

The BESS power supply in this case is assumed as zero. Therefore, (2.20) is modified to

$$P_{mv} = P_{lv-mod}. \tag{2.25}$$

This reduction in active power absorption from grid results in availability of higher reactive power injection capability and (2.21) is modified to

$$Q_{mv-mod} = \sqrt{S_{mv}^2 - P_{lv-mod}^2}. \tag{2.26}$$

The load control using ST LV converter improves the reactive power margin available with the ST MV converter during voltage disturbances and this extra reactive power injection helps in improving the voltage support capability in the MVAC grid.

2.3.3 Voltage Support with Coordinated BESS and LVAC Voltage Control

In this case, the ST LVAC voltage control is used. Due to the dynamic reduction in voltage, the active power loading at the LVAC side is also modified. Therefore, the coordinated control improves the MVAC PCC voltage with a reduced active power requirement from BESS. Considering these conditions, the new active power requirement from the MVAC grid is given as

$$P_{mv-mod} = P_{lv-mod} - P_b. \tag{2.27}$$

The simultaneous support of ST LVAC load control and BESS modifies the MVAC grid active power absorption as per (2.27). For this active power, the reactive power margin is determined by modifying (2.21) into

$$Q_{mv-mod} = \sqrt{S_{mv}^2 - (P_{lv-mod} - P_b)^2}. \tag{2.28}$$

Therefore, (2.22) shall be modified based on the (2.28) to obtain improved PCC voltage magnitude in case of coordinated operation. Load control using coordinated operation of BESS and ST LV converter reduces the BESS power required for achieving same voltage support at the MVAC grid. Following examples illustrate the voltage support performances of ST with coordinated and non-coordinated operations during symmetrical grid voltage sag and swell.

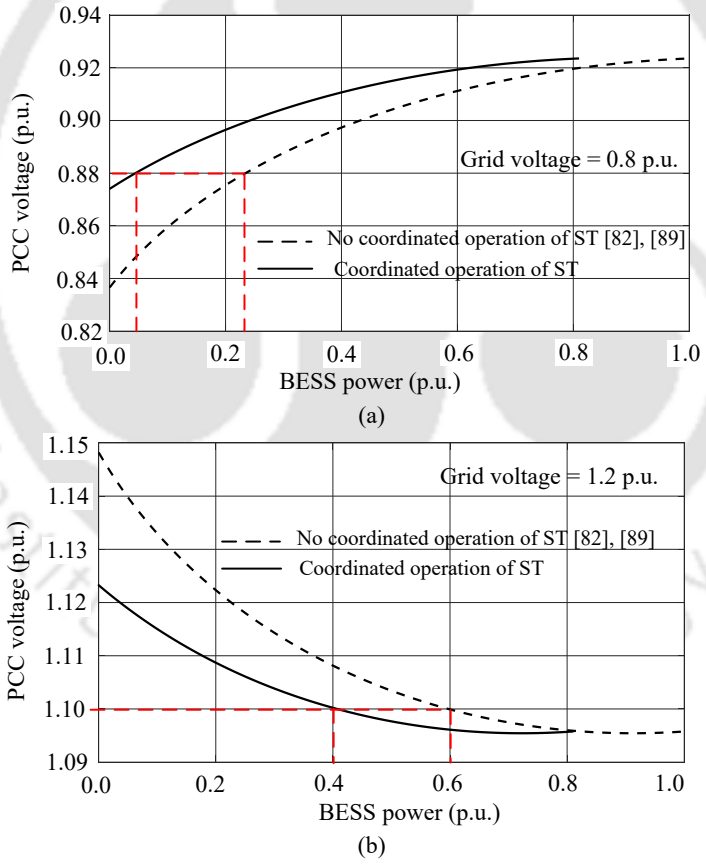

Fig. 2.7 Comparison of voltage support performance using ST (a) during a symmetrical grid voltage sag. (b) during a symmetrical grid voltage swell.

Example-1: Voltage sag

Fig. 2.7(a) shows the MVAC PCC voltage magnitude with and without coordinated operation of ST during an MVAC grid voltage sag of 20%. The voltage magnitude is plotted for different BESS injections. For the coordinated operation, the LVAC side voltage is kept at 0.9 p.u, which causes a lower active power requirement from the LVAC load. It is evident from the graph that, coordinated operation reduces the BESS power requirement for the improving of the PCC voltage magnitude to 0.88 p.u.

Example-2: Voltage swell

Fig. 2.7(b) shows the MVAC PCC voltage magnitude with and without coordinated operation of ST during an MVAC grid voltage swell 20%. The voltage magnitude is plotted for different BESS injections. For the coordinated operation, the LVAC side voltage is kept at 0.9 p.u, which causes a lower active power requirement from the LVAC load. It is evident from the graph that, coordinated operation reduces the BESS power requirement for the reduction of voltage magnitude to 1.1 p.u.

Table 2.1 shows different voltage support strategies using ST and their performance during a grid voltage sag of 20%. For a fixed rating of the ST MV converter, the achievable PCC voltage using different strategies are given. The coordinated operation with BESS and LVAC control achieves the required voltage with a reduced BESS power as given in the case 4 in Table 2.1. The BESS power reduction observed from Table 2.1 is the value obtained at a specific system condition. The percentage reduction depends on the operating voltage levels and load power magnitude.

2.4 SIZING OF DIFFERENT POWER CONVERTERS

In this section, the power rating of different ST converters and BESS converter is explained.

Table 2.1 Comparison of Parameters for Different Voltage Control Methods Using ST

Sl. No.	Control		MV converter reactive power (p.u.)	BESS power (p.u.)	LVAC voltage (p.u.)	PCC voltage (p.u.)
	LVAC voltage	BESS				
1 [108]	No	No	0.4583	NA	1	0.8366
2 [82], [89]	No	Yes	0.7952	0.24	1	0.88
3	Yes	No	0.7442	NA	0.9	0.874
4	Yes	Yes	0.7952	0.05	0.9	0.88

2.4.1 Power Converters of ST

The ST LV converter is designed to cater the entire active, reactive, and harmonic power of the LVAC grid. The maximum active power loading on ST LV converter is 1 p.u. Considering a maximum power factor of 0.95, the rating of this converter is selected as 1.05 p.u. The ST DC-DC converter is designed to carry the entire active power requirement at the LVAC side and BESS maximum charging/discharging power. Considering the BESS charging is not scheduled at peak LVAC load conditions, this converter is rated as 1 p.u. The ST MV converter is required to deliver the active power at the LVAC side and reactive power to the MVAC grid. Considering a maximum active power of 1 p.u., rating of ST MV converter is selected as 1.1 p.u.

2.4.2 BESS Converter

The rating of BESS converter required with and without coordinated operation is calculated during a voltage sag of 20% magnitude. During operation without coordination with ST LV converter, the BESS power requirement depends on the maximum active power ST MV converter is capable of exchanging after supplying the necessary reactive power to the MVAC grid. From (2.13), the BESS requirement neglecting P^*_{loss} for the non-coordinated operation can be written as

$$P_b = P_{lv} - P_{mv-lim}. \tag{2.29}$$

During the coordinated operation of ST MV converter with ST LV converter, the load control at the ST LVAC terminal reduces the active power requirement at the ST LVAC grid. The modified loading on ST MV converter is as per (2.24). Therefore, the modified BESS rating is given as

$$P_{b-mod} = n^2 P_{lv} - P_{mv-lim}. \tag{2.30}$$

Comparing (2.29) and (2.30) for the same voltage support, the BESS power demand is found to be smaller in coordinated operation as compared to the non-coordinated operation. For the mitigation of a 20% symmetrical voltage sag, the BESS rating is found to be 0.05 p.u. for coordinated operation and 0.24 p.u. for operation without

Table 2.2 Simulation Parameters

System quantities	Values
MVAC voltage	11 kV
LVAC voltage	0.4 kV
ST MV converter	L_{mv} = 20 mH, C_{mv} = 5 μF, R_{mv} = 30 Ω
ST LV converter	L_{lv} = 0.5 mH, C_{lv} = 20 μF
DC link voltage	V_{mv-dc} = 30 kV, V_{lv-dc} = 1.2 kV
DC link capacitor	C_{mv-dc} = 2000 μF, C_{lv-dc} = 2500 μF
ST DC-DC converter	L_{mvdc} = 10 mH, f_{sw} = 1 kHz
BESS DC-DC converter	L_b = 50 μH, f_{sw} = 10 kHz
MVDC link PI controller	K_{p-l} = 25 , K_{i-l} = 0.1

coordination.

2.5 SIMULATION RESULTS

Simulations are carried out using the PSCAD/EMTDC software. The simulation parameters are given in Table 2.2. Four cases are analyzed in simulation.

2.5.1 Non-coordinated Operation During Grid Voltage Sag

Fig. 2.8 shows the performance with non-coordinated operation during a symmetrical MVAC grid voltage sag of 20%. Before $t = 0.4$ s, the ST is operating in normal condition supplying the LVAC loads by absorbing the active power from MVAC grid. During sag, the MVAC voltage is supported with the ST MV converter reactive power injection. This case shows the operation without coordination, and the ST LV converter maintains the LVAC voltage at nominal value. The BESS supports the LVAC load to release the rating of ST MV converter during voltage sag. The MVAC grid voltage experiences a 20% symmetrical sag at t = 0.4 s as shown in Fig. 2.8(a). The PCC voltages with improved magnitude during voltage sag is shown in Fig. 2.8(b). The ST MV converter currents are maintained at the maximum rating as shown in Fig. 2.8(c). The LVAC voltage and load currents remain constant throughout the operation as shown in Fig. 2.8(d) and (e), respectively. The MV and LV DC link voltages are shown in Fig. 2.8(f)

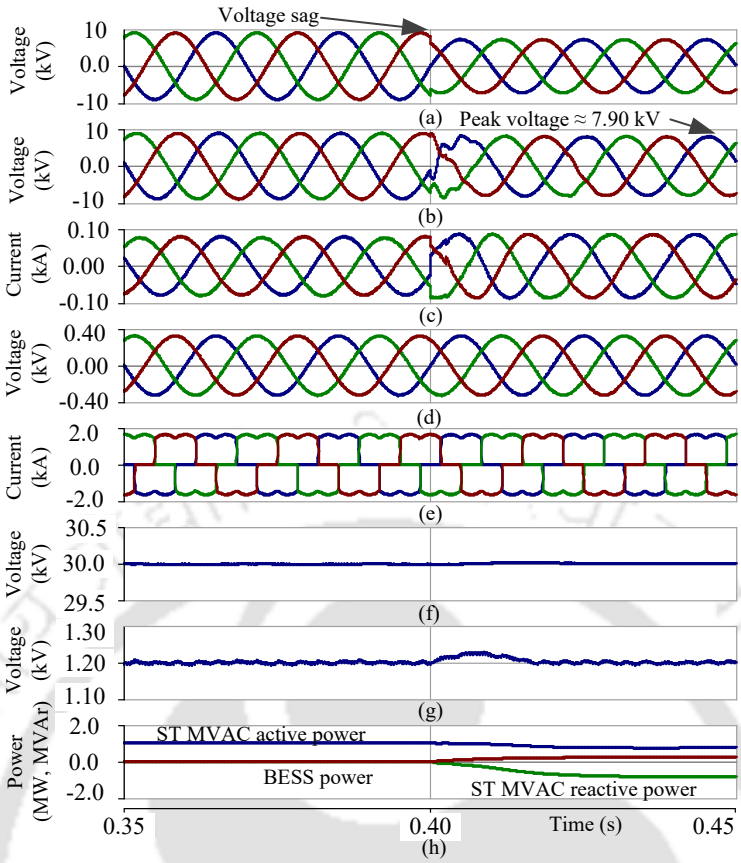

Fig. 2.8 Voltage support during symmetrical grid voltage sag without coordinated control of ST LV converter and BESS. (a) MVAC grid voltages. (b) MVAC PCC voltages. (c) ST MV converter currents. (d) ST LVAC voltages. (e) LVAC load currents. (f) MVDC link voltage. (g) LVDC link voltage. (h) Different powers.

and (g), respectively, and they are maintained at their constant reference values. Fig. 2.8(h) shows the ST MVAC active power, ST MVAC reactive power and BESS power during the operation. The ST MVAC active power reduces after t = 0.4 s as the BESS supports the LVAC active power. The ST MVAC reactive power increases to support the voltage at MVAC grid.

2.5.2 Coordinated Operation During Grid Voltage Sag

Fig. 2.9 shows the performance with coordinated operation during a 20% symmetrical MVAC grid voltage sag. Till t = 0.4 s, the ST MV converter absorbs the active power from MVAC grid to supply the LVAC loads. During sag, the operation of ST MV converter is coordinated with ST LV converter and BESS, resulting in a reduced BESS requirement. The MVAC grid voltage experiences a symmetrical sag at t = 0.4 s as shown in Fig. 2.9(a). In Fig. 2.9(b), the PCC voltages are shown with improved

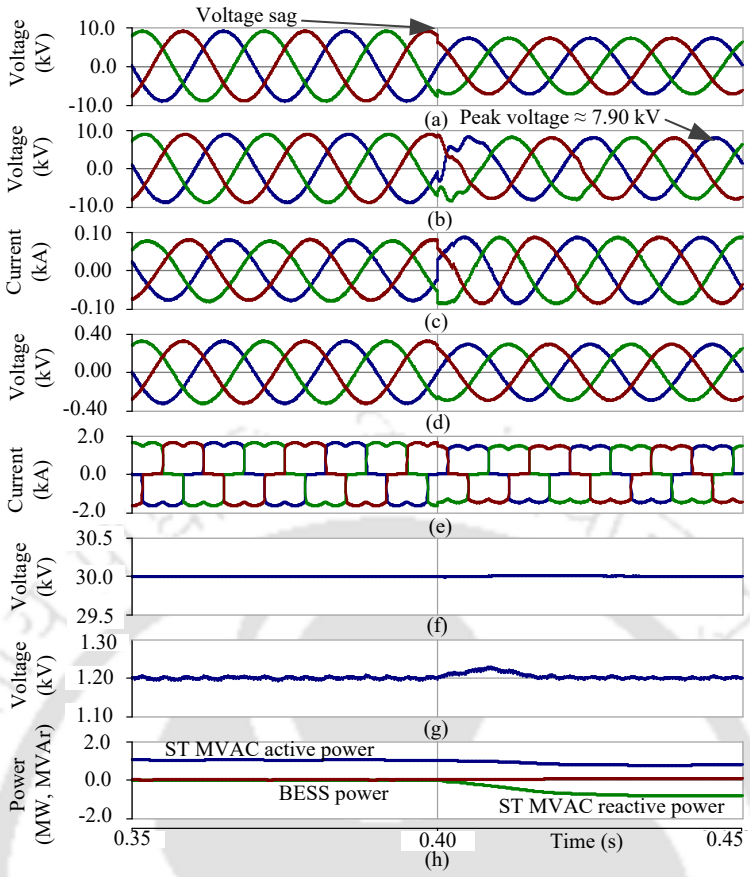

Fig. 2.9 Voltage support during symmetrical grid voltage sag with coordinated control of ST LV converter and BESS. (a) MVAC grid voltages. (b) MVAC PCC voltages. (c) ST MV converter currents. (d) ST LVAC voltages. (e) LVAC load currents. (f) MVDC link voltage. (g) LVDC link voltage. (h) Different powers.

magnitude during voltage sag. The ST MV converter currents are maintained at the maximum rating as shown in Fig. 2.9(c). The ST LV converter voltage control is realized in coordinated operation, and the voltage reduces to 90% of the nominal value after t = 0.4 s as shown in Fig. 2.9(d). Corresponding load currents are shown in Fig. 2.9(e). The voltages of MV and LV DC links are shown in Fig. 2.9(f) and (g), respectively for coordinated operation. Fig. 2.9(h) shows the ST MVAC active power, ST MVAC reactive power and BESS power during the operation. The ST MVAC reactive power increases to support the MVAC grid voltage. The BESS power injection reduces as compared to the Fig. 2.8(h).

2.5.3 Non-coordinated Operation During Grid Voltage Swell

Fig. 2.10 shows the performance with non-coordinated operation during a symmetrical MVAC grid voltage swell of 20%. The ST MV converter absorbs the active power

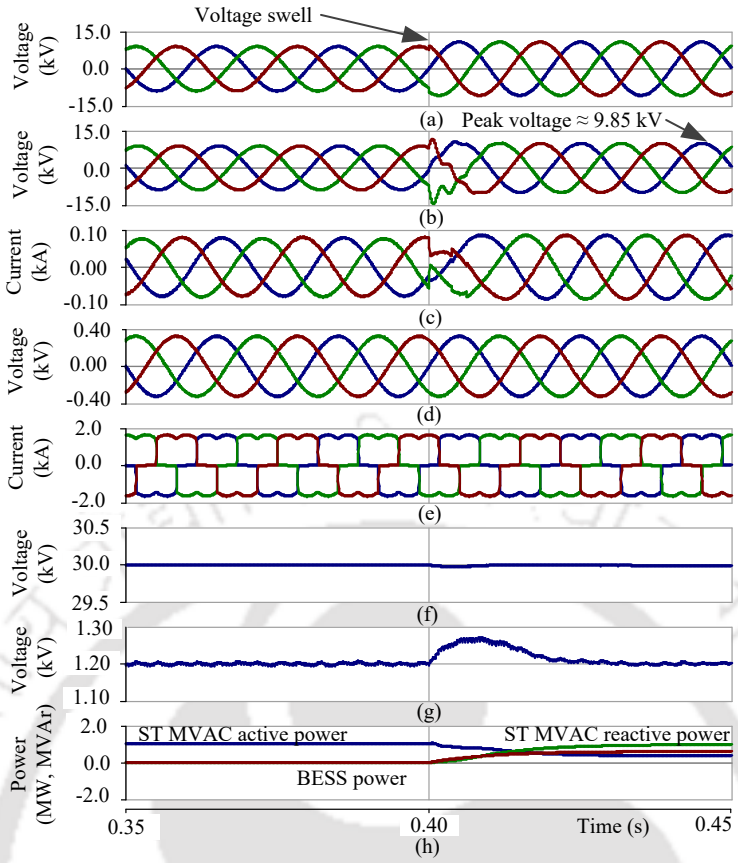

Fig. 2.10 Voltage support during symmetrical grid voltage swell without coordinated control of ST LV converter and BESS. (a) MVAC grid voltages. (b) MVAC PCC voltages. (c) ST MV converter currents. (d) ST LVAC voltages. (e) LVAC load currents. (f) MVDC link voltage. (g) LVDC link voltage. (h) Different powers.

from MVAC grid to supply the LVAC loads till t = 0.4 s. During swell, the voltage is supported with the ST MV converter reactive power injection. This case shows the operation without coordination, and the ST LV converter maintains the LVAC voltage at nominal value. The BESS supports the LVAC load to release the rating of ST MV converter during voltage swell. The MVAC grid voltage experiences a swell at t = 0.4 s as shown in Fig. 2.10(a). In Fig. 2.10(b), the PCC voltages are maintained at 1.1 p.u. during grid voltage swell. Fig. 2.10(c) shows the ST MV converter currents, and the magnitude is maintained at the maximum rating. The LVAC voltages and load currents remain constant throughout the operation as shown in Fig. 2.10(d) and (e), respectively. The MV and LV DC link voltages are shown in Fig. 2.10(f) and (g), respectively. These voltages are maintained at their respective reference values before and after the grid voltage swell. Fig. 2.10(h) shows the ST MVAC active power, ST MVAC reactive power and BESS power during the operation. The BESS supports the ST MV converter, and ST MVAC active power reduces. During swell, the ST MV converter exchanges

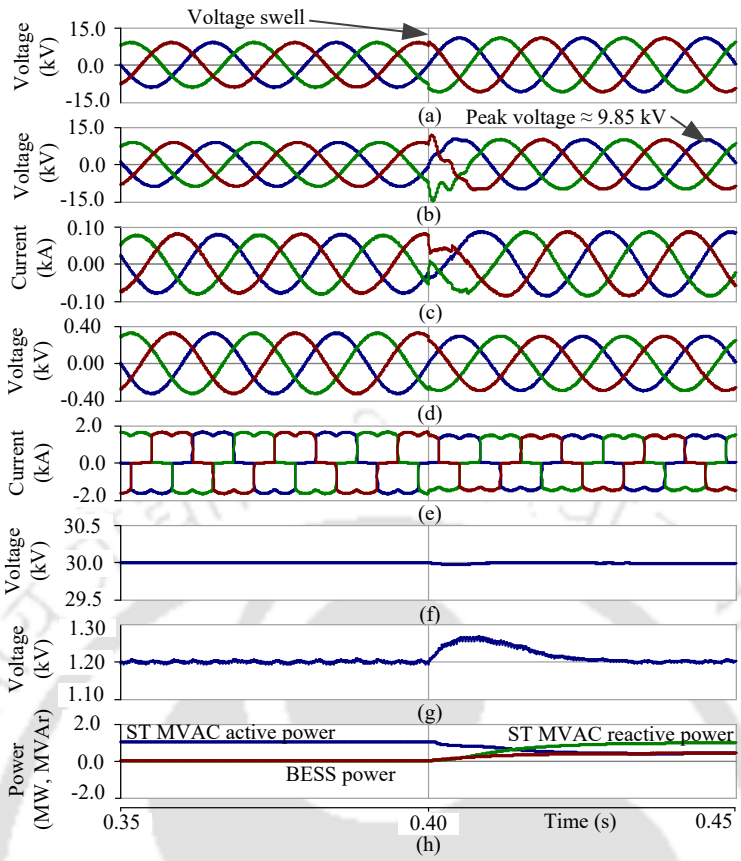

Fig. 2.11 Voltage support during symmetrical grid voltage swell with coordinated control of ST LV converter and BESS. (a) MVAC grid voltages. (b) MVAC PCC voltages. (c) ST MV converter currents. (d) ST LVAC voltages. (e) LVAC load currents. (f) MVDC link voltage. (g) LVDC link voltage. (h) Different powers.

reactive power to support the voltage as shown in Fig. 2.10(h).

2.5.4 Coordinated Operation During Grid Voltage Swell

Fig. 2.11 shows the performance with coordinated operation during a 20% symmetrical MVAC grid voltage swell. Till t = 0.4 s, the active power is absorbed from the MVAC grid by the ST MV converter to supply the LVAC loads. No reactive power is exchanged with MVAC grid. During swell, the ST MV converter exchanges reactive power with the MVAC grid. Because of the coordinated operation of ST MV, ST LV and BESS converters, the BESS power requirement reduces as compared to the operation without coordination. The MVAC grid voltage experiences a 20% symmetrical swell at t = 0.4 s as shown in Fig. 2.11(a). In Fig. 2.11(b), the PCC voltages are shown with improved magnitude during grid voltage swell. The ST MV converter currents are maintained at the maximum rating as shown in Fig. 2.11(c). The LV converter voltage control is

Table 2.3 Experimental Parameters

System quantities	Values
MVAC grid voltage	150 V
LVAC grid voltage	110 V
MVAC line parameters	L_s = 8 mH
ST MV converter	L_{mv} = 13 mH, C_{mv} = 10 μF
ST LV converter	L_{lv} = 5 mH, C_{lv} = 10 μF
DC link voltage	V_{dc} = 270 V
BESS converter	L_b = 10 mH
LV side rectifier load	50 Ω

realized in coordinated operation and the voltage reduces to 90% of the nominal value after t = 0.4 s as shown in Fig. 2.11(d). Corresponding load currents are shown in Fig. 2.11(e). The MV and LV DC link voltages are shown in Fig. 2.11(f) and (g), respectively for coordinated operation. Fig. 2.11(h) shows the ST MVAC active power, ST MVAC reactive power and BESS power. The ST MVAC reactive power is injected to maintain the PCC voltage within the maximum allowable limit. The BESS power injection reduces as compared to the Fig. 2.10(h).

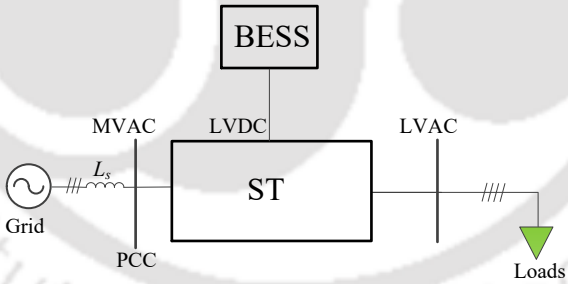

Fig. 2.12 Experimental setup schematic.

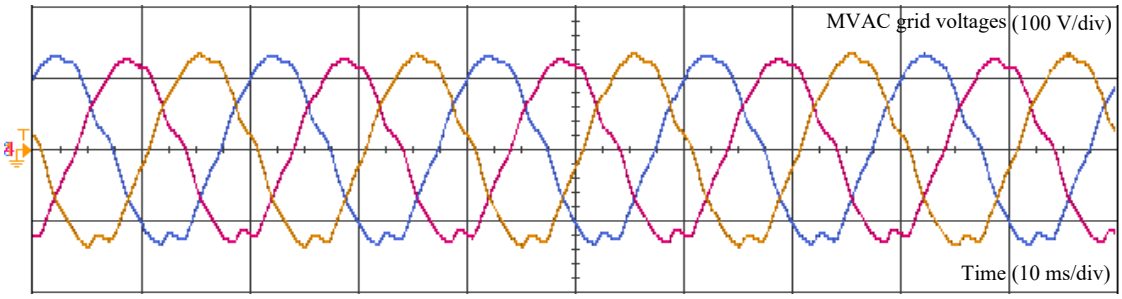

Fig. 2.13 Waveform of MVAC grid voltages.

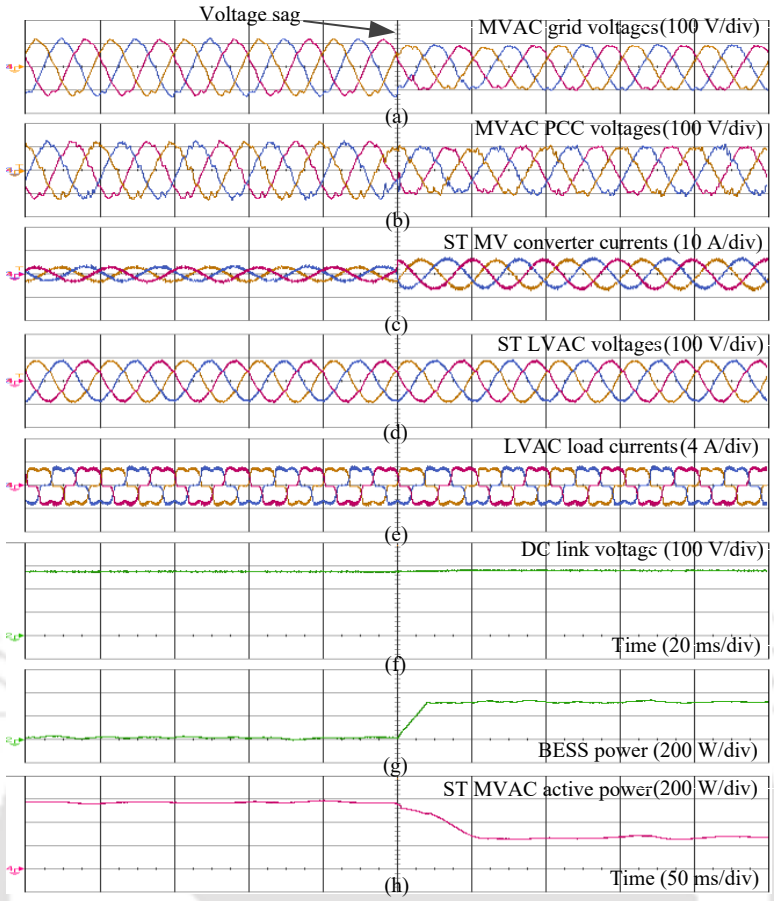

Fig. 2.14 Experimental results for symmetrical voltage sag without coordinated operation. (a) MVAC grid voltages. (b) MVAC PCC voltages. (c) ST MV converter currents. (d) ST LVAC voltages. (e) LVAC load currents. (f) DC link voltage. (g) BESS power. (h) ST MVAC active power.

2.6 EXPERIMENTAL RESULTS

Fig. 2.12 shows the experimental setup schematic. The grid voltages contain harmonics and due to the interconnection through step-down transformer, the voltage waveform is not smooth [88]. This is visible in the waveforms shown in Fig. 2.13, and the present work does not consider any improvement strategies for this particular problem. Moreover, this problem does not affect the performance of the proposed method. The experimental parameters are given in Table 2.3. The AC filter capacitor used in the experimental setup helps in reducing the effects of harmonics in voltage. It also provides support during grid voltage sag. However, a higher capacitance value may reduce the impedance offered at fundamental frequency, and may absorb higher magnitude of fundamental component of reactive current. This may affect the performance during grid voltage swell. Similar to the simulation, four cases are analyzed in the experimental study.

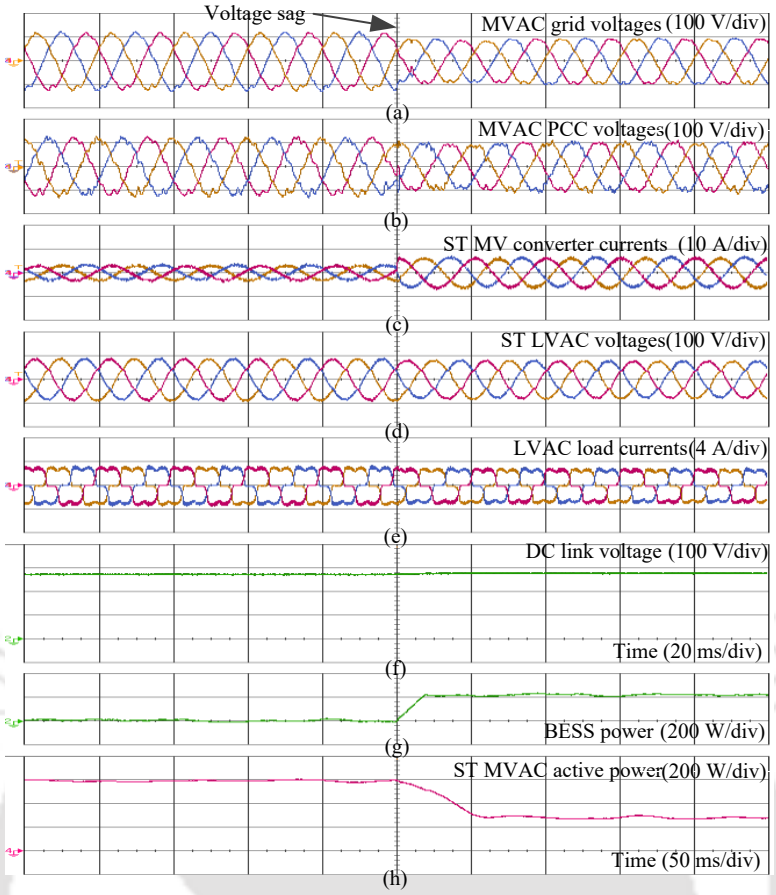

Fig. 2.15 Experimental results for symmetrical voltage sag with coordinated operation. (a) MVAC grid voltages. (b) MVAC PCC voltages. (c) ST MV converter currents. (d) ST LVAC voltages. (e) LVAC load currents. (f) DC link voltage. (g) BESS power. (h) ST MVAC active power.

2.6.1 Non-coordinated Operation During Grid Voltage Sag

The experimental waveforms for the non-coordinated operation are shown in Fig. 2.14 during a MVAC grid voltage sag of 20%. Before the sag, the ST MV converter absorbs the active power from MVAC grid to supply the LVAC loads. The MVAC grid voltage experiences a voltage sag as shown in Fig. 2.14(a). The corresponding improved PCC voltages are shown in Fig. 2.14(b). The ST MV converter currents are shown in Fig. 2.14(c). The ST LVAC voltages and load currents are shown in Fig. 2.14(d), and (e), respectively. In non-coordinated operation, the ST LV converter maintains the LVAC voltage at the nominal value during MVAC grid voltage sag. The DC link voltage is shown in Fig. 2.14(f), and it is maintained at the reference value. The BESS power increases to support the ST MV converter as shown in Fig. 2.14(g). The ST MVAC active power is shown in Fig. 2.14(h).

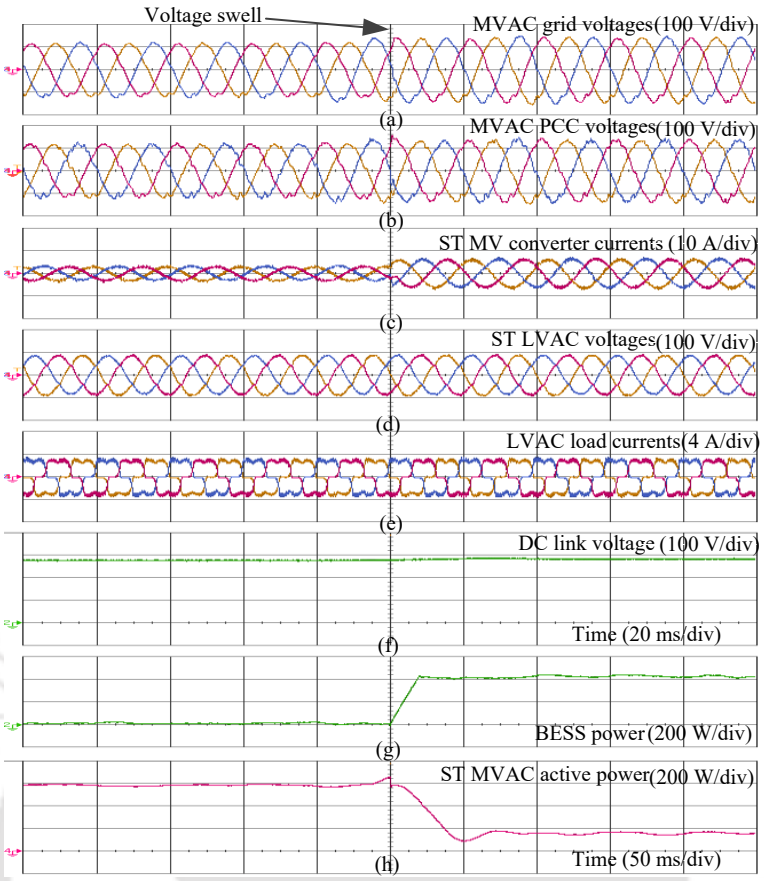

Fig. 2.16 Experimental results for symmetrical voltage swell without coordinated operation. (a) MVAC grid voltages. (b) MVAC PCC voltages. (c) ST MV converter currents. (d) ST LVAC voltages. (e) LVAC load currents. (f) DC link voltage. (g) BESS power. (h) ST MVAC active power.

2.6.2 Coordinated Operation During Grid Voltage Sag

The experimental waveforms for the coordinated operation are shown in Fig. 2.15 during MVAC grid voltage sag of 20%. The MVAC grid voltage experiences a voltage sag as shown in Fig. 2.15(a). The corresponding improved PCC voltages are shown in Fig. 2.15(b). The ST MV converter currents are shown in Fig. 2.15(c). The ST LVAC voltages and load currents are shown in Fig. 2.15(d), and (e), respectively. The LVAC voltage reduces to enable the load control, and the corresponding reduction in load currents are visible in Fig. 2.15(e). The DC link voltage is shown in Fig. 2.15(f). The BESS power is shown in Fig. 2.15(g), and the ST MVAC active power is shown in Fig. 2.15(h). The ST LV converter voltage control reduces the active power requirement at the LVAC bus. Therefore, the BESS power reduces in the coordinated operation as compared to the non-coordinated operation.

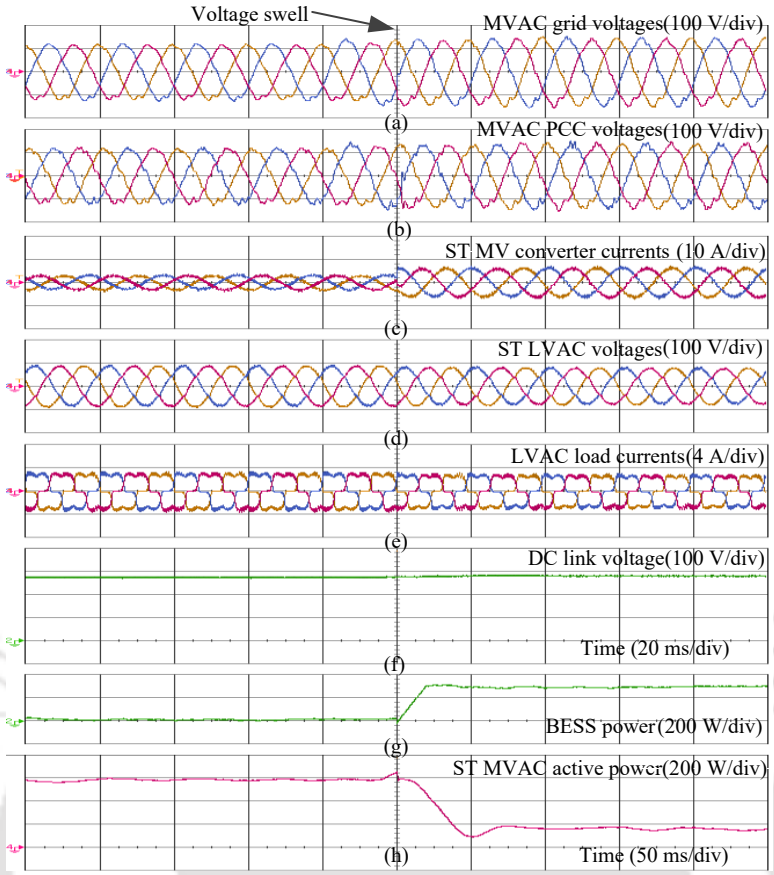

Fig. 2.17 Experimental results for symmetrical voltage swell with coordinated operation. (a) MVAC grid voltages. (b) MVAC PCC voltages. (c) ST MV converter currents. (d) ST LVAC voltages. (e) LVAC load currents. (f) DC link voltage. (g) BESS power. (h) ST MVAC active power.

2.6.3 Non-coordinated Operation During Grid Voltage Swell

The experimental waveforms for the non-coordinated operation are shown in Fig. 2.16 during an MVAC grid voltage swell of 20%. The active power is absorbed from the MVAC grid by the ST MV converter to supply the LVAC loads. The MVAC grid voltage experiences a voltage swell as shown in Fig. 2.16(a). The corresponding PCC voltages are shown in Fig. 2.16(b). The ST MV converter currents are shown in Fig. 2.16(c). The ST LVAC voltages and load currents are shown in Fig. 2.16(d), and (e), respectively. The LVAC voltage remain constant throughout the operation since the load control is not enabled in this mode of operation. The DC link voltage is shown in Fig. 2.16(f). The BESS power increases to support the ST MV converter as shown in Fig. 2.16(g). The ST MVAC active power is shown in Fig. 2.16(h).

2.6.4 Coordinated Operation During Grid Voltage Swell

The experimental waveforms for the coordinated operation are shown in Fig. 2.17 during a MVAC grid voltage swell of 20%. The MVAC grid voltage experiences a voltage swell as shown in Fig. 2.17(a). The corresponding improved PCC voltages are shown in Fig. 2.17(b). The ST MV converter currents are shown in Fig. 2.17(c). The ST LVAC voltages and load currents are shown in Fig. 2.17(d), and (e), respectively. The LVAC voltage reduces to enable the load control, and the corresponding reduction in load currents are visible in Fig. 2.17(e). The DC link voltage is shown in Fig. 2.17(f). The BESS power is shown in Fig. 2.17(g), and the ST MVAC active power is shown in Fig. 2.17(h). The ST LV converter load control reduces the LVAC active power requirement in coordinated operation. Therefore, BESS power reduces in the coordinated operation as compared to non-coordinated operation.

2.7 CONCLUSIONS

The proposed control algorithm utilizes the coordinated operation of the ST MV converter, ST LV converter and BESS to support the voltage at the MVAC grid. The analysis provided in this chapter confirms the advantages of proposed operation in comparison with the existing solutions. An improved reactive power injection capability of ST in the MVAC grid is achieved with the help of the BESS and LVAC voltage control. A reduction in the BESS rating is achieved with the coordinated operation in comparison with the non-coordinated operation. In addition, exploiting the ST LV converter and BESS capabilities of load control further establishes the potential of ST in distribution grid. These advantages are verified through simulation and experimental results.

CHAPTER 3

CAPACITY ENHANCEMENT OF A RADIAL DISTRIBUTION GRID USING SMART TRANSFORMER

In Chapter 2, capability of ST for MVAC grid voltage support is investigated. The reactive power capability enhancement of ST MV converter is achieved with the coordinated operation of the ST LV converter and BESS. However, reactive power injection from ST MV converter for voltage support is effective only in inductive grids. Moreover, the system configuration considered was a single-bus radial feeder. Moving further to a multiple-bus system, this chapter investigates the performance of ST in a 5-bus radial feeder with comparable resistance and reactance values.

Hosting capacity is defined as the maximum generation or load that can be integrated to the distribution system without violation of grid parameter limits such as voltage rise/drop, equipment overload, etc. [29], [94]. Accommodating more number of DGs and loads in the existing feeders without violating the grid-code specified power quality limits is a major challenge [19], [109]. Violation of the limits of steady-state voltage magnitude restricts the further load/DG inclusion in existing feeders. In order to improve the static hosting capability of feeders, several power management methods are proposed in the literature. The PV hosting capabilities of the distribution feeder are improved using STATCOM [93] and BESS [110], [111]. The EV load hosting capability improvement in an LVAC distribution grid is realized using distributed phase-shifting control [109]. The voltage sensitivity factors indicate the dependence of bus voltage magnitudes for a corresponding change in the active and reactive powers at a particular bus [112]. These factors are used to control the voltage rise by managing the active power flow from PV sources in radial distribution grids [113]. In [94], the sensitivity factors are utilized for enhancing the load/generation hosting capacity of a distribution system with the help of DC interconnection and BESS.

The hosting capability improvement using STATCOM is effective in distribution grids with a low R/X ratio, as it utilizes the reactive power exchange. Similarly, BESS based

systems are effective in the resistive grids. Utilization of DC lines for active power transfer involves the construction of extra DC infrastructure parallel to AC line. The application of PV converters for capacity enhancement involves active power curtailment, and this reduces the overall power extraction from the available solar energy.

From the literature mentioned above, the important observations are:

- The hosting capability improvement of distribution system is important to accommodate more DG and loads in the existing distribution system
- The improvement methods using independent active and reactive powers are effective in resistive and reactive distribution grids, respectively
- In multiple-bus radial distribution system, the voltage sensitivity to active and reactive powers is a measure to identify their impact on different bus voltages
- In MVAC distribution grids with comparable resistance and reactance values, both the active and reactive power injection strategies are effective in voltage support
- The ST is utilized for MVAC grid voltage support in a multiple-bus system [83], however the simultaneous active and reactive power exchange features are not considered with the presence of BESS.

In this chapter, the active and reactive power exchange potential of a BESS integrated ST is explored for hosting capacity enhancement of the MVAC grid. A 5-bus radial MVAC feeder is selected for validating the performance of the proposed method. The R/X ratio of the feeder is 0.85 [9]. The proposed method investigates the effectiveness of active power support, reactive power support and a flexible combination of both. A sensitivity-based sizing study for ST and BESS is proposed in this chapter. The method is verified in theoretical and simulation study for a 5-bus system, and the effectiveness is verified with experiments.

3.1 SYSTEM CONFIGURATION AND SENSITIVITY ANALYSIS

In the first part of this section, the conventional and proposed radial distribution system structures are explained. In the second part, an introduction to the sensitivity analysis is provided.

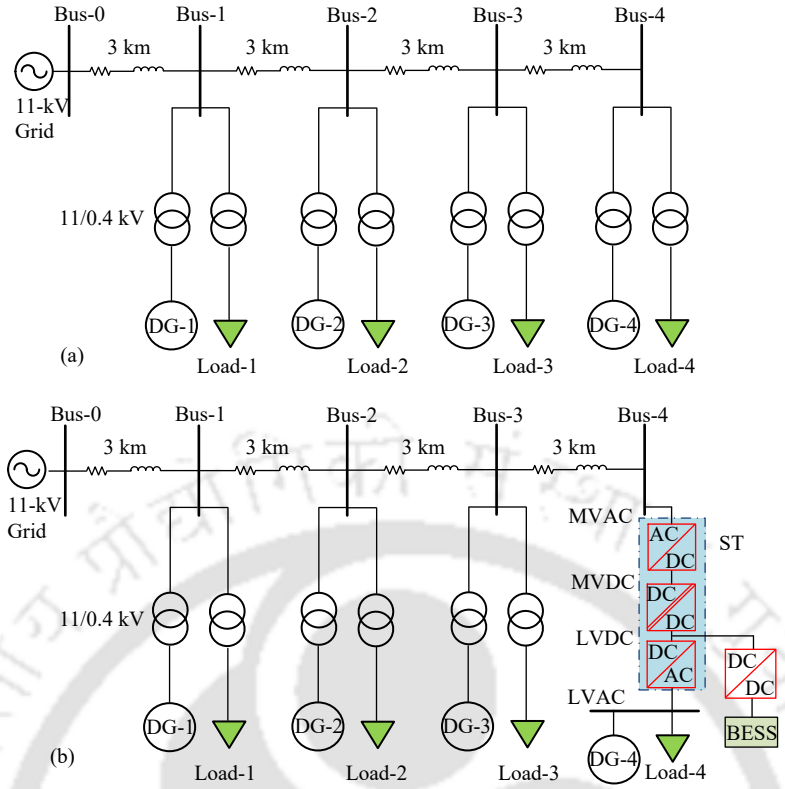

Fig. 3.1 Single-line diagram of a 5-bus radial feeder. (a) Conventional system [114]. (b) Proposed ST based system.

3.1.1 System Configuration

Fig. 3.1(a) shows the single-line diagram of an 11-kV, 5-bus, radial distribution feeder derived from [114]. The R/X ratio of the distribution system is 0.85 [9] with Weasel conductor. Other system parameters are given in Table 3.1. In each bus, loads and DG are connected through 11/0.4 kV CPT. The uniform variation of loads and generation at all buses are considered in this chapter to analyze the extreme voltage drop/rise scenarios [94], [97]. The loads are considered at a power factor of 0.95 lagging, and generation is considered at the unity power factor [94].

Fig. 3.1(b) shows the modified distribution system where the CPTs at bus-4 are replaced with an ST. The ST uses a three-stage configuration, and the details are provided in Chapter 2. The ST LV converter maintains a three-phase balanced sinusoidal voltage at the LVAC terminal. The load (Load-4) and DG (DG-4) are connected to the LVAC bus of ST. The BESS consists of a dc-dc converter, which connects the battery system to the LVDC terminal of ST. All the circuit parameters remain the same as given in Table 3.1.

Table 3.1 System Parameters

System quantities	Values
MVAC grid voltage	11 kV
LVAC voltage	0.4 kV
MVAC line parameters	1.014 + j1.1929 Ω/km
Load power factor	0.95 lag
Base voltage	11 kV
Base power	1 MVA

3.1.2 Sensitivity Analysis

Sensitivity analysis works as a tool to establish simple linear relationship between active, reactive powers and voltage instead of complex network equations [112]. The approximate relationship based on the sensitivity coefficients helps in identifying the effect of active and reactive power changes on the voltage magnitude. Newton-Raphson load-flow is carried out for the system shown in Fig. 3.1(b) to determine the voltages at each bus. Bus-0 is assumed as slack bus, and voltage magnitude is considered as 1 p.u. At bus-4, the ST absorbs only active power from the grid, and no reactive power is exchanged with the MVAC grid. Sensitivity analysis helps in identifying the effect of active and reactive powers on the various bus voltages. In this chapter, the sensitivity coefficients are derived from Jacobian matrix of Newton-Raphson load-flow method. The loading on bus-1 to bus-4 is uniformly increased from zero at the constant power factor, and the corresponding bus voltage magnitudes are plotted in Fig. 3.2. For analyzing the worst loading condition, generation at all the buses is considered as zero. From Fig. 3.2, it is observed that the bus-4 experiences worst voltage variations. Therefore, the objective of this chapter is to improve the voltage at bus-4 and thereby improving the load hosting capability. The change in voltage at bus-4 is related to different active and reactive powers by the relation [112]

$$\Delta|V_{b4}| = \sum_{i=1}^{4} \frac{\partial|V_{b4}|}{\partial P_{bi}} \Delta P_{bi} + \sum_{i=1}^{4} \frac{\partial|V_{b4}|}{\partial Q_{bi}} \Delta Q_{bi}. \tag{3.1}$$

In (3.1), $\Delta|V_{b4}|$ is the change in 4^{th} bus voltage magnitude in p.u. $\frac{\partial|V_{b4}|}{\partial P_{bi}}$ and $\frac{\partial|V_{b4}|}{\partial Q_{bi}}$ are the bus-4 voltage magnitude sensitivities for different bus active and reactive power changes for $i = 1,..,4$. ΔP_{bi} and ΔQ_{bi} are active and reactive power changes in the

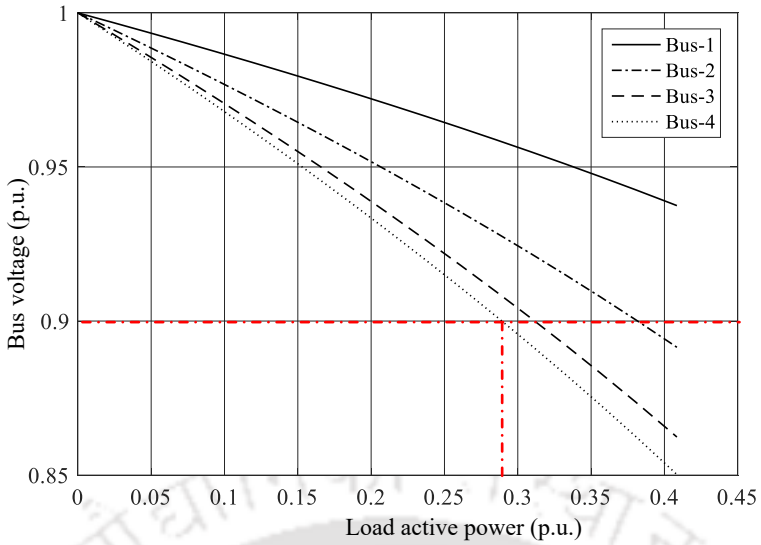

Fig. 3.2 Variation of bus voltage magnitudes with uniform increase in load.

corresponding bus, respectively.

3.2 SIZING BASED ON SENSITIVITY ANALYSIS DURING LOAD INCREASE

This section consists of four sub-sections. In the first part, the system operating conditions based on the load-flow studies are explained, which are the basis for sizing analysis. In the other three sub-sections, the sizing of various converters are explained using sensitivity studies under three different operating scenarios. In the first method, only reactive power injection from ST is considered. In the second method, only active power injection is considered. In the last method, the combination of active and reactive power is utilized to attain the desired hosting capability.

3.2.1 System Operating Conditions

In the proposed method, the ST integrated with BESS is controlled to manage the power flow at the MVAC grid for improving the load hosting capability of the feeder. It can be observed from Fig. 3.2 that the maximum active power loading is limited to approximately 0.29 p.u. due to the violation of voltage limit (0.9 p.u.). The steady-state voltage variations in a distribution system are not allowed beyond a maximum of 1.1 p.u. and a minimum of 0.9 p.u., respectively [103]. Therefore, if the bus-4 voltage is within

these limits, the ST is operated in normal operating mode. If the limits are violated, it is operated in voltage control mode. This chapter considers active and/or reactive power control only at bus-4 using BESS integrated ST. The worst bus voltage magnitude considered for analysis in this chapter is 0.85 p.u. Therefore, the maximum load hosting capability that can be achieved is the load corresponding to 0.85 p.u. of bus-4 voltage. From Fig. 3.2, the voltage at bus-4 is 0.85 p.u. when the active power loading on all the buses are 0.41 p.u. The rating of converters is decided to improve the voltage during this maximum voltage scenario. For the analysis, losses in the converters are neglected.

The ST LV converter supplies the load at the LVAC side in bus-4. In all the considered cases, the maximum active power loading is 0.41 p.u. at a lagging power factor of 0.95. Therefore, the ST LV converter is rated at 0.432 p.u.

3.2.2 ST with Only Reactive Power Support at MVAC Grid

In this case, the ST MV converter supports the grid with reactive power. No active power exchange is scheduled for MVAC grid support and therefore, BESS is not considered in this analysis. The rating requirements for ST DC-DC converter and MV converter are explained as follows.

ST DC-DC converter

The ST DC-DC converter is required to carry the entire active power requirement at the LVAC side. Hence, the rating (P_{dc-rat}) of this converter for satisfactory operation is,

$$P_{dc-rat} = P_{lv-max}. \tag{3.2}$$

The maximum active power loading (P_{lv-max}) at the ST LV converter is 0.41 p.u.; therefore, the DC-DC converter rating is considered as 0.41 p.u.

ST MV converter

The ST MV converter is rated such that it supplies the reactive power required at the MVAC side to maintain the bus-4 steady-state voltage at 0.9 p.u. This converter should

also supply the maximum active power requirement at the LVAC side. P_{mv-rat} is the active power rating of ST MV converter for a maximum LVAC load of P_{lv-max}. Therefore,

$$P_{mv-rat} = P_{lv-max}. \tag{3.3}$$

The ST's reactive power capability is utilized to maintain the required steady-state voltage, and no active power exchange is considered for the grid support. Modifying (3.1) based on these considerations,

$$\Delta|V_{b4}| = \frac{\partial|V_{b4}|}{\partial Q_{b4}}\Delta Q_{b4} \tag{3.4}$$

where $\frac{\partial|V_{b4}|}{\partial Q_{b4}}$ is the sensitivity of bus-4 voltage for its reactive power change in p.u./p.u. The maximum voltage magnitude deviation that needs to be mitigated is $\Delta|V_{b4-max}|$. The reactive power change (ΔQ_{b4-max}) required at MVAC grid is computed as

$$\Delta Q_{b4-max} = \frac{\Delta|V_{b4-max}|}{\frac{\partial|V_{b4-max}|}{\partial Q_{b4-max}}} \tag{3.5}$$

where $\frac{\partial|V_{b4-max}|}{\partial Q_{b4-max}}$ is the voltage sensitivity at the corresponding maximum loading, and ΔQ_{b4-max} is the reactive power required from the ST to maintain the voltage at required value.

The power rating requirements are calculated to improve the voltage to 0.9 p.u. at a maximum active power loading of 0.41 p.u. From the load-flow studies, the sensitivity of reactive power at the maximum active power loading (0.41 p.u.) is found to be 0.1471 p.u./p.u. The maximum voltage deviation that needs to be mitigated is 0.05 p.u. Therefore from (3.5), the reactive power required to mitigate this voltage deviation is,

$$\Delta Q_{b4-max} = \frac{0.05}{0.1471} = 0.34 \quad \text{p.u.} \tag{3.6}$$

From (3.3) and (3.6), the active and reactive power capacity required by the ST MV converter are,

$$P_{mv-rat} = 0.41 \quad \text{p.u.} \quad ; \quad Q_{mv-rat} = 0.34 \quad \text{p.u.} \tag{3.7}$$

From (3.7), the rating of ST MV converter is computed to be 0.53 p.u.

3.2.3 ST with Only Active Power Support at MVAC Grid

In this case, the active power supply from BESS is considered for improving the load hosting capability. The ST MV converter reactive power injection is not considered for the analysis. The rating requirements for BESS converter, ST DC-DC converter and MV converter are explained as follows.

BESS converter

When the bus-4 MVAC voltage limit is violated due to higher loading, active power from BESS is supplied to maintain the voltage magnitude within the steady-state limit. Modifying (3.1) based on these considerations,

$$\Delta|V_{b4}| = \frac{\partial|V_{b4}|}{\partial P_{b4}}\Delta P_{b4} \tag{3.8}$$

where $\frac{\partial|V_{b4}|}{\partial P_{b4}}$ is the sensitivity of bus-4 voltage for its active power change in p.u./p.u. Similar to (3.5), the active power requirement (ΔP_{b4-max}) is computed as follows:

$$\Delta P_{b4-max} = \frac{\Delta|V_{b4-max}|}{\frac{\partial|V_{b4-max}|}{\partial P_{b4-max}}} \tag{3.9}$$

where $\frac{\partial|V_{b4-max}|}{\partial P_{b4-max}}$ is the voltage sensitivity at the corresponding maximum loading. Therefore, the BESS converter rating required to achieve the specified magnitude of voltage is given by ΔP_{b4-max}.

Maximum voltage deviation of 0.05 p.u. is considered, similar to the previous case of analysis. The sensitivity factor corresponding to the maximum loading, $\frac{\partial|V_{b4-max}|}{\partial P_{b4-max}} = 0.1520$ p.u./p.u. Substituting the values in (3.9), the BESS rating is obtained as,

$$\Delta P_{b4-max} = \frac{0.05}{0.1520} = 0.329 \quad \text{p.u.} \tag{3.10}$$

Therefore, the BESS rating of 0.329 p.u. is required at bus-4 to improve the load hosting capability of system from 0.29 p.u. to 0.41 p.u. at all the four buses.

ST DC-DC converter

When steady-state voltage is within the limit, the ST DC-DC converter should maintain the active power flow from MVAC grid. Maximum active power loading considered in this case is 0.29 p.u. Therefore, the rating of the DC-DC converter in this condition is selected as 0.29 p.u.

ST MV converter

The ST MV converter active power requirement is calculated both in normal and voltage control modes of operation. The higher value is selected as the rating of the converter for this case of analysis. When the bus-4 voltage is within the steady-state limit, the ST MV converter supplies the active power requirement at the LVAC side and BESS. The active power requirement is 0.29 p.u. When the bus-4 voltage exceeds the steady-state limit, the ST MV converter active power requirement for a BESS power supply of P_b is

$$P_{mv-rat} = P_{lv-max} - P_b. \tag{3.11}$$

The BESS supplies 0.329 p.u. of active power to improve the steady-state voltage at the bus-4. The active power requirement from ST MV converter is 0.081 p.u. for a maximum load of 0.41 p.u. Since the reactive power injection is not considered in this analysis, the ST MV converter rating requirement is 0.29 p.u.

3.2.4 ST with Both Active and Reactive Power Support at MVAC Grid

In this case, the active power supply from the BESS is utilized along with the reactive power capability of ST MV converter to mitigate the steady-state voltage drop. The rating requirements for BESS converter, ST DC-DC converter and MV converter is explained as follows.

BESS converter

Modifying (3.1) by incorporating bus-4 active and reactive power control

$$\Delta|V_{b4}| = \frac{\partial|V_{b4}|}{\partial P_{b4}}\Delta P_{b4} + \frac{\partial|V_{b4}|}{\partial Q_{b4}}\Delta Q_{b4}. \tag{3.12}$$

In this analysis, as a generalized case, the active and reactive power contributions are considered equal. All other combinations of active and reactive power injections are also possible with the ST. Based on the equal active and reactive power contribution, (3.12) can be modified to,

$$\Delta|V_{b4-max}| = (\frac{\partial|V_{b4-max}|}{\partial P_{b4-max}} + \frac{\partial|V_{b4-max}|}{\partial Q_{b4-max}})\Delta P_{b4-max}. \tag{3.13}$$

Calculating the BESS size with the ST active and reactive power contribution,

$$\Delta P_{b4-max} = \Delta Q_{b4-max} = \frac{0.05}{0.1520 + 0.1471} = 0.167 \quad \text{p.u.} \tag{3.14}$$

The BESS converter size required for achieving improved load hosting capability is reduced to 0.167 p.u. after the incorporation of ST MV reactive power control.

ST DC-DC converter

The rating of ST DC-DC converter remains same as the previous case since during normal operating condition, this converter needs to supply LVAC active power load. Therefore, the rating of DC-DC converter in this condition is selected as 0.29 p.u.

ST MV converter

During the normal operating mode, the ST MV converter supplies the active power requirement at the LVAC side and BESS. The active power requirement is 0.29 p.u. During the voltage control mode, the active power required from the ST MV converter is as per (3.11). The BESS supplies 0.167 p.u. of active power to improve the steady-state voltage at the bus-4. The active power requirement from ST MV converter is 0.243 p.u. for a maximum load of 0.41 p.u. Since the reactive power injection is calculated

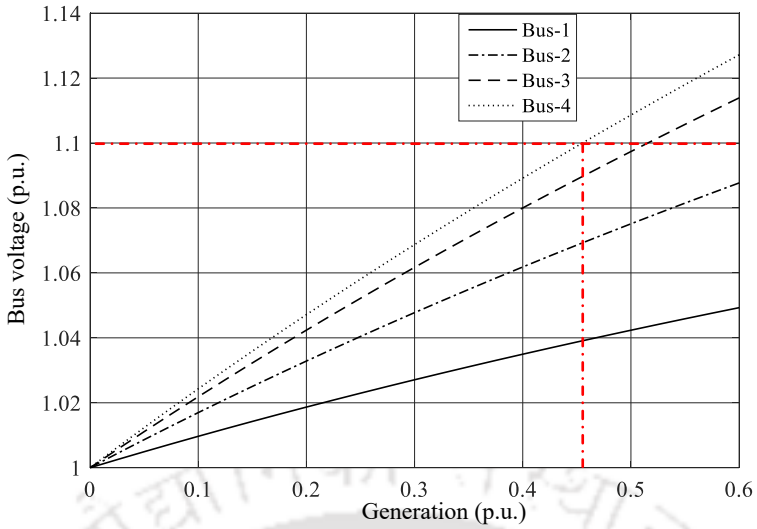

Fig. 3.3 Variation of bus voltage magnitudes with uniform increase in generation.

as 0.167 p.u., in this strategy, the ST MV converter rating requirement is 0.295 p.u. The ratings of different power converters obtained from the above analysis is given in Table 3.2.

3.3 SIZING BASED ON SENSITIVITY ANALYSIS DURING GENERATION INCREASE

In this section, the sizing analysis is explained when the generation is increased along the feeder. Newton-Raphson load-flow is carried out for the system shown in Fig. 3.1(b) to determine the voltages at each bus. Bus-0 is assumed as slack bus, and voltage magnitude is considered as 1 p.u. In this case, the generation at each bus is increased uniformly and the reverse power flow condition is analyzed. Due to reverse power flow along the feeder, the voltages increase at different buses. Fig. 3.3 shows the variation of voltages at different buses when generation is increased from zero. For analyzing the worst voltage rise phenomenon, the loading at all the buses is assumed as zero. From Fig. 3.3, it can be observed that the maximum active power generation is limited approximately to 0.46 p.u. due to the violation of the upper voltage limit (1.1 p.u.). The ST's capability to improve the load hosting capability can also be utilized for increasing DG penetration. The sensitivity study explained in case of load hosting capability improvement is repeated for the generation increase.

As seen in Fig. 3.3, the bus-4 experiences the worst voltage magnitude rise due to

Table 3.2 Comparison of Ratings of Converters with Different Power Control Methods Using ST during Load Increase

Sl. No.	Control		Rating (p.u.)			
	Active power	Reactive power	ST MV converter	ST DC-DC converter	ST LV converter	BESS converter
1	No	Yes	0.53	0.41	0.432	NA
2	Yes	No	0.29	0.29	0.432	0.329
3	Yes	Yes	0.295	0.29	0.432	0.167

increased generation. The worst bus voltage magnitude considered for analysis in this chapter is 1.125 p.u. With this voltage magnitude, the maximum DG hosting capability that can be achieved is the generation corresponding to 1.125 p.u. of bus-4 voltage. From Fig. 3.3, the voltage at bus-4 is 1.125 p.u. when the active power generation on all the buses is 0.59 p.u. This condition is considered to decide the size of different converters. The sensitivity-based sizing is explained for the load increase case, and the same methods are repeated for generation increase. The findings related to the ratings of different converters are given in Table 3.3.

The third scenario shown in the earlier analysis considers the equal contribution of active and reactive power injection. However, the ST is capable of operating at other combinations of active and reactive powers to improve the voltage at bus-4. This flexible active, reactive power injection shows the multiple power factor operation capability of ST for achieving the same objective.

This method cannot be extended for any voltage and load conditions due to the limitation on the convergence of N-R load flow method. Moreover, the operation at or near the P-V curve nose point is impractical and a sufficient power margin need to be provided for the satisfactory operation of the system [115]. Therefore, the proposed method is not applicable for the operation at or near the nose point of the P-V curve.

3.4 CONTROL OF POWER CONVERTERS

In this section, the principle of operation and control of ST MV converter, ST DC-DC converter, ST LV converter and BESS converter is explained. Fig. 3.4 shows the overall control diagram of ST. The ST MV converter is controlled in current control mode. The ST DC-DC converter maintains the LVDC link voltage constant at the reference value (V^*_{lv-dc}). The ST LV converter is controlled to maintain a constant three-phase balanced voltage based on the reference voltage V^*_{lv}. The BESS exchanges the active power with the LVDC link of ST based on the power reference P^*_b. The control of converters are explained for load increase case.

Table 3.3 Comparison of Ratings of Converters with Different Power Control Methods Using ST during Generation Increase

Sl. No.	Control		Rating (p.u.)			
	Active power	Reactive power	ST MV converter	ST DC-DC converter	ST LV converter	BESS converter
1	No	Yes	0.635	0.59	0.59	NA
2	Yes	No	0.46	0.46	0.59	0.349
3	Yes	Yes	0.47	0.46	0.59	0.14

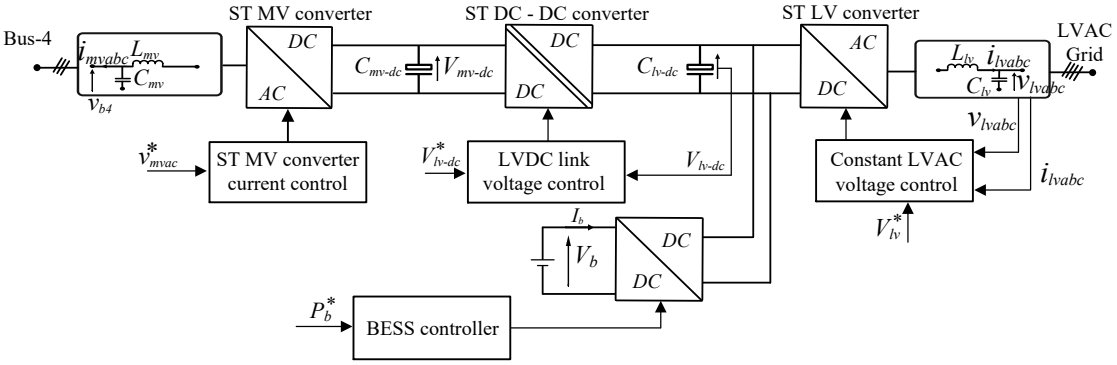

Fig. 3.4 Overall control diagram of ST and BESS.

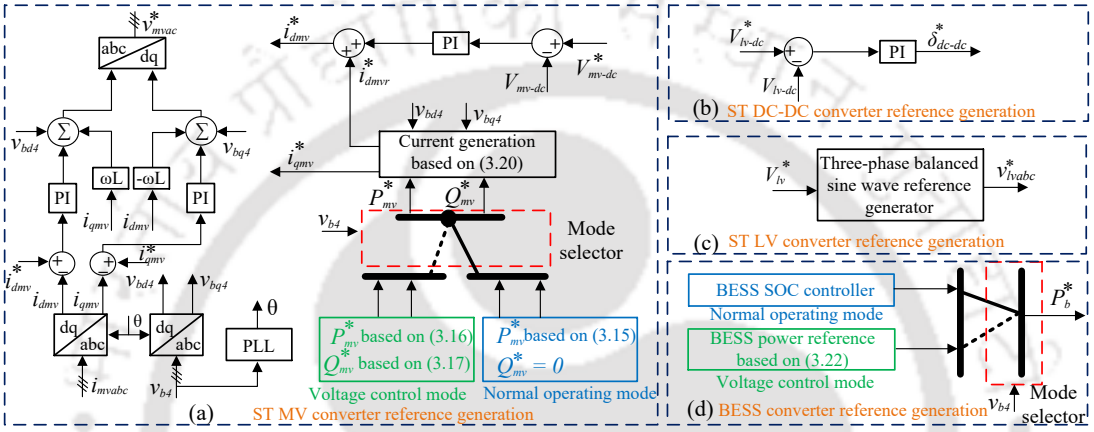

Fig. 3.5 (a) ST MV converter reference generation strategy. (b) ST DC-DC converter reference phase angle generation strategy. (c) ST LV converter reference generation strategy. (d) BESS converter reference generation strategy.

3.4.1 ST MV Converter Control

The control of ST MV converter is explained during normal and voltage control modes. The control block-diagram is shown in Fig. 3.5(a). During the normal operating condition, the ST MV converter supplies the active power requirement at the LVAC side and BESS charging power requirement. The ST MV converter active power requirement is given by

$$P^*_{mv} = P_{b4l} + P^*_b \tag{3.15}$$

where P_{b4l} is the active power loading at the ST LVAC side and P^*_b is the BESS charging power reference. No exchange of reactive power is considered at this condition, and the reactive power reference (Q^*_{mv}) is zero. Therefore, the ST operates at unity power factor during normal operating condition.

In the voltage control mode, depending upon the strategy adopted for capacity enhancement, active and/or reactive power references are generated for ST MV converter. The

load increase leads to voltage drop in different buses. For a specified lower limit of voltage magnitude V_{b4-ll}, and bus-4 voltage magnitude of V_{b4}, the ST MV active power reference is given by

$$P^*_{mv} = P_{b4l} + M_{pd}(V_{b4} - V_{b4-ll}) \tag{3.16}$$

where M_{pd} is the slope factor for active power (p.u./p.u.). The ST MV converter reactive power reference is given by

$$Q^*_{mv} = 0 + M_{qd}(V_{b4} - V_{b4-ll}) \tag{3.17}$$

where M_{qd} is the slope factor for reactive power (p.u./p.u.).

Depending upon the strategy adopted for voltage control, active/reactive power independently or a combination of both is utilized. The value of slope factor depends on the strategy adopted for capacity enhancement. The calculation of slope factors for a simultaneous active and reactive power injection strategy is explained as follows. The BESS capacity required for the voltage drop of 0.05 p.u. beyond the lower limit is calculated in (3.14) and maximum BESS power required for the mitigation of this voltage drop is 0.167 p.u. Therefore, the BESS power required for a 1 p.u. voltage change, M_{pd} is given by

$$M_{pd} = \frac{\Delta P_{b4-max}}{\Delta |V_{b4-max}|} = \frac{1}{\left(\frac{\partial |V_{b4-max}|}{\partial P_{b4-max}} + \frac{\partial |V_{b4-max}|}{\partial Q_{b4-max}}\right)} = \frac{0.167}{0.05} = 3.34 \quad \text{p.u/p.u.} \tag{3.18}$$

As considered in (3.13), the active and reactive power contribution from ST are equal. Therefore, the reactive power slope factor is given by

$$M_{qd} = 3.34 \quad \text{p.u/p.u.} \tag{3.19}$$

Similarly, the slope factors for only active or reactive power injection strategy can be computed. The active and the reactive power references are generated using the above-mentioned strategies. These are used as inputs to the inner controllers, explained in the next part of this section.

Three-phase bus-4 voltages (v_{b4}) and ST MV converter currents (i_{mvabc}) are converted to its d and q components v_{bd4}, v_{bq4} and i_{dmv}, i_{qmv}, respectively. The outer controller generates the active (P^*_{mv}) and the reactive (Q^*_{mv}) power references based on different

control modes as given in (3.15), (3.16), and (3.17) . The MVDC link voltage (V_{mv-dc}) is compared with a reference value (V^*_{mv-dc}) and the error is passed through a PI controller to generate the d component of current which corresponds to the losses in DC link. The current references are generated from the power references using the following equation:

$$\begin{bmatrix} i^*_{dmvr} \\ i^*_{qmv} \end{bmatrix} = \frac{2}{3}\frac{1}{v^2_{bd4}+v^2_{bq4}} \begin{bmatrix} v_{bd4} & -v_{bq4} \\ v_{bq4} & v_{bd4} \end{bmatrix} \begin{bmatrix} P^*_{mv} \\ Q^*_{mv} \end{bmatrix}. \tag{3.20}$$

The d component of current reference (i^*_{dmvr}) is added with the loss component to generate total current reference i^*_{dmv}. The q component of reference current (i^*_{qmv}) is generated directly from (3.20). The three-phase voltage references (v^*_{mvac}) for the ST MV converter are generated from the current reference given in (3.20), and i^*_{dmv} using voltage oriented current control as shown in Fig. 3.5(a) [70].

3.4.2 ST DC-DC Converter Control

The primary function of this converter is to maintain the LVDC voltage at a constant value. It ensures a constant power flow between MVDC and LVDC links of ST. The block-diagram representation is shown in Fig. 3.5(b). The LVDC voltage (V_{lv-dc}) is compared with a reference value (V^*_{lv-dc}) and the error is passed through a PI controller to generate the phase angle which is maintained between MVDC and LVDC side converter switching instances [59]. Moreover, Chapter 2 provides a detailed explanation for this converter operation and control.

3.4.3 ST LV Converter Control

The ST LV converter is controlled as a grid forming voltage source converter. Fig. 3.5(c) shows the reference generation block-diagram. The converter maintains the reference value of rms phase voltage (V^*_{lv}) at 50 Hz frequency and 120° phase difference between phases to generate three-phase balanced sinusoidal voltage at the LVAC side [9], [96]. The detailed explanation for this converter operation is provided in Chapter 2.

Table 3.4 Simulation Parameters

System quantities	Values
ST MV converter	L_{mv} = 20 mH, C_{mv} = 5 μF
ST LV converter	L_{lv} = 0.5 mH, C_{lv} = 20 μF
DC link voltage	V_{mv-dc} = 20 kV, V_{lv-dc} = 0.7 kV
DC link capacitor	C_{mv-dc} = 2000 μF, C_{lv-dc} = 2500 μF
ST DC-DC converter	L_{mvdc} = 10 mH, f_{sw} = 1 kHz
BESS DC-DC converter	L_b = 50 μH, f_{sw} = 10 kHz

3.4.4 BESS DC-DC Converter Control

In Fig. 3.5(d), the method to compute reference power (P_b^*) for BESS converter is shown. During the normal grid operating conditions, the active power exchange with the MVAC grid maintains the appropriate SOC. The BESS current reference (I_b^*) is given by

$$I_b^* = \frac{P_b^*}{V_b} \tag{3.21}$$

where V_b is the voltage across the battery.

During voltage control mode, depending upon the adopted support strategy, the BESS may be activated. The BESS supplies the active power based on

$$P_b^* = M_{pd}(V_{b4} - V_{b4-ll}). \tag{3.22}$$

Using P_b^*, the current I_b^* is computed from (3.21). It is compared with the actual current (I_b) and passed through a PI controller to generate the error. This is used to generate switching pulses for the DC-DC converter [107].

3.5 SIMULATION RESULTS

The simulation is carried out in the PSCAD/EMTDC software. The system parameters used for simulation studies are given in Table 3.1, 3.4, and 3.5. Loading on all the four buses are considered to be uniform throughout the simulation at a constant lagging power factor of 0.95. The ST is installed at the bus-4, and the active power load hosting capability of each bus is limited to 0.29 p.u. This is due to the violation of steady-state

Table 3.5 Simulation PI Controller Parameters

System	PI Gains
ST MV converter (d-axis)	$K_p = 60$, $K_i = 2 * 10^{-4}$
ST MV converter (q-axis)	$K_p = 60$, $K_i = 2 * 10^{-4}$
MVDC link controller	$K_p = 5$, $K_i = 2 * 10^{-5}$
ST DC-DC converter	$K_p = 5$, $K_i = 1000$
BESS converter	$K_p = 30$, $K_i = 1$

voltage limit (0.9 p.u.) at bus-4. The aim is to improve the active power load hosting capability to 0.41 p.u., which corresponds to 0.85 p.u. of voltage at bus-4 without any active/reactive power support from ST. The active/reactive power requirement from ST in different control strategies is explained in the sizing analysis, and the simulation results verify the theoretical findings.

3.5.1 Performance of System with Only Reactive Power Support from ST

This case analyzes the performance of the system when ST MV converter injects only reactive power to the MVAC grid when load increases beyond 0.29 p.u. Fig. 3.6 shows the simulation results for this case. Till t = 10 s, the active power loading in all the buses are 0.29 p.u. Fig. 3.6(a) shows the bus-4 voltages, and the voltage magnitude is at the steady-state limit of 0.9 p.u. The ST MV converter absorbs the active power requirement at the LVAC side from MVAC grid. Fig. 3.6(b) shows the ST MV converter currents. The ST LV converter maintains a 1 p.u. of voltage at the LVAC side, as shown in Fig. 3.6(c). The ST LV converter supplies the power to LVAC loads, and the currents are shown in Fig. 3.6(d). Fig. 3.6(e) shows the load active and reactive powers. Fig. 3.6(f) shows ST MV converter active, reactive powers, and BESS power. At t = 10 s, the load at all buses is increased to 0.41 p.u. The ST injects reactive power to the MVAC grid and the voltage at the bus-4 is maintained at 0.9 p.u. as shown in the Fig. 3.6(a). Fig. 3.6(e) shows the active and reactive power increase at the bus-4. In Fig. 3.6(f), the reactive power increases after the load change to maintain the voltage at 0.9 p.u. The ST MVAC active power also increases to supply the additional load at the LVAC side. The BESS is not involved in this case of analysis, and its power output remains zero.

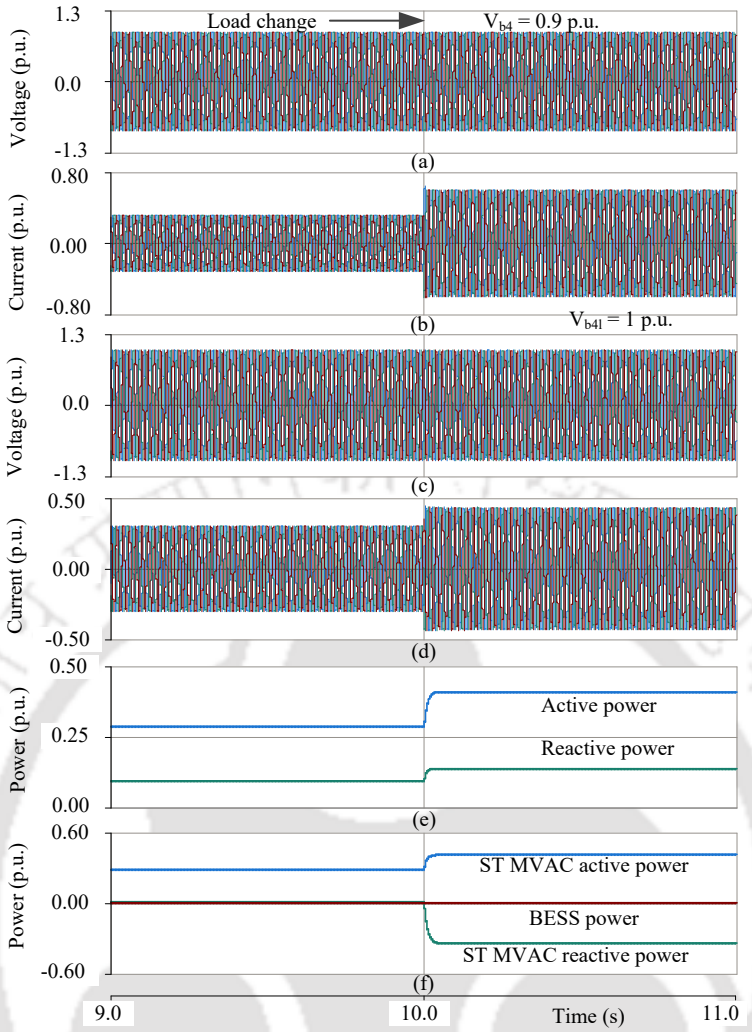

Fig. 3.6 ST supports MVAC grid with reactive power during load change. (a) Bus-4 MVAC voltages. (b) ST MV converter currents. (c) Bus-4 LVAC voltages. (d) LVAC load currents. (e) Bus-4 load active and reactive powers. (f) Different powers.

3.5.2 Performance of System with Only Active Power Support from ST

This case analyzes the performance of the system when ST utilizes active power from BESS to the MVAC grid when the load increases beyond 0.29 p.u. Fig. 3.7 shows the simulation results for this case. The loading in all the buses increases at t = 10 s. Fig. 3.7(a) shows the bus-4 voltages, and the magnitude is at the steady-state limit of 0.9 p.u. Fig. 3.7(b) shows the ST MV converter currents. Fig. 3.7(c) and Fig. 3.7(d) show ST LVAC voltages and currents, respectively. Fig. 3.7(e) shows the load active and reactive powers, and the load increase is visible after t = 10 s. Fig. 3.7(f) shows ST MV converter active and reactive powers, and BESS power. At t = 10 s, the load at all the buses is increased to 0.41 p.u. After the load increase, the BESS injects active power to

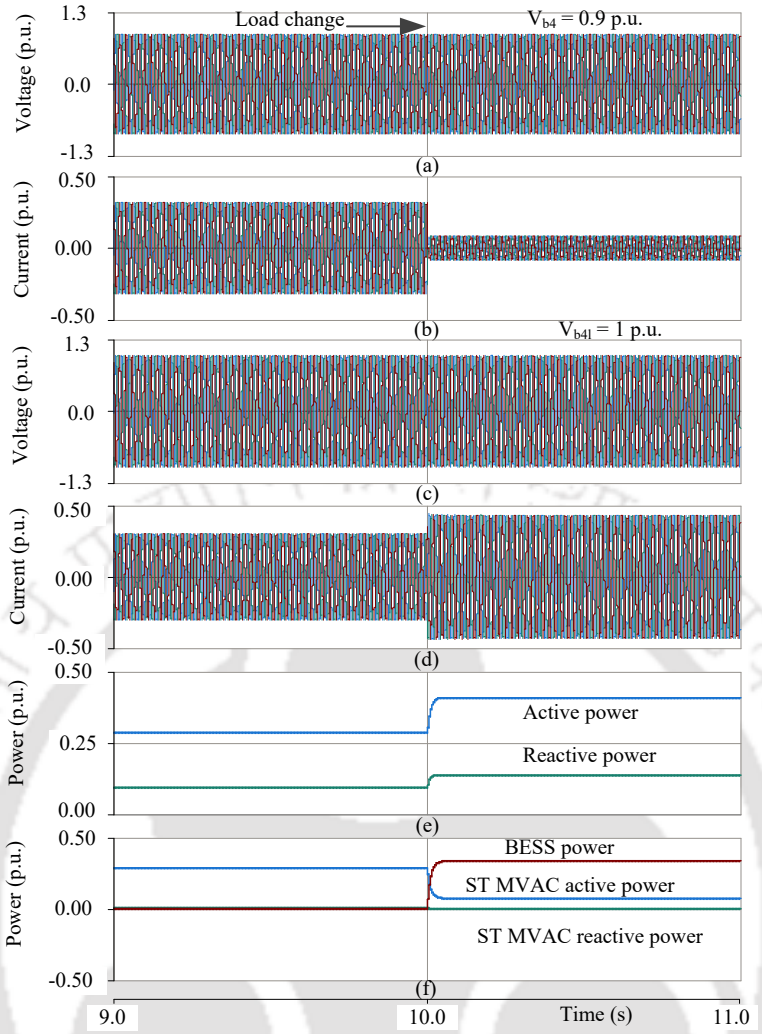

Fig. 3.7 ST supports MVAC grid with active power during load change. (a) Bus-4 MVAC voltages. (b) ST MV converter currents. (c) Bus-4 LVAC voltages. (d) LVAC load currents. (e) Bus-4 load active and reactive powers. (f) Different powers.

the MVAC grid, and the voltage at the bus-4 are maintained at 0.9 p.u. as shown in the Fig. 3.7(a). In Fig. 3.7(f), the active power injection from BESS is visible, and active power absorption from ST MV converter decreases due to BESS injection. ST reactive power is not involved in this case of analysis.

3.5.3 Performance of System with Both Active and Reactive Power Support from ST

This case analyzes the performance of the system when ST utilizes active power from the BESS and reactive power capability of the ST MV converter to improve the load hosting capability. The simulation results are shown in Fig. 3.8 and Fig. 3.9.

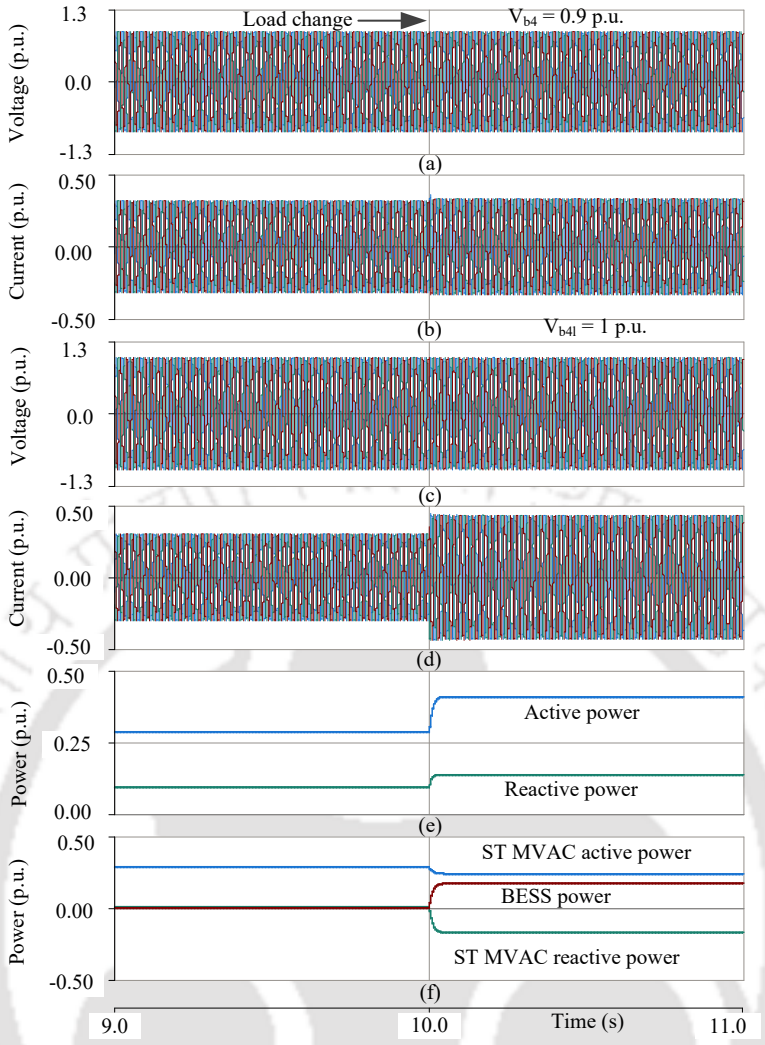

Fig. 3.8 ST supports MVAC grid with equal contribution of active and reactive power during load change. (a) Bus-4 MVAC voltages. (b) ST MV converter currents. (c) Bus-4 LVAC voltages. (d) LVAC load currents. (e) Bus-4 load active and reactive powers. (f) Different powers.

Fig. 3.8 shows the results when the active and reactive power contributions are considered equal. The load increases similar to the previous cases. Fig. 3.8(a) shows the bus-4 voltages and the magnitude is at the steady-state limit of 0.9 p.u. Fig. 3.8(b) shows the ST MV converter currents. The ST LVAC voltages and currents are shown in Fig. 3.8(c) and Fig. 3.8(d), respectively. Load increases after t = 10 s and Fig. 3.8(e) shows the load active and reactive powers. The ST MV converter active and reactive powers, and BESS power are shown in Fig. 3.8(f). The active and reactive power required to maintain the steady-state voltage at 0.9 p.u. is calculated from the sensitivity study, and the same is shown in Fig. 3.8(f).

In another case shown in Fig. 3.9, an unequal contribution of active and reactive power is studied. The reactive power contribution is considered as two times that of active

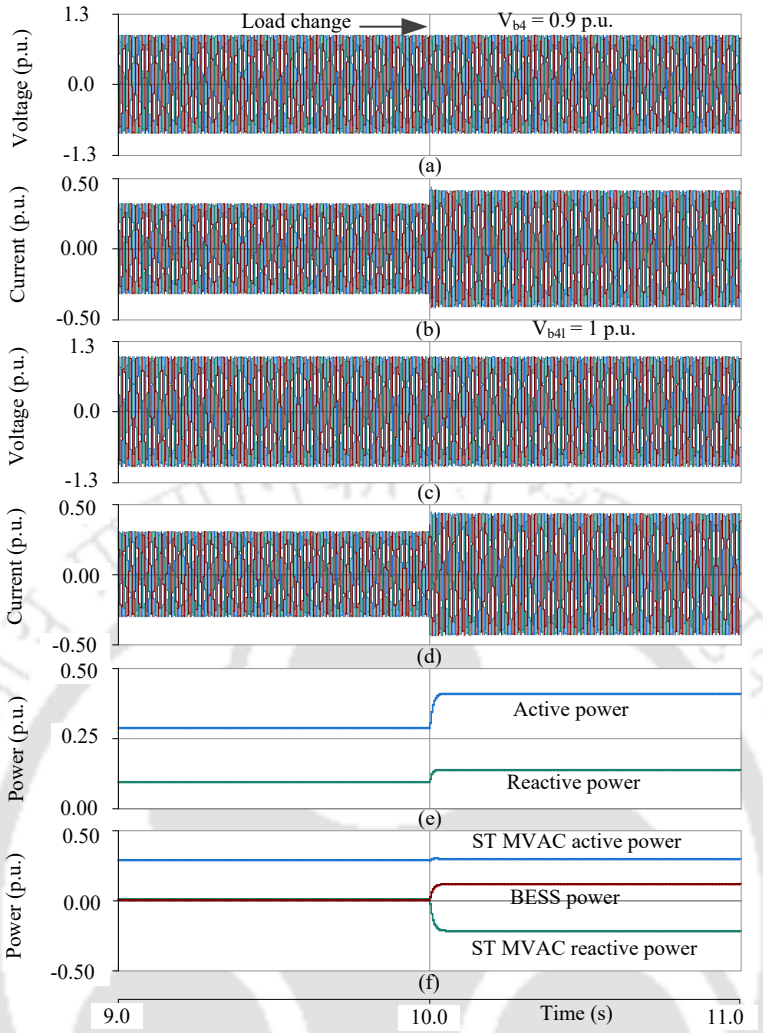

Fig. 3.9 ST supports MVAC grid with unequal contribution of active and reactive power during load change. (a) Bus-4 MVAC voltages. (b) ST MV converter currents. (c) Bus-4 LVAC voltages. (d) LVAC load currents. (e) Bus-4 load active and reactive powers. (f) Different powers.

power to obtain the required voltage support at the bus-4. All other conditions remain same. Fig. 3.9(a) and Fig. 3.9(b) show the bus-4 voltages and ST MV converter currents, respectively. The voltage magnitude remains the same at the steady-state limit of 0.9 p.u. after the load change at t = 10 s. The ST LVAC voltages and currents are shown in Fig. 3.9(c) and Fig. 3.9(d), respectively. Fig. 3.9(e) shows the load active and reactive powers. The ST MV converter active and reactive powers, and BESS power are shown in Fig. 3.9(f). The active and reactive power required to maintain the steady-state voltage at 0.9 p.u. is calculated from the sensitivity study maintaining the ratio of their contribution.

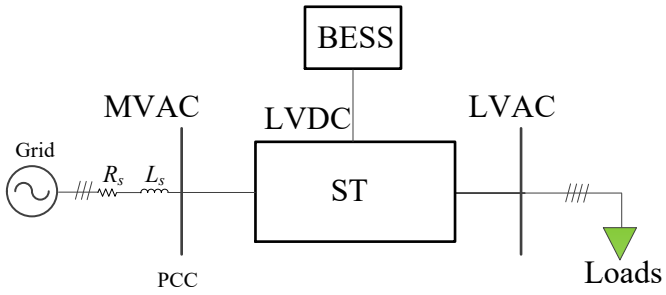

Fig. 3.10 Experimental setup schematic.

Table 3.6 Experimental Parameters

System quantities	Values
MVAC grid voltage	150 V
LVAC grid voltage	110 V
MVAC line parameters	R_s = 2.1 Ω, L_s = 8 mH
ST MV converter	L_{mv} = 18 mH, C_{mv} = 10 μF
ST LV converter	L_{lv} = 5 mH, C_{lv} = 10 μF
DC link voltage	V_{dc} = 270 V
BESS converter	L_b = 18 mH

3.6 EXPERIMENTAL RESULTS

Fig. 3.10 shows the experimental setup configuration. The system shown in Fig. 3.1(b) is simplified to the Fig. 3.10 configuration. The experimental parameters are given in Table 3.6. The equivalent line resistances and inductances till bus-4 are replaced by a lumped value, and the bus-4 is considered as PCC. The R/X ratio of the original 5-bus system is maintained for the experimental analysis also. The system is operating at the load corresponds to 90% of the nominal voltage at PCC. The load is increased to a value which leads the voltage to decrease to 85% of the nominal value without any control. Three cases are investigated in this chapter. In all the three cases, the ST is controlled to improve the voltage at PCC to the maximum allowed limit, i.e., 90% of the nominal value.

3.6.1 Performance of System with Only Reactive Power Support from ST

In this case, the voltage reduction due to load increase is compensated with the reactive power capability of ST MV converter. The experimental waveforms are shown in Fig. 3.11. Fig. 3.11(a) shows the MVAC PCC voltages, which is maintained at the grid-code specified limiting value. The load change is marked in the waveform. Fig. 3.11(b) shows the ST MV converter currents, and it increases after load change due to increased active and reactive power exchange. Fig. 3.11(c) shows the ST LVAC voltages which are maintained at the nominal value. The load increase is visible from the increase in LVAC side currents, as shown in Fig. 3.11(d). The LVDC link voltage is shown in Fig. 3.11(e), which remains constant. The MVAC grid side active power is shown in Fig. 3.11(f). The ST absorbs more power from MVAC grid to supply the increased loads. Fig. 3.11(g) shows the reactive power supplied by the ST MV converter to MVAC grid for maintaining the voltage. Fig. 3.11(h) shows the BESS power, which is maintained at zero in this case of experiment, as only reactive power is used in this case for the capacity enhancement.

3.6.2 Performance of System with Only Active Power Support from ST

In the second case, the active power supply from BESS is used to compensate for the voltage reduction due to increased load requirement, and the waveforms are shown in Fig. 3.12. Fig. 3.12(a)-(e) show the waveforms of MVAC PCC voltages, ST MVAC currents, ST LVAC voltages, ST LVAC load currents, and LVDC link voltage, respectively. The PCC voltages are maintained at the limiting value, even after the load increase as shown in Fig. 3.12(a). The ST MV converter currents remain constant since the increased load is supplied from BESS as shown in Fig. 3.12(b). The LVAC voltage remains at the nominal value as seen in Fig. 3.12(c). The LVAC load change is visible in the Fig. 3.12(d). The DC link voltage remains undisturbed throughout the operation as seen in Fig. 3.12(e). The load increase is compensated with the BESS active power. Fig. 3.12(f) shows the ST MVAC active power, which remains at the previous value after load increase. No reactive power is exchanged with the MVAC grid. This is shown

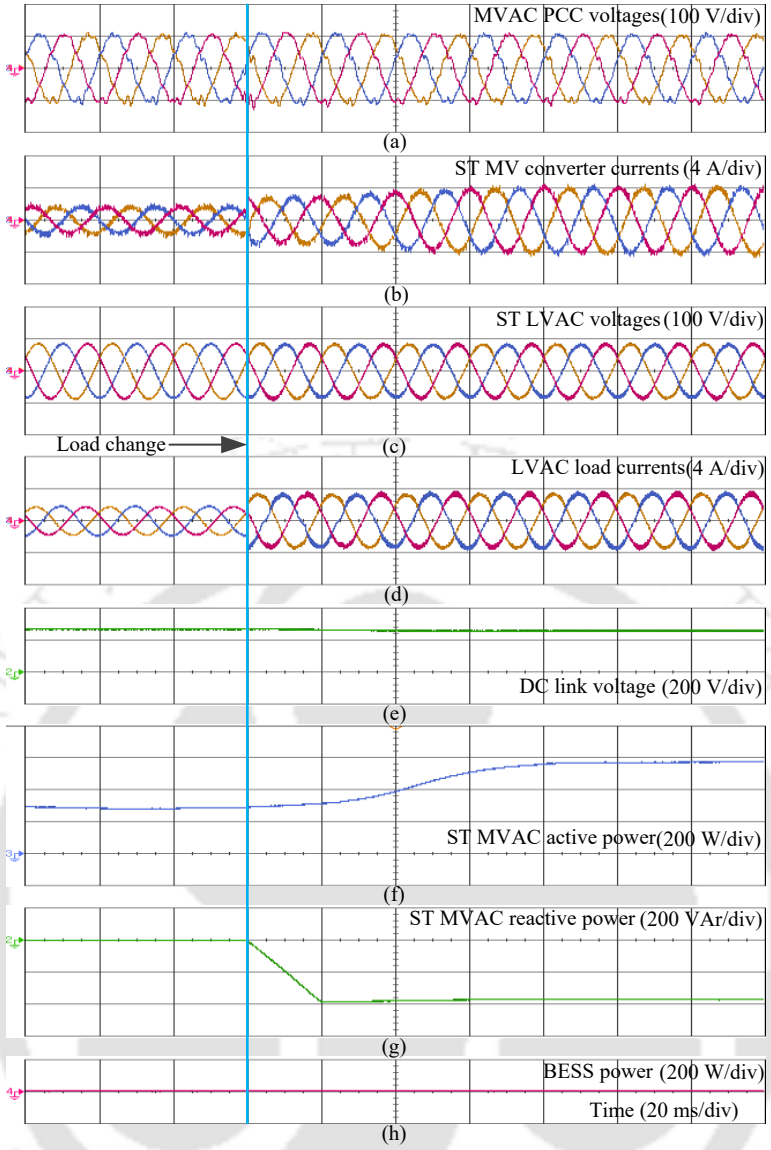

Fig. 3.11 Experimental results when ST supports the grid with reactive power during load change. (a) MVAC PCC voltages. (b) ST MV converter currents. (c) ST LVAC voltages. (d) LVAC load currents. (e) DC link voltage. (f) ST MVAC active power. (g) ST MVAC reactive power. (h) BESS power.

in Fig. 3.12(g). Fig. 3.12(h) shows the BESS power, which is required to maintain the voltage at MVAC grid.

3.6.3 Performance of System with Both Active and Reactive Power Support from ST

In the third case, simultaneous active and reactive powers from ST are used to compensate for the voltage reduction due to increased load requirement, and the waveforms are shown in Fig. 3.13. Fig. 3.13(a)-(e) show the waveforms of MVAC PCC voltages,

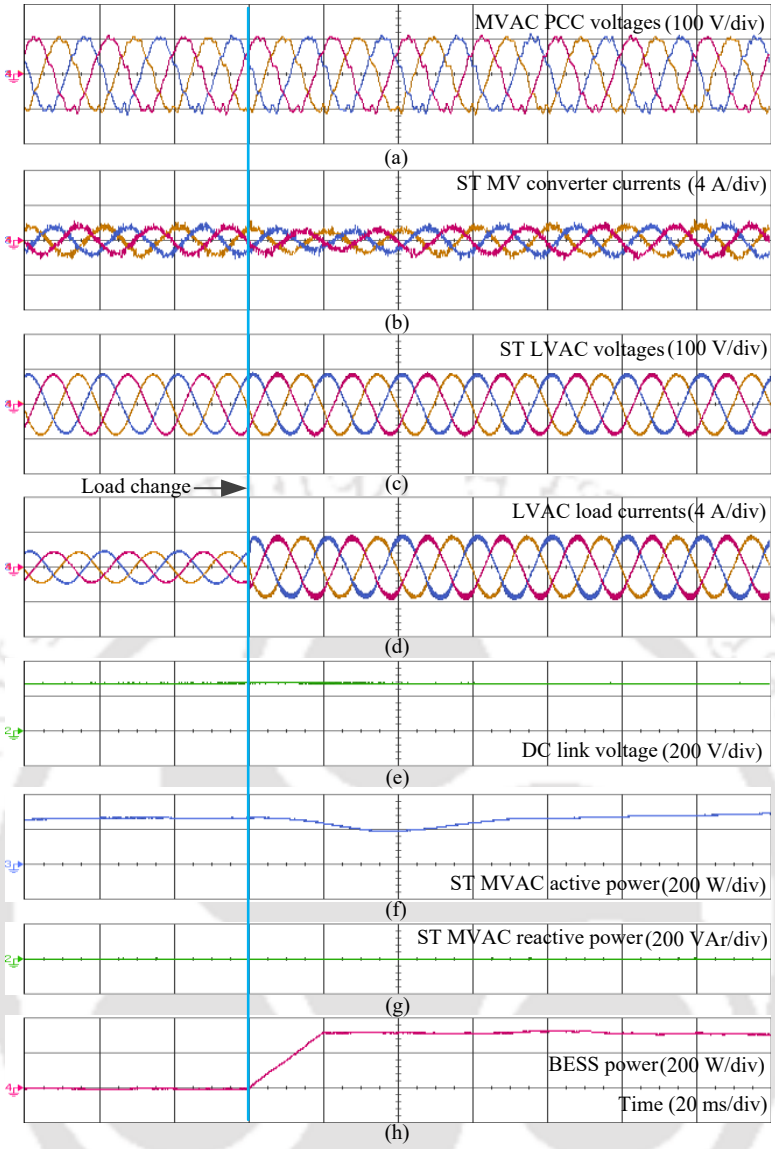

Fig. 3.12 Experimental results when ST supports the grid with active power during load change. (a) MVAC PCC voltages. (b) ST MV converter currents. (c) ST LVAC voltages. (d) LVAC load currents. (e) DC link voltage. (f) ST MVAC active power. (g) ST MVAC reactive power. (h) BESS power.

ST MVAC currents, ST LVAC voltages, ST LVAC load currents, and LVDC link voltage, respectively. The PCC voltages are maintained at the limiting value, even after the load increase as shown in Fig. 3.13(a). The ST MV converter currents increases due to the exchange of active and reactive powers as shown in Fig. 3.13(b). The LVAC voltage remains at the nominal value as seen in Fig. 3.13(c). The LVAC load increase is visible in the Fig. 3.13(d). The DC link voltage remains undisturbed throughout the operation as seen in Fig. 3.13(e). Fig. 3.13(f) shows the ST MVAC active power. The ST MVAC converter active power increases to supply the required amount of load. As discussed in the sizing analysis, active and reactive power contribution are considered

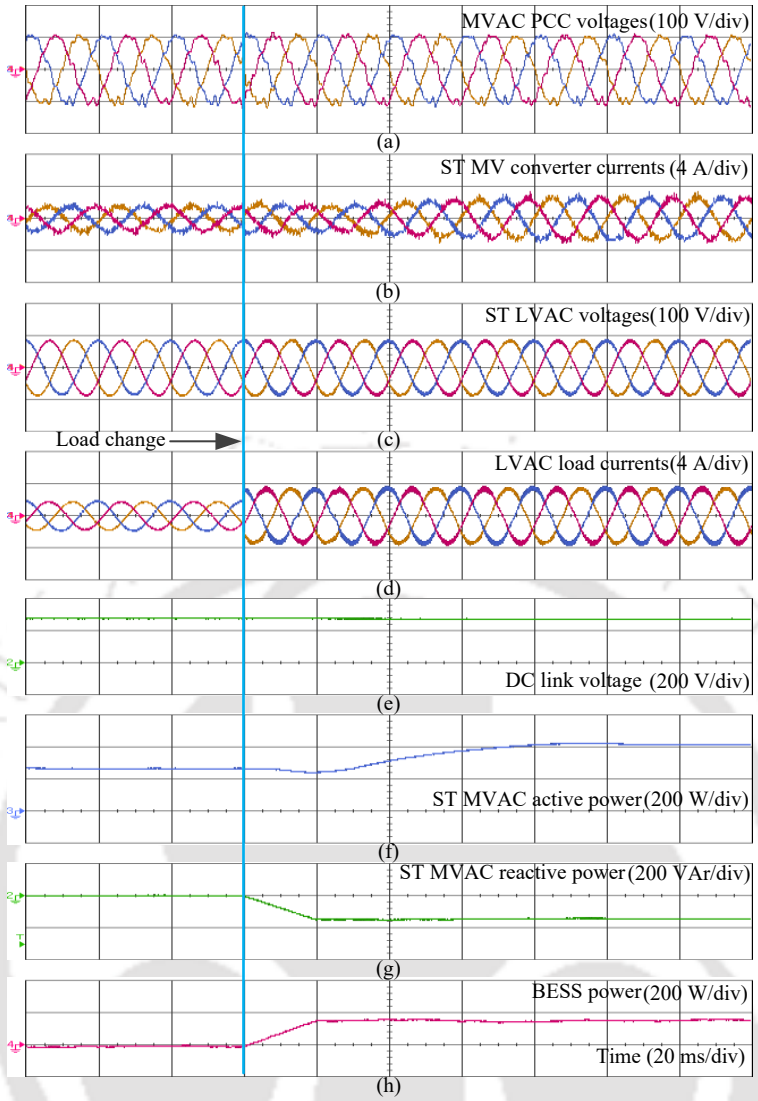

Fig. 3.13 Experimental results when ST supports the grid with active and reactive powers during load change. (a) MVAC PCC voltages. (b) ST MV converter currents. (c) ST LVAC voltages. (d) LVAC load currents. (e) DC link voltage. (f) ST MVAC active power. (g) ST MVAC reactive power. (h) BESS power.

equal, and ST MVAC reactive and BESS powers are shown in Fig. 3.13(g) and Fig. 3.13(h), respectively.

3.7 CONCLUSIONS

In this chapter, the CPT is replaced with a BESS integrated ST in a 5-bus radial MVAC distribution system. The load and generation hosting capability improvement is achieved with three methods utilizing the ST's multidimensional active and reactive power management capability. The design study based on the sensitivity analysis provides the rating requirement for achieving the desired results. The findings are verified through

simulation and experimental results. The flexibility in achieving the required result with the help of active power, reactive power and a combination of active and reactive powers makes the BESS integrated ST a suitable candidate irrespective of the R/X ratio of the MVAC grid.

CHAPTER 4

AN MVDC BASED MESHED HYBRID MICROGRID ENABLED USING SMART TRANSFORMERS

In previous chapters, the ST's capability to control the MVAC grid voltage has been investigated. The Chapter 2 proposes a coordinated voltage improvement strategy for ST in the MVAC grid. Chapter 3 extends to analyze the active and reactive power exchange feature of BESS integrated ST in a 5-bus radial distribution feeder. The load and generation hosting capability improvement is achieved from the proposed strategy utilizing the active power, reactive power and a flexible combination of both. These two chapters focus on the ST's active and reactive power exchange features for the support of voltage in MVAC grid. In addition to the voltage support aspects, the power management capability of ST is an important feature that helps in improving the reliability of distribution grid. Moreover, the incorporation of suitable control of active power plays a crucial role in voltage variations caused by the load and generation fluctuations. This chapter aims to study the power management aspects of ST in an AC microgrid.

The local consumption of the energy generated from the DG sources are more economical and it leads to the formation of microgrids [19], [116]. Even though microgrids can exist independent of AC main grid connection, the interconnection with existing AC grids improves the power quality and reliability of microgrids. In the modern power transmission sector, VSC based HVDC transmission systems are popular for the interconnection of DG sources located away from the main grid [117]. The features such as increased power transfer capability and flexibility in controlling active, reactive power exchanges make this system a better solution in comparison with a conventional AC system [118]. Similarly, in the distribution side, the MVDC distribution systems are considered to be an emerging trend for integrating the AC microgrids with the main grid [95], [119], [120]. Some of the features that MVDC distribution system offers are: independent control of active and reactive power flows, improved stability for existing AC distribution system, decoupling grids with different frequencies, etc. [95], [119]. The conventional AC microgrid faces challenges in flexibly controlling the active power

flow based on the DG output and load condition. Connecting a BTB converter system in a conventional AC distribution line improves the active power control features in the system. In [121], a BTB converter is connected in an MVAC radial feeder and the performance is analyzed during severe voltage sags. Moreover, the reliability of power supply is affected in the conventional configurations. The usage of DC links for establishing highly reliable meshed distribution grids is investigated in [122].

The meshed hybrid microgrids are considered to be an emerging trend in the reconfiguration of microgrids. The MVDC distribution system is effectively utilized for the formation of highly reliable meshed grids [120]. Similarly, the availability of MVDC link of ST opens up an option to realize the MVDC distribution system [64], [65]. The following observations are consolidated from the literature mentioned:

- The power management aspects in microgrids are important to handle the voltage variation due to load and generation fluctuation
- The interconnection of AC microgrids with the other grids improves the reliability of microgrid
- The interconnections through power electronic-based solutions improve the controllability of active and reactive powers
- The MVDC systems offers a flexible solution to the grid interconnection problem [95], [119], [120]
- The ST MVDC link has the potential to establish the MVDC distribution system [64], [65].

This chapter proposes an MVDC based meshed hybrid microgrid using STs. The different power management characteristics of the proposed system is studied and features are compared with the existing solutions. Performance of the system is verified with simulation and experimental studies.

4.1 SYSTEM CONFIGURATION

Fig. 4.1(a) shows a conventional AC microgrid configuration derived from [114], [120]. The 11-kV source in the microgrid is constituted by a number of renewable sources. The 11-kV bus of the microgrid is horizontally coupled to a main grid bus through AC distribution line and normally open (NO) circuit breakers (CBs). In the microgrid MVAC bus, the DG unit (DG-1) and loads (Load-1) are connected through 11/0.4 kV

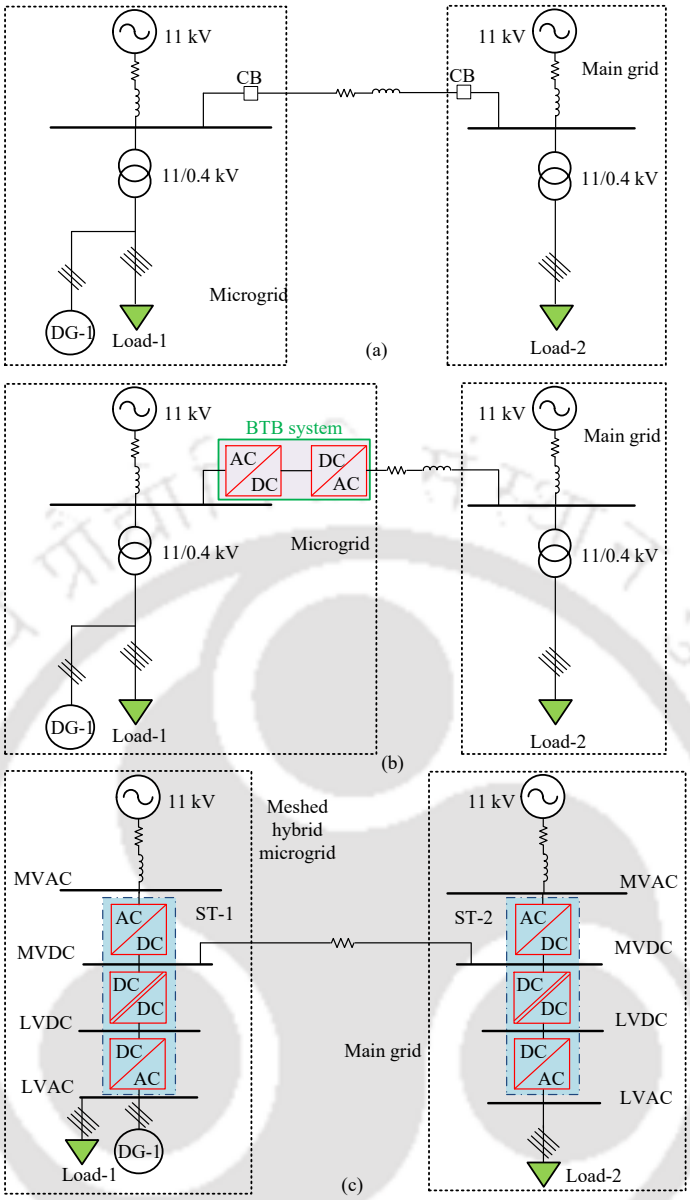

Fig. 4.1 Single-line diagram of the system. (a) A conventional microgrid configuration horizontally coupled with the main grid [114], [120]. (b) A BTB system interconnected microgrid [121]. (c) Proposed MVDC interconnected meshed hybrid microgrid.

CPT. In the main grid MVAC bus, the loads (Load-2) are connected through a 11/0.4 kV CPT.

Fig. 4.1(b) shows a modified conventional AC microgrid configuration derived from [121]. The BTB converter system connects the microgrid with main grid. The controlled active power flow is possible through the BTB system between microgrid and main grid. The connection of loads and DG remains same as the system shown in Fig. 4.1(a).

Fig. 4.1(c) shows the proposed meshed hybrid microgrid using STs. In the microgrid,

Table 4.1 System Parameters

System quantities	Values
MVAC grid voltage	11 kV
LVAC voltage	0.4 kV
MVAC line parameters	1.014 + j1.1929 Ω/km [9], [114]
Load-1, Load-2	0.45 MW, 0.15 MVAr
DG-1	0.2 MW

Table 4.2 Proposed Restructured System Parameters

System quantities	Values
MVDC line parameter	1.014 Ω/km [114]
MVDC voltage	20 kV
ST MV converters	0.55 MVA
ST DC-DC converters	0.45 MW
ST LV converters	0.48 MVA

the CPT is replaced by ST-1. The load-1 and DG-1 are connected to the ST-1 LVAC bus. In the main grid MVAC bus, the CPT is replaced by ST-2 and the load-2 is connected to the LVAC bus. The BTB converters are eliminated and the MVDC links of ST-1 and ST-2 are connected through MVDC distribution lines. The existing AC line infrastructure is utilized to establish MVDC interconnection [123]. Therefore, the cost related to construction of a completely new DC network infrastructure is eliminated here. The system parameters considered are given in Table 4.1 and 4.2.

4.2 MODES OF OPERATION

This section discusses the operating modes of the ST based MVDC interconnected meshed hybrid microgrid. Two operating modes are considered in this chapter, normal and emergency modes. A flowchart representation of the operating modes is given in Fig. 4.2.

4.2.1 Normal Mode

The normal operating mode is defined when the following conditions are satisfied:

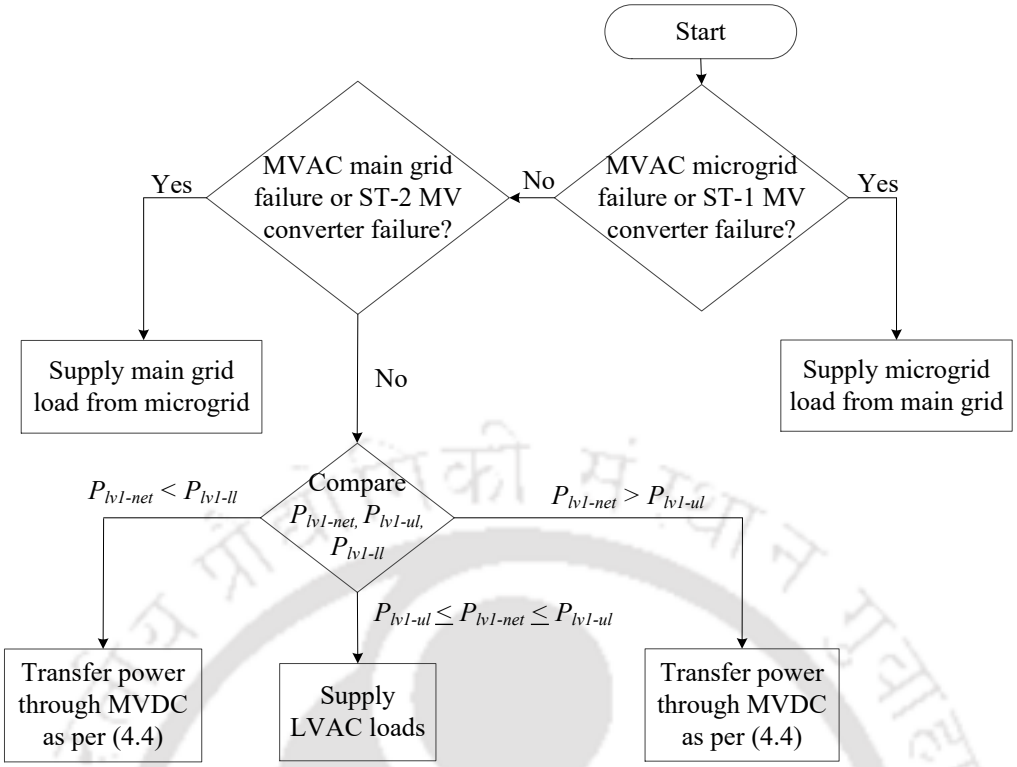

Fig. 4.2 Flowchart representation of operation of the meshed hybrid microgrid enabled using STs.

- microgrid and main grid MVAC sources are operating without any faults and delivering required power to their respective loads [64]
- The ST-1 and ST-2 MV converters are operating without fault or maintenance.

In the normal operating mode, two scenarios are considered. One scenario is independent operation of STs and another is inter-feeder power transfer. These operations are selected based on the loading on the meshed hybrid microgrid LVAC bus. The net active power loading on ST-1 LVAC bus ($P_{lv1-net}$) is given by

$$P_{lv1-net} = P_{llv1} - P_{glv1} \tag{4.1}$$

where P_{llv1} and P_{glv1}, respectively are the active power loading and generation at the microgrid LVAC bus. The power transfer to the main grid is scheduled only when the ST-1 LVAC net active power loading is less than a predefined active power lower limit (P_{lv1-ll}). Similarly, the active power absorption from main grid is scheduled during microgrid peak load hours when the ST-1 LVAC loading is greater than a predefined

active power upper limit (P_{lv1-ul}). The inter-feeder power transfer (P_t) is given by

$$P_t = P_{opr} - P_{lv1-net} \tag{4.2}$$

where P_{opr} is the predefined active power operating point. This operating power is defined based on the availability of excess power in the microgrid during low-load condition and amount of load shaving required during peak demand condition. The ST-1 MV converter power reference (P^*_{mv1}) during this mode of operation is given as

$$P^*_{mv1} = \begin{cases} P_{lv1-net}, & \text{if } P_{lv1-ll} \leq P_{lv1-net} \leq P_{lv1-ul} \\ P_{opr}, & \text{otherwise.} \end{cases} \tag{4.3}$$

If the lower or upper limits of active power loading is violated, the MVDC power transfer is initiated. The power reference (P^*_{dc}) for MVDC power transfer is given by

$$P^*_{dc} = \begin{cases} 0, & \text{if } P_{lv1-ll} \leq P_{lv1-net} \leq P_{lv1-ul} \\ P_{opr} - P_{lv1-net}, & \text{otherwise.} \end{cases} \tag{4.4}$$

The power transfer through MVDC line helps in supporting the microgrid during low and high load conditions. During the normal operating mode, the ST-2 MV converter active power reference (P^*_{mv2}) is given as

$$P^*_{mv2} = P_{llv2} \tag{4.5}$$

where P_{llv2} is the active power loading at the ST-2 LVAC side. The ST-2 power reference consists of the LVAC load requirement. The MVDC power transfer is indirectly controlled by the MVDC link voltage control.

4.2.2 Emergency Mode

In the emergency mode, two scenarios are analyzed. First one is the operation of system during the failure of MVAC microgrid/ST-1 MV converter. Second case shows the failure of MVAC main grid/ST-2 MV converter. In the event of ST-1 MV converter or MVAC microgrid failure, the ST-2 MV converter active power reference is given

by (4.5). The active power exchanged from MVAC microgrid remains at zero and the loads at the ST-1 LVAC bus is served from main grid through MVDC interconnection. Similarly, during the MVAC main grid or ST-2 MV converter failure, the ST-1 supports the ST-2 LVAC loads by the transfer of power through MVDC interconnection. The ST DC-DC converters provides the active power load requirement at the respective LVAC buses. The ST LV converters deliver the powers for the LVAC loads connected at the respective terminals.

4.3 CONTROL OF POWER CONVERTERS

In this section, the control strategy of different power converters are explained for normal and emergency modes. The overall control block diagram is shown in Fig. 4.3. The subscript i is used to indicate the ST-1, ST-2 related terms ($i = 1, 2$).

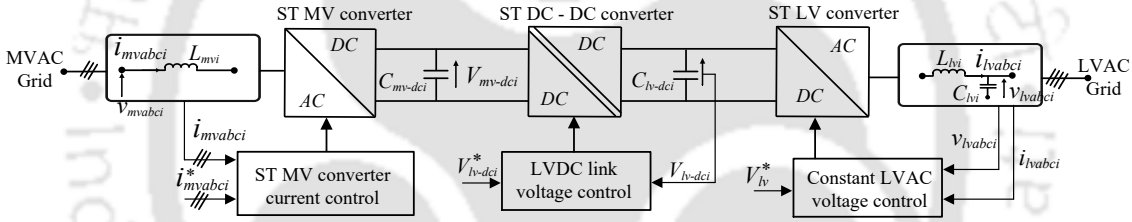

Fig. 4.3 Overall control diagram.

The control strategy of ST-1 and ST-2 MV converters are different as they need to control the power transfer between two feeders. The ST DC-DC and ST LV converters of ST-1 and ST-2 are controlled in the similar fashion; therefore, they are not explained separately.

4.3.1 ST-1 MV Converter Control

The ST-1 MV converter is controlled to exchange necessary power with the MVAC microgrid. The block-diagram representation is given in Fig. 4.4 (a) and (b). The ST-1 is selected as the primary power controller (PPC). It controls the MVDC power transfer during normal operating mode. During this mode of operation, the active power reference is given by (4.3). This includes the ST LVAC bus active power and the power transfer requirement. The generalized expression for active and reactive power refer-

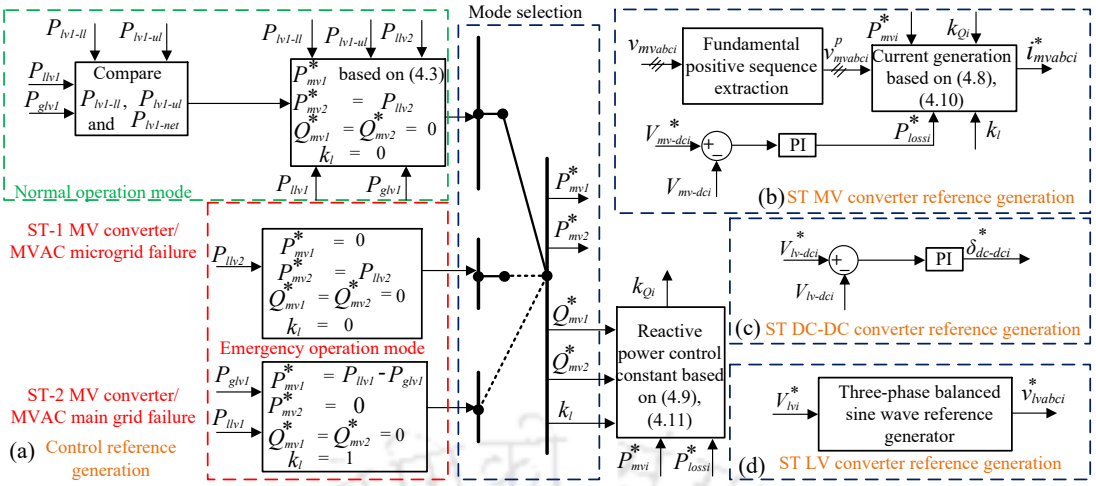

Fig. 4.4 (a) Control reference generation. (b) ST MV converter current reference generation. (c) ST DC-DC converter phase angle reference generation. (d) ST LV converter reference voltage generation.

ence (Q^*_{mv1}) is written as

$$P^*_{mv1} = P_{lv1-net} + k_{tr}P^*_{dc}\ ;\ Q^*_{mv1} = 0 \tag{4.6}$$

where k_{tr} is the control constant for the MVDC active power transfer. The MVDC power transfer is activated based on the conditions explained in Fig. 4.2. For the transfer of power through MVDC link, the constant k_{tr} assumes value 1. If there is no active power transfer, k_{tr} is given as 0.

During emergency mode, when microgrid MVAC grid or ST-1 MV converter fails, P^*_{mv1} = 0. During the MVAC main grid or ST-2 MV converter failure, the P^*_{mv1} and Q^*_{mv1} are given as

$$P^*_{mv1} = P_{lv1-net}\ ;\ Q^*_{mv1} = 0. \tag{4.7}$$

The ST-1 MV converter uses instantaneous symmetrical component theory [71] for the generation of reference currents. The three-phase reference currents (i^*_{mvabc1}) for ST-1

MV converter is given as

$$
\begin{aligned}
i^*_{mva1} &= \frac{v^p_{mva1} + k_{Q1}(v^p_{mvb1} - v^p_{mvc1})}{(v^p_{mva1})^2 + (v^p_{mvb1})^2 + (v^p_{mvc1})^2}(P^*_{mv1} + k_l P^*_{loss1}) \\
i^*_{mvb1} &= \frac{v^p_{mvb1} + k_{Q1}(v^p_{mvc1} - v^p_{mva1})}{(v^p_{mva1})^2 + (v^p_{mvb1})^2 + (v^p_{mvc1})^2}(P^*_{mv1} + k_l P^*_{loss1}) \\
i^*_{mvc1} &= \frac{v^p_{mvc1} + k_{Q1}(v^p_{mva1} - v^p_{mvb1})}{(v^p_{mva1})^2 + (v^p_{mvb1})^2 + (v^p_{mvc1})^2}(P^*_{mv1} + k_l P^*_{loss1})
\end{aligned} \tag{4.8}
$$

where v^p_{mvabc1} are fundamental positive sequence three-phase MVAC bus voltages and P^*_{mv1} is the reference power depending upon the mode of operation. P^*_{loss1} is the power loss component generated to maintain the necessary DC link voltage. The reference (V^*_{mv-dc1}) and measured (V_{mv-dc1}) MVDC link voltages are compared and the error is passed through a PI controller to generate P^*_{loss1}. However, for the normal operation, the MVDC link is controlled by the ST-2 MV converter. In this case, the MVDC link control of ST-1 is deactivated. For deactivating the ST-1 MVDC link control, the constant k_l assumes a value 0. In the event of ST-2 MVDC link control failure, the ST-1 MVDC link control is activated, and k_l = 1. The constant k_{Q1} controls the reactive power injection to the microgrid MVAC bus, and is given by

$$
k_{Q1} = \frac{Q^*_{mv1}}{\sqrt{3}(P^*_{mv1} + k_l P^*_{loss1})}. \tag{4.9}
$$

There is no reactive power exchange involved both in normal and emergency modes from ST-1 MV converter. Therefore k_{Q1} is given as zero. The reference currents generated in (4.8) are used with a hysteresis current controller to generate switching pulses.

4.3.2 ST-2 MV Converter Control

The ST-2 works as a secondary power controller (SPC). The block-diagram representation is given in Fig. 4.4 (a) and (b). During normal operation, the ST-2 MV converter reference active power is given by (4.5). In addition, during emergency mode of operation with ST-1 MV converter or MVAC microgrid failure, P^*_{mv2} is also given by (4.5). When ST-2 MV converter or MVAC main grid fails, P^*_{mv2} is zero. In all conditions, the reactive power exchange (Q^*_{mv2}) is zero. Similar to the ST-1 MV converter, the

three-phase reference currents (i^*_{mvabc2}) for ST-2 MV converter is given as

$$\begin{aligned} i^*_{mva2} &= \frac{v^p_{mva2} + k_{Q2}(v^p_{mvb2} - v^p_{mvc2})}{(v^p_{mva2})^2 + (v^p_{mvb2})^2 + (v^p_{mvc2})^2}(P^*_{mv2} + P^*_{loss2}) \\ i^*_{mvb2} &= \frac{v^p_{mvb2} + k_{Q2}(v^p_{mvc2} - v^p_{mva2})}{(v^p_{mva2})^2 + (v^p_{mvb2})^2 + (v^p_{mvc2})^2}(P^*_{mv2} + P^*_{loss2}) \\ i^*_{mvc2} &= \frac{v^p_{mvc2} + k_{Q2}(v^p_{mva2} - v^p_{mvb2})}{(v^p_{mva2})^2 + (v^p_{mvb2})^2 + (v^p_{mvc2})^2}(P^*_{mv2} + P^*_{loss2}) \end{aligned} \tag{4.10}$$

where v^p_{mvabc2} are fundamental positive sequence three-phase main grid MVAC bus voltages and P^*_{mv2} is the reference power depending upon the mode of operation. P^*_{loss2} is power loss component generated to maintain the nominal DC link voltage. The reference (V^*_{mv-dc2}) and measured (V_{mv-dc2}) MVDC link voltages are compared, and the error is passed through a PI controller to generate P^*_{loss2}. During ST-2 MV converter or MVAC main grid failures, the P^*_{loss2} is also given as zero. The constant k_{Q2} controls the reactive power injection to the main grid MVAC bus, and is given by

$$k_{Q2} = \frac{Q^*_{mv2}}{\sqrt{3}(P^*_{mv2} + P^*_{loss2})}. \tag{4.11}$$

There is no reactive power exchange involved both in normal and emergency modes from ST-2 MV converter. Therefore, k_{Q2} is given as zero. The reference currents generated in (4.10) are used with a hysteresis current controller to generate necessary switching pulses.

4.3.3 ST DC-DC Converter Control

For both ST-1 and ST-2, the DC-DC converters ensure constant power transfer between MVDC and LVDC links. The block-diagram representation is shown in Fig. 4.4(c). This is guaranteed by maintaining LVDC link voltage at the constant reference value. The measured LVDC link voltage (V_{lv-dci}) is compared with the reference value (V^*_{lv-dci}). The error is passed through a PI controller to generate a reference phase angle (δ^*_{dc-dci}). This phase angle is maintained between the MVDC and LVDC side converter switching instances. Maintaining this phase shift ensures that the required power flow is exchanged between MVDC and LVDC buses [59]. The detailed explanation for the control of this converter is given in Chapter 2.

4.3.4 ST LV Converter Control

A three-phase balanced sinusoidal voltage is required at the ST LVAC bus for both ST-1 and ST-2. The control block-diagram is shown in Fig. 4.3(d). The ST LV converter control guarantees the reference value of phase rms voltage (V^*_{lvi}) is maintained at 50 Hz frequency and 120° phase difference between phases. This is ensured by controlling the ST LV converter as a grid forming voltage source converter [9], [96]. The detailed explanation for this converter operation is provided in Chapter 2.

4.4 PERFORMANCE COMPARISON

In this section, the performance of the proposed system is compared with different existing solutions [64], [114], [121]. Reactive power capability and active power loss comparison with existing literature is explained. Different system parameters considered are given in Table 4.1 and Table 4.2.

4.4.1 Reactive Power Capability

Reactive power capability of microgrid is an important feature to ensure necessary voltage support and stability. In the conventional AC microgrid shown in Fig. 4.1(a), the DG converter can be utilized with full capacity to provide reactive power support. During this time, the active power exchange from DG needs to be reduced to zero. The reactive power availability is given as

$$Q_{DG1} = S_{DG1} \tag{4.12}$$

where Q_{DG1} is the reactive power rating of DG and S_{DG1} is the rating of DG.

In the second case, the AC system shown in Fig. 4.1(b) is considered. The reactive power availability (Q_{tot1}) at the MVAC microgrid bus is given by

$$Q_{tot1} = S_{DG1} + S_{BTB1} \tag{4.13}$$

where S_{BTB1} is the rating of BTB converter. Here, the DG-1 capacity is also considered

for reactive power support.

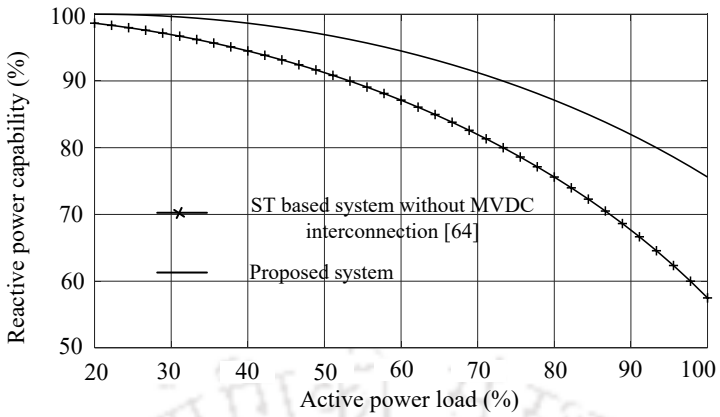

Fig. 4.5 Reactive power capability comparison.

In the third case, an ST based microgrid is considered without MVDC interconnection. The reactive power availability from ST-1 MV converter is given by

$$Q_{mv1} = \sqrt{S_{mv1-rat}^2 - P_{llv1}^2} \tag{4.14}$$

where $S_{mv1-rat}$ is the rating of ST-1 MV converter and P_{llv1} is the loading on the LVAC bus. The generation at the ST-1 LVAC bus is not considered to analyze the maximum loading condition on ST-1 MV converter.

In the proposed system shown in Fig. 4.1(c), if the ratings is considered similar to the ST system without MVDC interconnection, the reactive power availability at the MVAC microgrid is given as

$$Q_{mv1} = \sqrt{S_{mv1-rat}^2 - (P_{llv1} - P_{dc})^2} \tag{4.15}$$

where P_{dc} is the transferred power from the main grid.

The percentage reactive power capability ($Q_{cap-perc}$) of ST-1 MV converter is given as

$$Q_{cap-perc} = \frac{Q_{mv1}}{S_{mv1-rat}} \times 100. \tag{4.16}$$

The reactive power availability in microgrid MVAC bus is constant irrespective of the LVAC loading both in the conventional AC system and AC system with BTB converters. In addition, generally BTB converters are rated only for the maximum active power transfer. The percentage reactive power capability of ST-1 MV converter is plotted

against percentage ST-1 LVAC loading in Fig. 4.5 for the proposed system and the ST based system without MVDC interconnection. The proposed system has the better reactive power capability compared to the ST system without MVDC interconnection.

4.4.2 Active Power Loss

Active power loss is important during the inter-feeder power transfer. In the conventional AC system shown in Fig. 4.1(a), the controlled active power transfer is not possible. However, for the system shown in Fig. 4.1(b), the controlled power transfer is possible with BTB system. The active power loss ($P_{loss-ac}$) for transferring the power from one feeder to other is given by [123]

$$P_{loss-ac} = \frac{P_{li}^2 + Q_{li}^2}{V_{bill}^2} R_{acij} \tag{4.17}$$

where P_{li} and Q_{li} are the load active and reactive powers of bus-i. V_{bill} is the bus-i voltage (L-L). R_{acij} is the line resistance in Ohms (Ω) per kilometre.

In the ST based system without MVDC interconnection, the controlled power transfer is not possible since the power is transferred through the AC system [64]. In this case, the ST LV converters supply the required load reactive power and it is not absorbed from the other feeder. Therefore, the active power loss in this case is

$$P_{loss-ac} = \frac{P_{li}^2}{V_{bill}^2} R_{acij}. \tag{4.18}$$

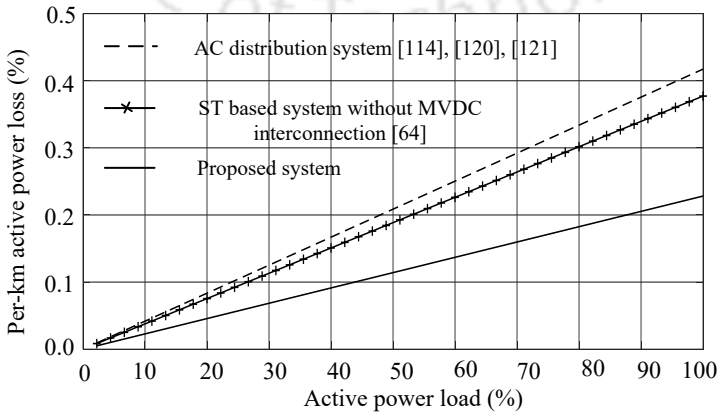

Fig. 4.6 Comparison of active power loss during inter-feeder power transfer.

In the proposed ST based MVDC system, the controlled active power transfer is enabled

Table 4.3 Performance Comparison

Parameter	Conventional AC system [114], [120]	AC system with BTB system [121]	ST based system without MVDC interconnection [64]	Proposed system
Loss during inter-grid power transfer	High	High	Moderate	Low
Controlled inter-grid power transfer	Not available	High flexibility	Not available	High flexibility
Reactive power capability	Low	Low	Moderate	High
Continuous operation of LVAC system during MVAC microgrid failure	Not possible	Not possible	Not possible	Possible
Re-synchronization of DG after MVAC microgrid failure	Required	Required	Required	Not required

Table 4.4 Simulation Parameters

System quantities	Values
ST MV converters	L_{mvi} = 100 mH
ST LV converters	L_{lvi} = 0.5 mH, C_{lvi} = 20 μF
DC link capacitors	C_{mv-dci} = 2000 μF, C_{lv-dci} = 2500 μF
ST DC-DC converters	L_{mvdc} = 10 mH, f_{sw} = 1 kHz

through MVDC interconnection and is given as [123]

$$P_{loss-dc} = \frac{2P_{li}^2}{V_{dci}^2} R_{dcij} \tag{4.19}$$

where V_{dci} is the MVDC link voltage at the ST-i terminal and R_{dcij} is the line resistance in Ω per kilometre.

The percentage reduction in losses ($\Delta P_{loss-perc}$) for the proposed system as compared to the ST based AC system without MVDC interconnection given in (4.18) is

$$\Delta P_{loss-perc} = (1 - \frac{2V_{bill}^2 R_{dcij}}{V_{dci}^2 R_{acij}}) \times 100. \tag{4.20}$$

Considering same AC and DC line resistances, the percentage active power loss reduction is nearly 40% for the proposed system. The percentage of per-kilometre active power loss for a particular amount of active power transfer is calculated. This quantity is plotted against the percentage active power in Fig. 4.6 for different systems. The proposed system curve shows the lowest active power loss percentage. The main features of different distribution systems are compared in Table 4.3. The proposed system has lower losses and higher reactive power capability. The controlled active power transfer is available with both the BTB based system and the proposed system. However, among the various systems shown in Table 4.3, the continuous operation of LVAC system during MVAC microgrid failure is available only with the proposed system. Moreover, the DG re-synchronization requirement during MVAC microgrid failure is avoided only in the proposed system.

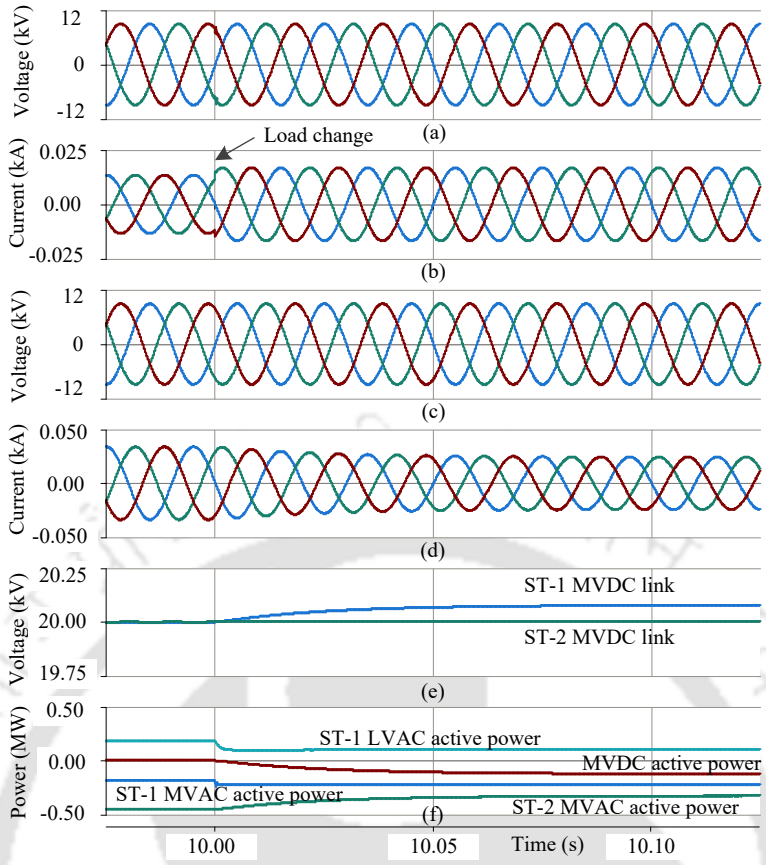

Fig. 4.7 Simulation results for light-load operation of microgrid. (a) Microgrid MVAC voltages. (b) ST-1 MV converter currents. (c) Main grid MVAC voltages. (d) ST-2 MV converter currents. (e) MVDC link voltages. (f) Different active powers.

4.5 SIMULATION RESULTS

The simulation analysis is carried out in PSCAD/EMTDC software. Different parameters are given in Table 4.1, 4.2, and 4.4. Normal and emergency mode operations are shown in the simulation.

4.5.1 Normal Mode

In Fig. 4.7, the power transfer during normal mode of microgrid LVAC bus is demonstrated. The microgrid LVAC bus loading is 40% of the maximum load till t = 10 s. The P_{lv1-ll} is set as 25% of the maximum load. At t = 10 s, the load decreases below P_{lv1-ll}. The P_{opr} is selected as 50% of the maximum load. As discussed in the Fig. 4.2, the power is transferred from MVAC microgrid to main grid through MVDC line. Fig. 4.7(a) and (c) show the microgrid and main grid MVAC voltages, respectively. Fig. 4.7(b) and (d) show the ST-1 and ST-2 MV converter currents. The ST-2 MV converter

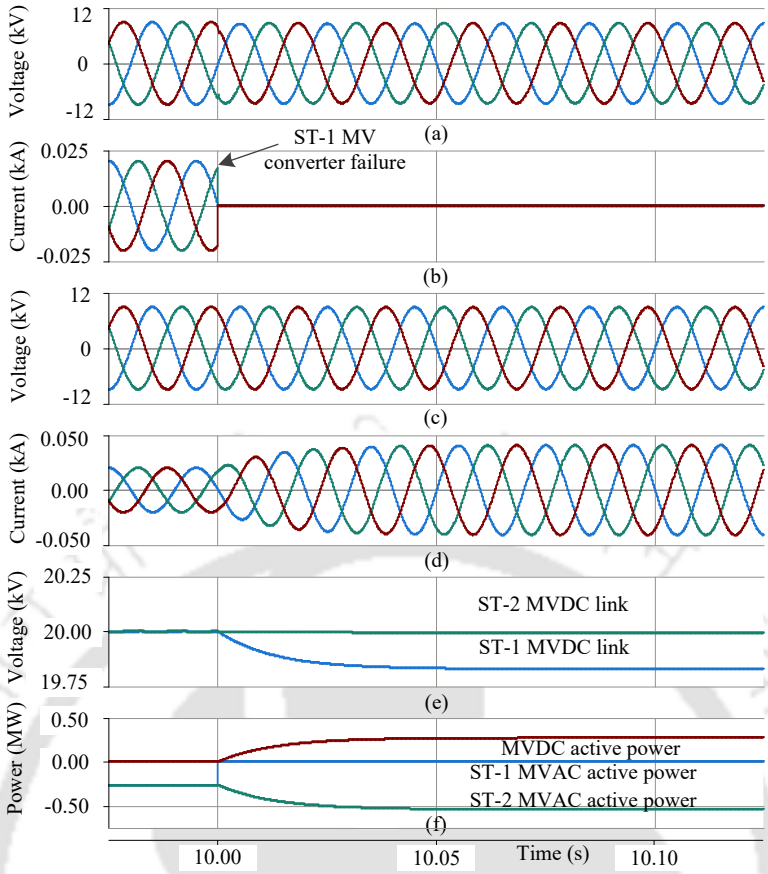

Fig. 4.8 Simulation results during ST-1 MV converter failure. (a) Microgrid MVAC voltages. (b) ST-1 MV converter currents. (c) Main grid MVAC voltages. (d) ST-2 MV converter currents. (e) MVDC link voltages. (f) Different active powers.

currents decrease after load change due to MVDC power transfer from microgrid. The MVDC link voltages are shown in Fig. 4.7(e). The ST-1 MVDC link voltage increases to facilitate the power transfer. Fig. 4.7(f) shows ST-1 and ST-2 MVAC active powers, ST-1 LVAC load active power, and MVDC power transferred. The load power decreases after t = 10 s, and more power is transferred from microgrid to the main grid. The ST-2 MVAC active power decreases because of the active power transfer through MVDC line.

4.5.2 Emergency Mode

In this mode, two cases are analyzed (1) ST-1 MV converter failure, (2) MVAC main grid source failure. In the first case shown in Fig. 4.8, the ST-1 MV converter fails due to fault at t = 10 s. Before the fault, the ST-1 and ST-2 MV converters supply their own LVAC loads. Fig. 4.8(a) shows the MVAC microgrid voltage. Fig. 4.8(b) shows the ST-1 MV converter currents that decrease to zero after t = 10 s due to ST-1

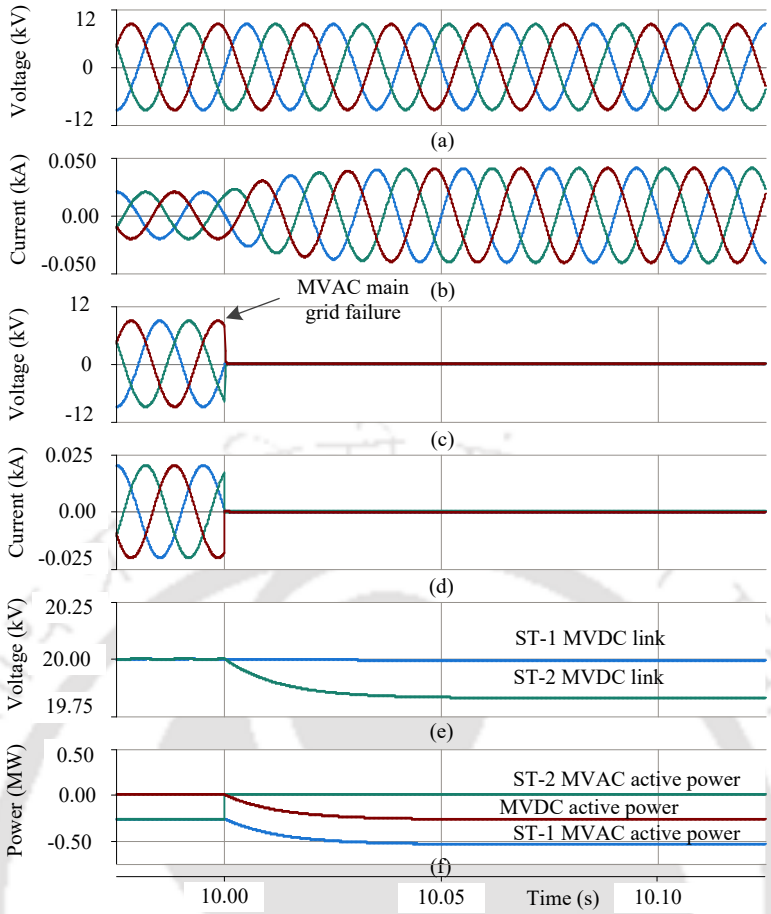

Fig. 4.9 Simulation results for MVAC main grid failure. (a) Microgrid MVAC voltages. (b) ST-1 MV converter currents. (c) Main grid MVAC voltages. (d) ST-2 MV converter currents. (e) MVDC link voltages. (f) Different active powers.

MV converter failure. Fig. 4.8(c) shows the main grid MVAC voltages and Fig. 4.8(d) shows the ST-2 MV converter currents. Fig. 4.8(e) shows the MVDC link voltages of ST-1 and ST-2. The ST-1 MVDC link voltage decreases to facilitate the active power transfer from MVAC grid to microgrid LVAC loads. Different active powers are shown in Fig. 4.8(f). The ST-1 MVAC active power reduces to zero after the fault. The ST-2 MVAC active power increases to support the ST-1 LVAC loads.

In the second case, the main grid MVAC source failure situation is analyzed. Till t = 10 s, both the feeders are operating in healthy condition. Both ST-1 and ST-2 supply their own LVAC loads. Fig. 4.9(a) and (c) show the microgrid and main grid MVAC voltages, respectively. Fig. 4.9(b) and (d), respectively show ST-1 and ST-2 MV converter currents. Main grid MVAC bus voltages and ST-2 MV converter currents reduce to zero after the MVAC main grid source failure. Fig. 4.9(e) shows MVDC link voltages. The ST-2 MVDC link voltage reduces after MVAC source failure which facilitates the power transfer from microgrid MVAC grid to main grid LVAC loads. The ST-1 MV converter

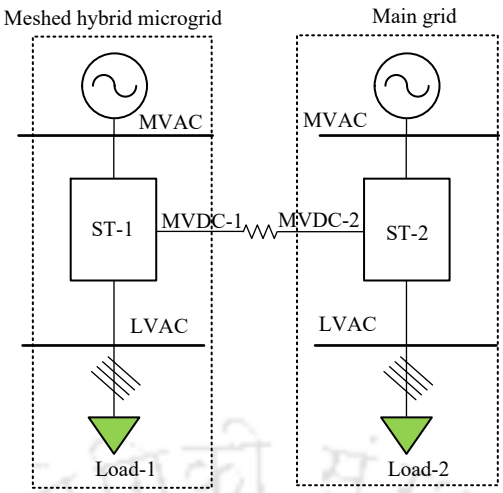

Fig. 4.10 Experimental setup schematic.

Table 4.5 Experimental Parameters

System quantities	Values
MVAC grid voltage	150 V
LVAC grid voltage	110 V
ST MV converters	L_{mv} = 13 mH,
ST LV converters	L_{lv} = 5 mH, C_{lv} = 10 μF
DC link voltage	V_{dc} = 275 V

maintains the MVDC link voltage at nominal value. Fig. 4.9(f) shows different active powers. The ST-2 MVAC active power reduces to zero after the MVAC grid failure. The ST-1 MVAC active power increases to transfer the load at ST-2 LVAC side. The MVDC power increases due to power transfer from microgrid to the ST-2 LVAC loads.

4.6 EXPERIMENTAL RESULTS

The experimental schematic is shown in Fig. 4.10. The experimental parameters are shown in Table 4.5. All the cases shown in simulation analysis are verified in the experimental analysis.

4.6.1 Normal Mode

The normal operation shown in Fig. 4.11 exhibits the MVDC power transfer based on the loading condition. The ST-1 and ST-2 supplies their own loads. The load change

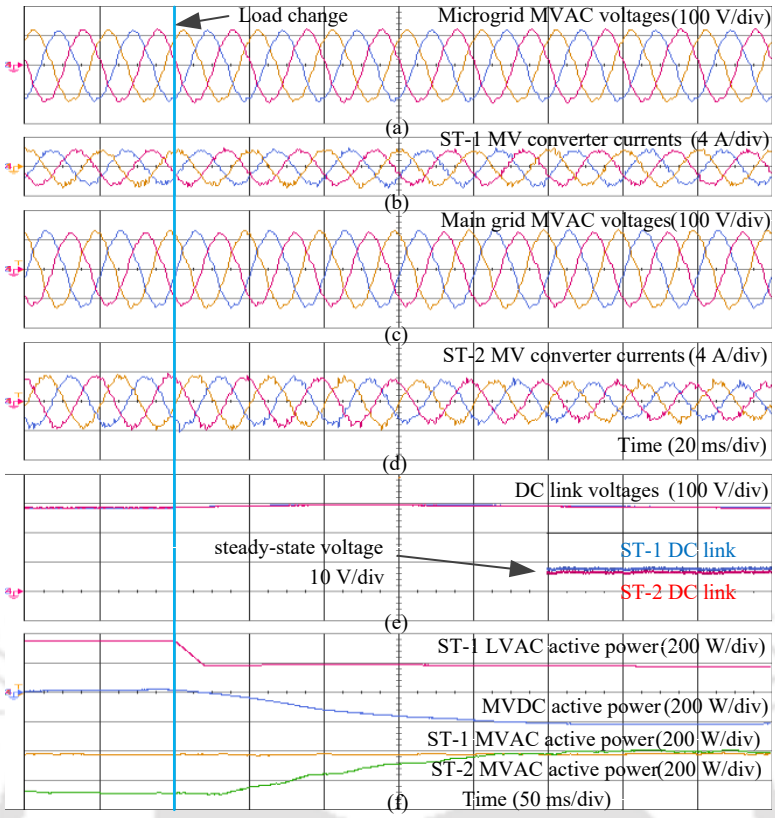

Fig. 4.11 Experimental results for light-load operation of microgrid. (a) Microgrid MVAC voltages. (b) ST-1 MV converter currents. (c) Main grid MVAC voltages. (d) ST-2 MV converter currents. (e) MVDC link voltages. (f) Different active powers.

is marked in Fig. 4.11, and the ST-1 LVAC load decreases. As the load in ST-1 LVAC converter becomes lower than the limit, the active power transfer from microgrid to main grid is initiated. This is visible in the Fig. 4.11 waveforms. Fig. 4.11(a) shows the microgrid MVAC voltages and Fig. 4.11(b) shows the ST-1 MV converter currents. The main grid MVAC voltages are shown in Fig. 4.11(c). The ST-2 MVAC currents decrease as seen in Fig. 4.11(d), since a portion of the ST-2 loads are supplied from microgrid through the MVDC line. The MVDC link voltages are shown in Fig. 4.11(e). The ST-1 LVAC power decreases as shown in Fig. 4.11(f). In addition, ST-1, ST-2 MV, and MVDC active powers are shown in Fig. 4.11(f). The ST-2 MV active power reduces as a portion of active power is supplied from the microgrid. The MVDC power indicates the power transfer through the MVDC line.

4.6.2 Emergency Mode

In the first case shown in Fig. 4.12, the ST-1 MV converter fails due to the converter fault. Till the occurrence of fault, the ST-1 and ST-2 MV converters supply their own

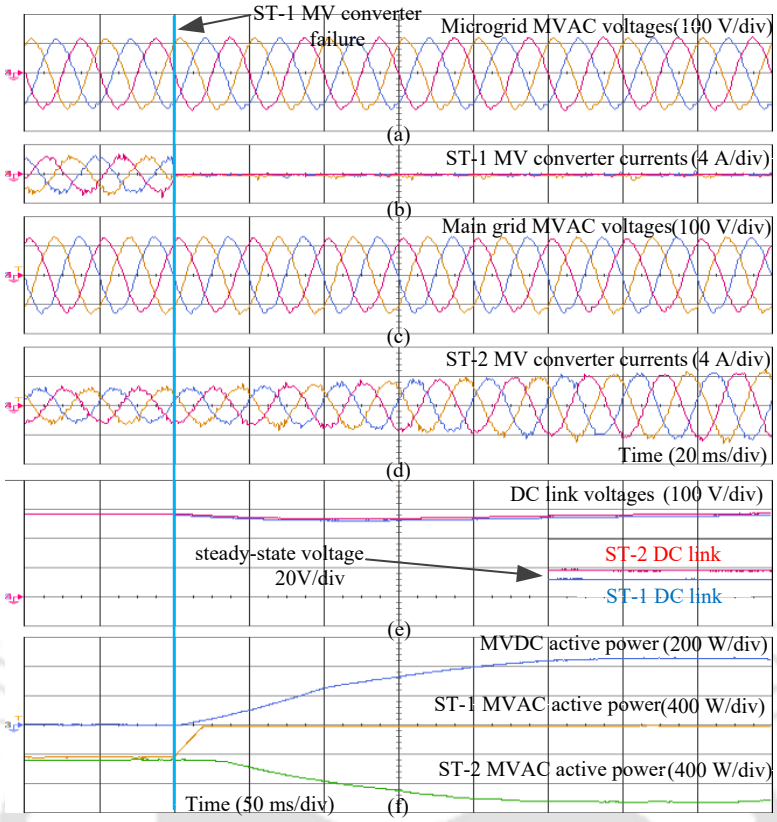

Fig. 4.12 Experimental results during ST-1 MV converter failure. (a) Microgrid MVAC voltages. (b) ST-1 MV converter currents. (c) Main grid MVAC voltages. (d) ST-2 MV converter currents. (e) MVDC link voltages. (f) Different active powers.

LVAC loads. After the fault, the ST-2 MV converter supplies the ST-1 LVAC loads through the MVDC line. Fig. 4.12(a) shows the microgrid MVAC voltages and Fig. 4.12(b) shows the ST-1 MV converter currents. The ST-1 MV converter currents decrease to zero after the converter failure. The main grid MVAC voltages are shown in Fig. 4.12(c). The ST-2 MV converter currents increase as seen in Fig. 4.12(d), since the ST-1 loads are supplied from main grid through the MVDC line. The MVDC link voltages are shown in Fig. 4.12(e), and the ST-1 DC link voltage decreases to facilitate the power transfer. Different active powers are shown in Fig. 4.12(f). The ST-1 MV active power reduces to zero after the failure. The ST-2 MV active power increases to supply the ST-1 LVAC loads. The active power transfer through the MVDC line supports the ST-1 LVAC loads.

In the second case shown in Fig. 4.13, the MVAC grid failure condition is analyzed. Fig. 4.13(a) shows the microgrid MVAC voltages and Fig. 4.13(b) shows the ST-1 MV converter currents. Till the MVAC grid failure, the ST-1 and ST-2 MV converters supply their own loads. The ST-1 MV converter currents increase after the MVAC grid

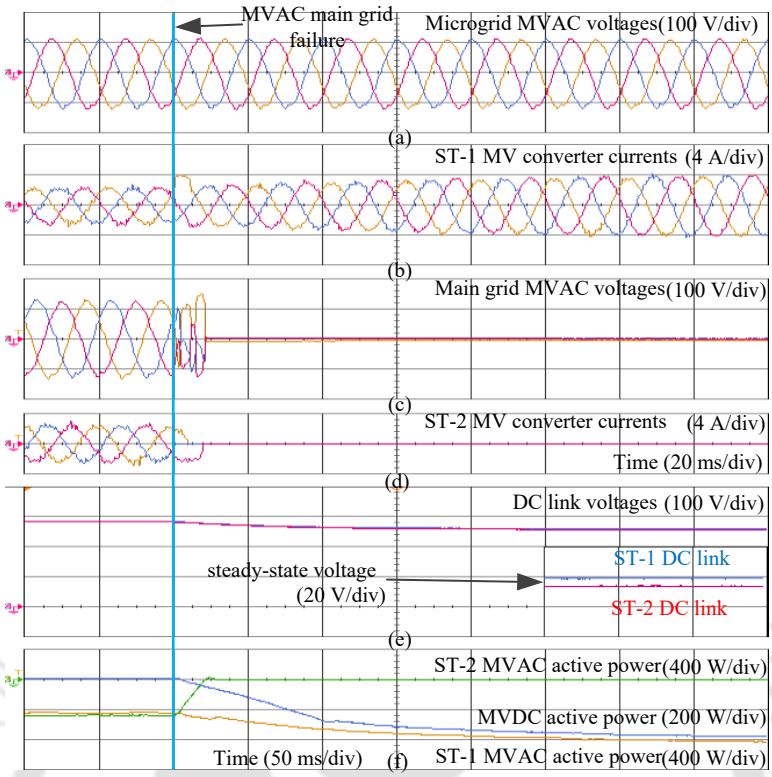

Fig. 4.13 Experimental results for MVAC main grid failure. (a) Microgrid MVAC voltages. (b) ST-1 MV converter currents. (c) Main grid MVAC voltages. (d) ST-2 MV converter currents. (e) MVDC link voltages. (f) Different active powers.

failure. The main grid MVAC voltages are shown in Fig. 4.13(c), and it decrease to zero after the grid failure. The ST-2 MV converter currents also decrease to zero as seen in Fig. 4.13(d). The MVDC link voltages are shown in Fig. 4.13(e), and the ST-2 DC link voltage decreases to facilitate power transfer. Different active powers are shown in Fig. 4.13(f). The ST-2 MVAC active power reduces to zero after the grid failure. The ST-1 MV converter power increases, and the ST-2 LVAC loads are supplied through the interconnected DC line.

4.7 CONCLUSIONS

The simulation and experimental results verify the performance of an MVDC interconnected meshed hybrid microgrid configuration enabled with STs. The proposed system provides several advantages such as (1) controlled active power transfer capability with high flexibility in power flow, (2) for the inter-feeder power transfer, the active power line losses are 40% lower than the ST system without MVDC interconnection, (3) nearly 30% more reactive power capability at full load operating condition

in comparison with the ST system without MVDC interconnection, and (4) continuous operation of LVAC distribution system in case of MVAC main grid/microgrid failure conditions, and avoids the requirement of DG resynchronization.

CHAPTER 5

OPERATION OF MESHED HYBRID MICROGRID DURING ADVERSE GRID CONDITIONS WITH STORAGE INTEGRATED SMART TRANSFORMER

In Chapter 4, the ST based meshed hybrid configuration is introduced. Various advantages of this system over existing conventional systems were explored. Also, the operation during grid and converter failure conditions were analyzed. The DG source is considered in the system; however, the reverse power flow from DG is not studied, and the ST control capabilities are not analyzed. Also, the integration of BESS into the system for MVAC grid support functions is not considered. This chapter further extends the study on this configuration with the integration of PV based DG source and BESS to the microgrid.

Due to high DG penetration, the reverse power flow scenario arises in the distribution grid. The uncontrolled reverse power flow can introduce voltage rise in the system. Conventionally, the voltage rise due to reverse power flow is handled by solutions such as OLTCs [97], and active power control of PV inverters [113]. The peak load demand on the system often leads to unmanageable active power burden on the system, and this creates spikes in the load curve. The BESS is considered to be an option for providing active power support during the peak loading hours [124]. Voltage disturbances and different mitigation techniques are discussed in previous chapters. Beyond the mitigation plans, maintaining the continuity of power supply to the LVAC loads during MVAC grid voltage sags improves the reliability of the system. From the problems mentioned above and literature explored in Chapter 1, the following are the observations:

- The reverse power flow from PV sources introduces voltage rise in the distribution grids
- The peak load management feature is important to smooth the load curve
- Continuous operation of loads during voltage sags improve the reliability of distribution system

- The operation of the meshed hybrid microgrid introduced in Chapter 4 with BESS integration needs further analysis to address the issues such as peak load demand, peak PV generation and grid voltage sag.

This chapter analyzes the operation of BESS integrated ST based meshed hybrid microgrid during adverse grid conditions. The peak load management, reverse power flow control, and voltage sag operation are considered in this chapter for further analysis.

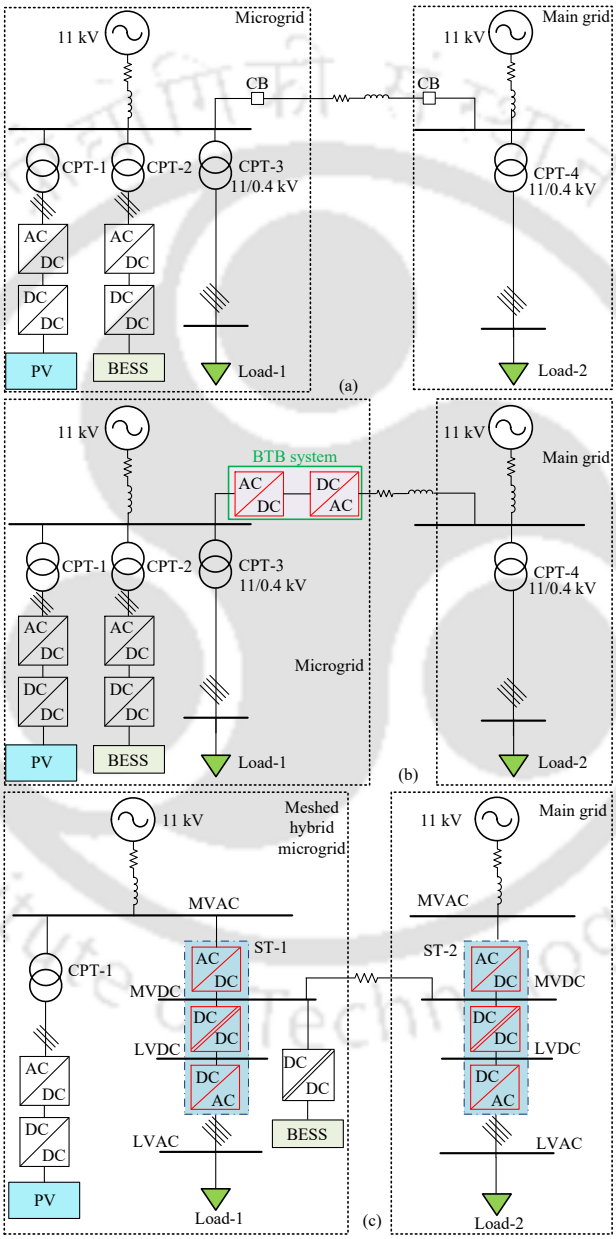

Fig. 5.1 Single-line diagram of the system. (a) A conventional microgrid configuration horizontally coupled with the main grid [114], [120]. (b) A BTB system interconnected microgrid [121]. (c) ST based meshed hybrid microgrid.

Table 5.1 System Parameters

System quantities	Values
MVAC grid voltage	11 kV
LVAC voltage	0.4 kV
MVAC line parameters	1.014 + j1.1929 Ω/km [9], [114]
Load-1, Load-2	0.45 MW, 0.15 MVAr
ST MV converters	0.55 MVA
ST DC-DC converters	0.45 MW
ST LV converters	0.48 MVA
PV converters	0.45 MW
BESS converters	0.2 MW
BESS capacity	0.2 MWh

5.1 SYSTEM CONFIGURATION

Fig. 5.1(a) shows a conventional AC microgrid configuration derived from [114], [120]. The 11-kV source in the microgrid is constituted by a number of renewable sources. The 11-kV bus of the microgrid is horizontally coupled to a main grid bus through AC distribution line and NO CBs. The PV-based DG source is connected to the MVAC bus of microgrid through DC-DC, DC-AC converters and CPT. The BESS is connected to the microgrid through DC-DC, DC-AC converters and CPT. The load (Load-1) is connected to the LVAC bus through the 11/0.4 kV CPT. In main grid MVAC bus, load (Load-2) is connected through 11/0.4 kV CPT.

Fig. 5.1(b) shows microgrid configuration connected to the main grid through BTB converter interconnected AC distribution line derived from [121]. The BTB system introduces the controlled active power flow between microgrid and main grid. All other system components remain same as Fig. 5.1(a).

In the ST based configuration, ST-1 and ST-2 replaces the CPT-2, CPT-3 and CPT-4 as shown in Fig. 5.1(c). The BESS is connected to ST-1 MVDC link through an isolated DAB converter [125]. The loads in the microgrid are connected to the ST-1 LVAC bus. In the main grid, the loads are connected to the ST-2 LVAC bus. Similar to previous chapters, a three-stage configuration of ST is used. All the system parameters are given in Table 5.1.

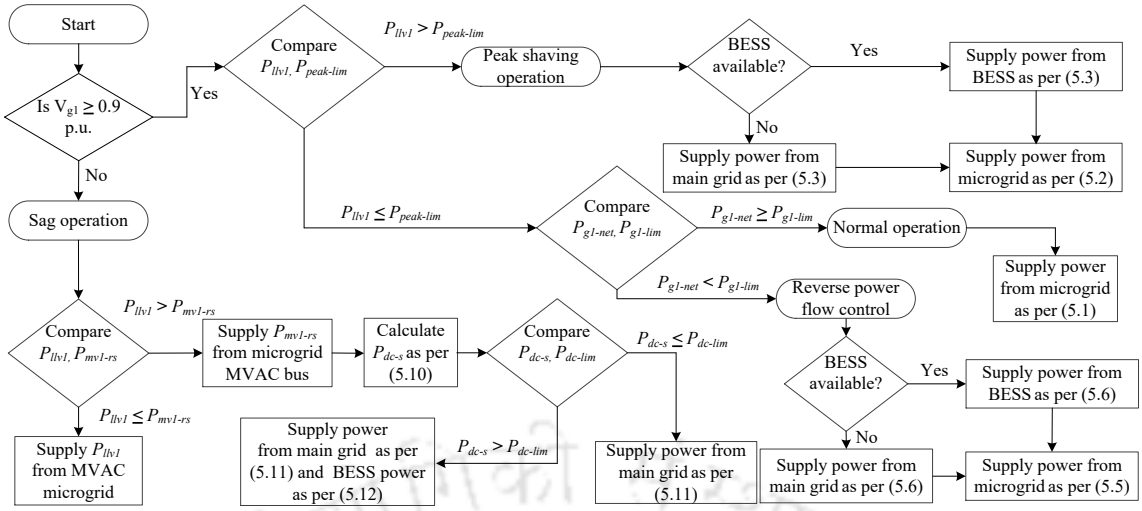

Fig. 5.2 Flowchart representation of modes of operation.

5.2 MODES OF OPERATION

This chapter considers four modes of operation. They are named as mode-1, mode-2, mode-3, and mode-4. The transition of operation from one mode to another is also discussed in this section. Fig. 5.2 shows a flowchart of various operating modes.

5.2.1 Mode-1: Normal Operation

In the normal operation, the ST-1 and ST-2 supply their own LVAC loads. In addition, the BESS charging is carried out through the ST-1 MV converter to maintain appropriate SOC. The active power references for MV converters of ST-1 (P^*_{mv1}) and ST-2 (P^*_{mv2}) are given by

$$\begin{aligned} P^*_{mv1} &= P_{llv1} + P^*_b \\ P^*_{mv2} &= P_{llv2} \end{aligned} \tag{5.1}$$

where P_{llv1} and P_{llv2} are the loading on ST-1 and ST-2 LVAC buses, respectively. P^*_b is the BESS charging power reference.

5.2.2 Mode-2: Peak Load Shaving Operation

The peak load shaving is typically employed to eliminate demand spikes in the system that causes the extreme power demands from the energy sources. This mode of

system operation supports the grid during peak loading hours. The ST-1 LVAC load is supported either from the BESS or from the main grid through MVDC link. This mode is activated when the ST-1 LVAC load exceeds the predefined peak demand limit ($P_{peak-lim}$). In this case, the ST-1 MV converter active power reference is given by

$$P^*_{mv1} = P_{peak-lim}, \text{ if } P_{llv1} > P_{peak-lim}. \tag{5.2}$$

P^*_{mv2} remains same as given in (5.1). If the BESS is available for discharge, the power is delivered from BESS. In the event of BESS unavailability, the power is transferred from main grid through MVDC line. Therefore, the BESS discharge power reference (P^*_b) and the MVDC transfer power reference (P^*_{dc}) are given by

$$P^*_b = P^*_{dc} = P_{peak-lim} - P_{llv1}, \text{ if } P_{llv1} > P_{peak-lim}. \tag{5.3}$$

A negative value of P^*_b is given to the controller for BESS discharge. Similarly, a negative value of P^*_{dc} indicates power transfer from main grid to microgrid. This active power support helps in reducing peak load demand on the microgrid MVAC bus.

5.2.3 Mode-3: Reverse Power Flow Control

The increased power generation from PV source leads to reverse power flow in the system that can cause voltage rise. This mode controls the reverse power flow in the microgrid by the ST's absorption of active power from the MVAC microgrid bus. The absorbed active power is either stored in BESS or transferred to the main grid through MVDC line. The net active power import (P_{g1-net}) in the microgrid is given by

$$P_{g1-net} = P_{llv1} - P_{lv1-pv} \tag{5.4}$$

where P_{lv1-pv} is the active power generation from PV generator. During low-load, peak-generation hours, the active power from PV is absorbed through ST-1 MV converter depending upon the predefined power export limit (P_{g1-lim}). The ST-1 MV converter reference power is given by

$$P^*_{mv1} = P_{lv1-pv} - P_{g1-lim}, \text{ if } P_{g1-net} < P_{g1-lim}. \tag{5.5}$$

The ST-2 MV converter active power reference remains same as given in (5.1). The absorbed power is either used for BESS charging, and if BESS is not available for charging, the power is transferred to the main grid. Therefore, the BESS charging power reference and the MVDC transfer power reference is given by

$$P_b^* = P_{dc}^* = -P_{g1-net} - P_{g1-lim}, \text{ if } P_{g1-net} < P_{g1-lim}. \tag{5.6}$$

The extra absorption of active power limits the reverse power flow in microgrid and thereby avoiding the voltage rise conditions.

5.2.4 Mode 4: Voltage Sag Operation

Voltage sags are caused by different faults in the grid and it affects the availability of power supply to the customers. If the microgrid MVAC voltage magnitude is lower than 90% of the nominal value, the ST-1 operates in sag operating mode. In this mode, the ST-1 MV converter is controlled to continue the operation with reduced power absorption. Due to the constant power operation of grid-connected ST-1 MV converter, the absorption of currents increases during MVAC voltage sag to maintain the load power supply. In this chapter, the ST-1 MV converter is controlled in coordination with ST-2 and BESS for ensuring the reliability of power supply for the ST-1 LVAC loads during microgrid MVAC voltage sags.

The reactive power exchange is not considered during this operating mode. The apparent power rating (S_{mv1-rn}) of ST-1 MV converter during nominal microgrid voltage condition is equal to the active power rating (P_{mv1-rn}) given by

$$P_{mv1-rn} = \sqrt{3} V_{g1-n} I_{mv1-r} \tag{5.7}$$

where V_{g1-n} is the microgrid MVAC nominal rms voltage and I_{mv1-r} is the ST-1 MV converter rms current rating. In the event of microgrid MVAC voltage sag, the voltage (V_{g1-s}) is lower than the nominal value. For limiting the currents within the rating, the maximum apparent power (S_{mv1-rs}) that can be absorbed during sag is limited to a lower value as compared to S_{mv1-rn}. During sag, the active power rating (P_{mv1-rs}) same

as the S_{mv1-rs}, is given by

$$P_{mv1-rs} = \sqrt{3}V_{g1-s}I_{mv1-r} = M_s P_{mv1-rn} \quad \text{where } M_s = \frac{V_{g1-s}}{V_{g1-n}}. \tag{5.8}$$

In the case when ST-1 MV converter effective rating during sag is less than the ST-1 LVAC demand, the balance power is transferred from main grid through MVDC line. However, the maximum power transfer during this mode is limited to a fixed value (P_{dc-lim}) and the remaining power is absorbed from the BESS.

The active power requirement for the LVAC load is absorbed from microgrid MVAC bus by the ST-1 MV converter subject to its rating and the ST-1 LVAC load. The ST-1 MV converter power reference during voltage sag is given as

$$P^*_{mv1} = \begin{cases} P_{llv1}, & \text{if } P_{llv1} \leq P_{mv1-rs} \\ P_{mv1-rs}, & \text{otherwise.} \end{cases} \tag{5.9}$$

Based on the ST-1 LVAC loading and depth of voltage sag, the ST-1 demands power from the main grid. The MVDC power transfer requirement is given by

$$P_{dc-s} = \begin{cases} 0, & \text{if } P_{llv1} \leq P_{mv1-rs} \\ P_{llv1} - P_{mv1-rs}, & \text{otherwise.} \end{cases} \tag{5.10}$$

The MVDC power requested from the ST-1 may exceed the power transfer limit. Therefore, depending on the requested active power and the maximum power transfer limit, the MVDC power transfer reference (P^*_{dc}) is given by

$$P^*_{dc} = \begin{cases} -P_{dc-s}, & \text{if } P_{dc-s} \leq P_{dc-lim} \\ -P_{dc-lim}, & \text{otherwise.} \end{cases} \tag{5.11}$$

The P^*_{dc} is limited to a maximum value of P_{dc-lim} and BESS is activated if P_{dc-s} exceeds the P_{dc-lim}. Depending upon the active power supplied from the main grid, the ST-1 may require support from BESS. The BESS power reference (P^*_b) during the sag

operation is given by

$$P_b^* = \begin{cases} 0, & \text{if } P_{dc-s} \leq P_{dc-lim} \\ -(P_{dc-s} - P_{dc-lim}), & \text{otherwise.} \end{cases} \tag{5.12}$$

BESS transfers the remaining power to support the ST-1 LVAC load based on the requirement. The ST-2 MV converter reference remain same as given in (5.1).

5.3 CONTROL OF POWER CONVERTERS

In this section, the control of ST converters are explained. In addition, the BESS converter control is also explained. Overall control diagram is shown in Fig. 5.3.

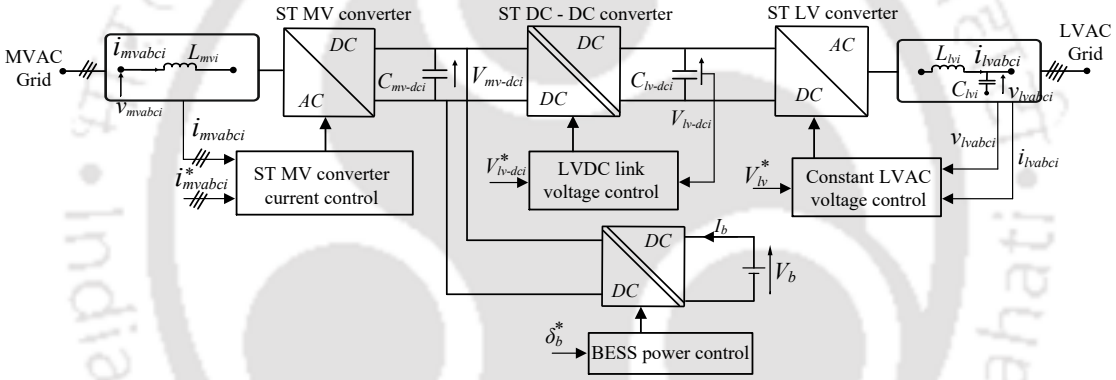

Fig. 5.3 Overall control diagram.

5.3.1 ST-1 MV Converter Control

The aim of ST-1 MV converter is to support its LVAC loads and exchange power with ST-2 through MVDC link. It is also used to charge/discharge the BESS. The control diagram is shown in Fig. 5.4(a) and (b). For the mode-1 to mode-4, the active power references are given by (5.1), (5.2), (5.5), and (5.9), respectively. A generalized expression for the ST-1 MV converter reference active power is given by

$$P^*_{mv1} = P_{llv1} + P^*_{dc} + P^*_b. \tag{5.13}$$

In mode-2 to mode-4, the inter-grid power transfer is controlled by ST-1 using indirect MVDC voltage control. Considering a constant DC link voltage at the ST-2 MVDC

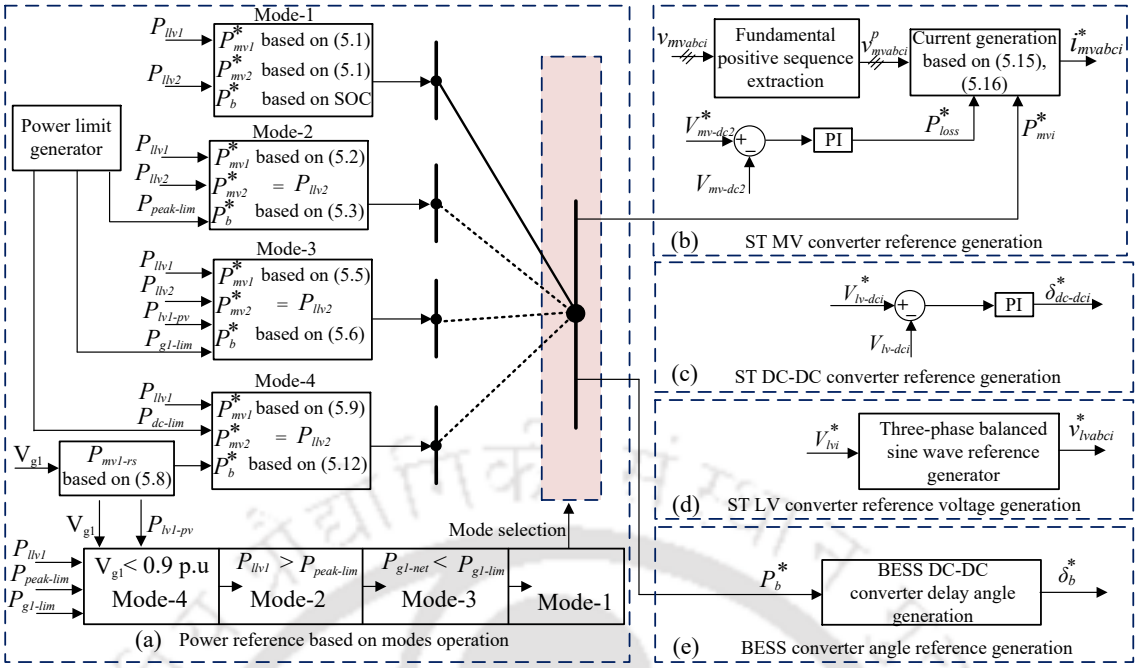

Fig. 5.4 (a) Power reference based on modes of operation. (b) ST MV converter current reference generation. (c) ST DC-DC converter phase angle reference generation. (d) ST LV converter reference voltage generation. (e) Reference phase angle generation of BESS converter.

link, the ST-1 MVDC voltage is expressed as

$$V_{mv-dc1} = V_{mv-dc2} + P^*_{dc}\frac{2R_{dc}}{V_{mv-dc2}} \tag{5.14}$$

where V_{mv-dc1} and V_{mv-dc2} are the voltages at ST-1 and ST-2 MVDC links, respectively. R_{dc} is the resistance of DC line. A positive P^*_{dc} indicates that the power is transferred from microgrid to main grid, and a negative P^*_{dc} indicates the power transfer from main grid to microgrid. The ST-1 MVDC voltage variation based on P^*_{dc} is shown in Fig. 5.5. The P^{max}_{dc} is the maximum power transfer and V^h_{mv-dc1}, V^l_{mv-dc1} are the maximum and minimum ST-1 MVDC voltages depending upon the direction of power transfer. For a power transfer of P^*_{dc-op} from ST-1 to ST-2, the ST-1 MVDC link voltage required to be higher than the ST-2 MVDC link. The ST-2 MVDC link is maintained at nominal value. The ST-1 MVDC link increases to V^o_{mv-dc1} as shown in Fig. 5.5. The ST-1 MV converter power reference P^*_{mv1} is used with instantaneous symmetrical component theory [71] to generate the corresponding current references (i^*_{mvabc1}). The currents are

given by

$$
\begin{aligned}
i^*_{mva1} &= \frac{v^p_{mva1} + k_{Q1}(v^p_{mvb1} - v^p_{mvc1})}{(v^p_{mva1})^2 + (v^p_{mvb1})^2 + (v^p_{mvc1})^2}(P^*_{mv1}) \\
i^*_{mvb1} &= \frac{v^p_{mvb1} + k_{Q1}(v^p_{mvc1} - v^p_{mva1})}{(v^p_{mva1})^2 + (v^p_{mvb1})^2 + (v^p_{mvc1})^2}(P^*_{mv1}) \\
i^*_{mvc1} &= \frac{v^p_{mvc1} + k_{Q1}(v^p_{mva1} - v^p_{mvb1})}{(v^p_{mva1})^2 + (v^p_{mvb1})^2 + (v^p_{mvc1})^2}(P^*_{mv1})
\end{aligned}
\tag{5.15}
$$

where v^p_{mva1}, v^p_{mvb1} and v^p_{mvc1}, respectively are fundamental positive sequence microgrid MVAC voltages of respective phases. k_{Q1} is the reactive power control constant. In this chapter reactive power exchange is not considered, and therefore k_{Q1} is zero. These reference currents are maintained using hysteresis based current controller to generate switching pulses.

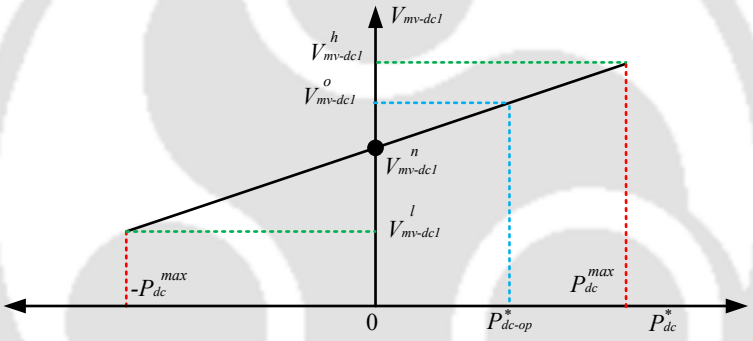

Fig. 5.5 ST-1 MVDC voltage variation with MVDC active power transfer.

5.3.2 ST-2 MV Converter Control

The ST-2 MV converter supplies the active power requirement at the LVAC bus. It also exchanges active power with main grid through MVDC distribution line. The control diagram is shown in Fig. 5.4(a) and (b). The ST-2 MV converter maintains the DC link voltage at nominal value. Depending upon the ST-1 MVDC voltage magnitude, the power is exchanged with the ST-1. The reference (V^*_{mv-dc2}) and measured (V_{mv-dc2}) ST-2 MVDC voltages are compared and the error is passed through a PI controller to generate the reference P^*_{loss}. This power reference along with ST-2 MV active power reference generated in (5.1) are used in instantaneous symmetrical component theory to

generate current references (i^*_{mvabc2}) as follows

$$
\begin{aligned}
i^*_{mva2} &= \frac{v^p_{mva2} + k_{Q2}(v^p_{mvb2} - v^p_{mvc2})}{(v^p_{mva2})^2 + (v^p_{mvb2})^2 + (v^p_{mvc2})^2}(P^*_{mv2} + P^*_{loss}) \\
i^*_{mvb2} &= \frac{v^p_{mvb2} + k_{Q2}(v^p_{mvc2} - v^p_{mva2})}{(v^p_{mva2})^2 + (v^p_{mvb2})^2 + (v^p_{mvc2})^2}(P^*_{mv2} + P^*_{loss}) \\
i^*_{mvc2} &= \frac{v^p_{mvc2} + k_{Q2}(v^p_{mva2} - v^p_{mvb2})}{(v^p_{mva2})^2 + (v^p_{mvb2})^2 + (v^p_{mvc2})^2}(P^*_{mv2} + P^*_{loss})
\end{aligned}
\tag{5.16}
$$

where v^p_{mva2}, v^p_{mvb2} and v^p_{mvc2}, respectively are fundamental positive sequence main grid MVAC voltages of respective phases. The reactive power control constant $k_{Q2} = 0$, since there is no reactive power transfer. The block-diagram representation of the reference current generation strategy is shown in Fig. 5.4(b). These reference currents are used with hysteresis current controller to generate converter switching pulses.

5.3.3 ST DC-DC Converter Control

For both ST-1 and ST-2, DC-DC converters are operated to transfer required power between MVDC and LVDC links. The control block-diagram is given in Fig. 5.4(c). The symbol 'i' indicates terms related to i^{th} ST (i =1, 2). The ST-1 and ST-2 DC-DC converters maintain a constant voltage at their respective DC links. A PI controller generates a phase angle reference (δ^*_{dc-dci}) from the error generated by the comparison of reference LVDC-i voltage (V^*_{lv-dci}) and corresponding measured value (V_{lv-dci}). Maintaining this phase angle difference between MVDC and LVDC side converter switches ensure the power flow and voltage control [59]. Detailed explanation of the control is given in Chapter 2.

5.3.4 ST LV Converter Control

The ST-1 and ST-2 LV converters are controlled in the similar fashion as a grid forming voltage source converter [9], [96]. A block-diagram is given in Fig. 5.4(d). The reference rms LV voltage (V^*_{lvi}) is maintained at 50 Hz frequency and 120° phase difference between phases. The reference three-phase voltages are maintained at the respective LVAC buses by the PWM controller. Detailed explanation of the control is given in Chapter 2.

Table 5.2 Simulation Parameters

System quantities	Values
ST MV converters	L_{mvi} = 100 mH
ST LV converters	L_{lvi} = 0.5 mH, C_{lvi} = 20 μF
DC link capacitors	C_{mv-dci} = 2000 μF, C_{lv-dci} = 2500 μF
ST DC-DC converters	L_{mvdc} = 10 mH, f_{sw} = 1 kHz
BESS DC-DC converter	L_b = 10 mH, f_{sw} = 1 kHz

5.3.5 BESS DC-DC Converter Control

The BESS control reference generation is shown in Fig. 5.4(a). During mode-1, the BESS charges from microgrid MVAC bus to maintain the necessary SOC. During peak load shaving operation, based on the availability of energy, the microgrid MVAC bus is supported from BESS. During reverse power flow control mode, as per requirement and availability, power is transferred from microgrid. In voltage sag operation, the BESS supports the ST-1 LVAC load as per the algorithm shown in Fig. 5.2. Based on the charging/discharging power reference (P_b^*) given in (5.3), (5.6) and (5.12), the controller generates the reference angle (δ_b^*) as shown in Fig. 5.4(e). This angle is maintained between ST-1 MVDC and BESS side converter switches which ensures the required power exchange between BESS and ST-1 MVDC link [125]. The BESS power transfer depends on the angle between BESS and ST-1 MVDC link side converter switches. The BESS power transfer reference (P_b^*) and reference angle (δ_b^*) is related as per

$$P_b^* = \frac{V_b V_{mv-dc1}}{2\pi f_{sw} L_b} \delta_b^* \left(1 - \frac{|\delta_b^*|}{\pi}\right) \tag{5.17}$$

where V_b is the voltage across the battery, f_{sw} is the switching frequency of the converter and L_b is the sum of isolation transformer leakage inductance and converter inductance [125].

5.4 SIMULATION RESULTS

The simulation analysis is carried out in PSCAD/EMTDC software and the parameters are shown in Table 5.1 and 5.2. Three cases are simulated in this chapter.

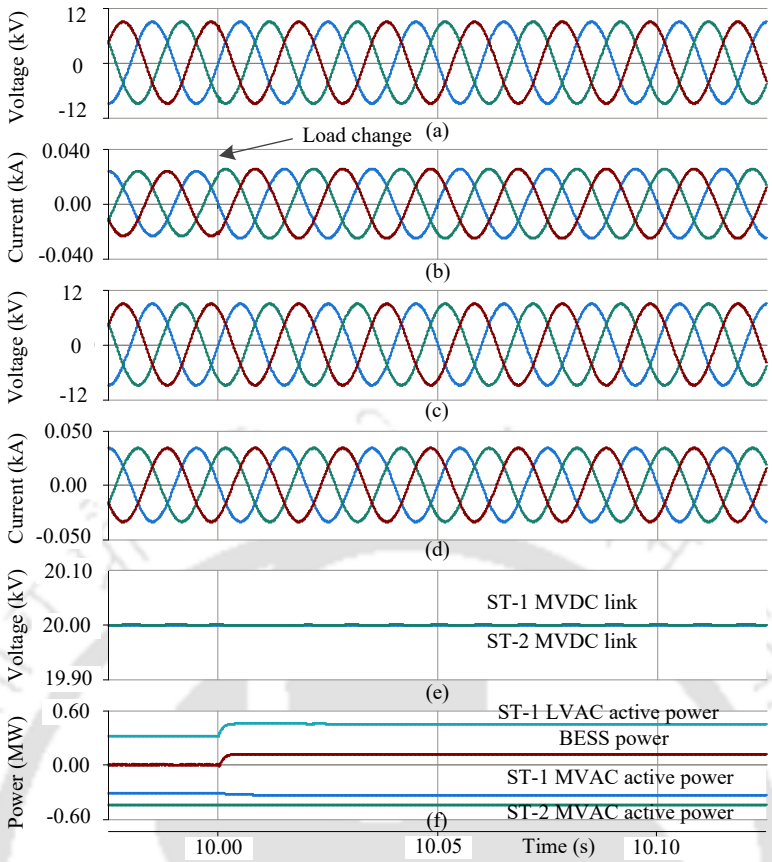

Fig. 5.6 Simulation results for peak load shaving operation. (a) Microgrid MVAC voltages. (b) ST-1 MV converter currents. (c) Main grid MVAC voltages. (d) ST-2 MV converter currents. (e) MVDC link voltages. (f) Different active powers.

5.4.1 Operation During Peak Load

Fig. 5.6 shows the operation with BESS support during peak loading on the microgrid. Till t = 10 s, the ST-1 and ST-2 MV converters supply their own LVAC loads. At t = 10 s, the loading on ST-1 LVAC bus is increased beyond the $P_{peak-lim}$. Fig. 5.6(a) and (c) show the microgrid and main grid MVAC voltages, respectively. Fig. 5.6(b) and (d) show the ST-1 MV and ST-2 MV converter currents. The BESS is available for discharge and it supports the ST-1 LVAC loads. Therefore, the loading on microgrid MVAC bus is not increased beyond a preset limit. The ST-1 and ST-2 MVDC voltages are shown in Fig. 5.6(e). As the power is not supplied from main grid through the MVDC line, the MVDC voltages remain at the nominal value. In Fig. 5.6(f), different active powers are shown. The ST-1 LVAC load power increase is visible from the Fig. 5.6(f). BESS power increases to supply a part of the load power. The ST-2 MVAC active power remain same throughout the operation.

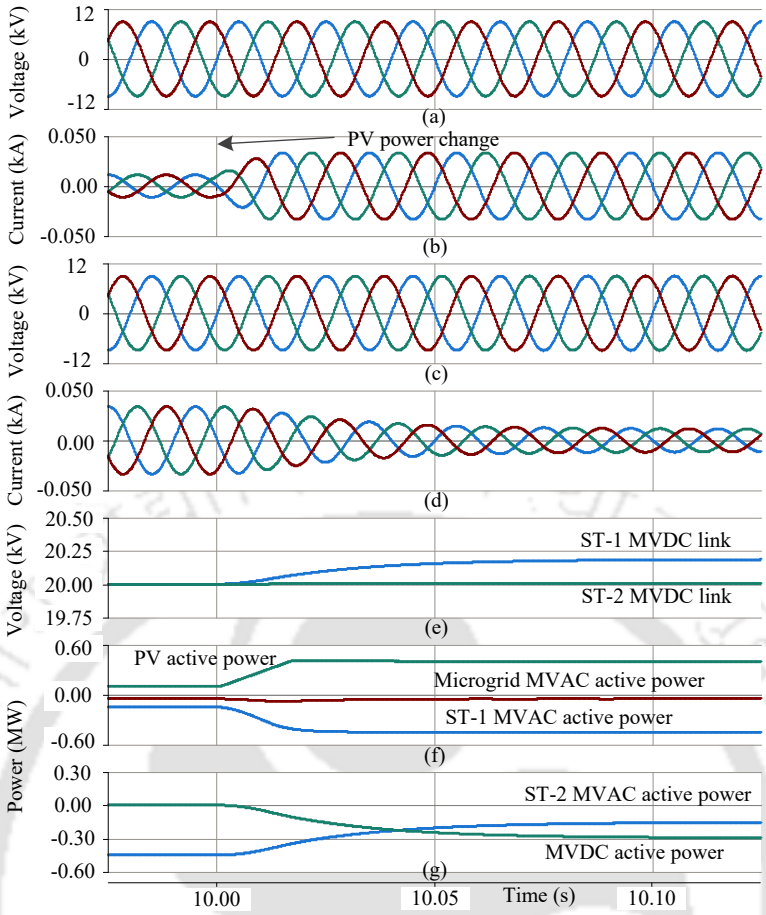

Fig. 5.7 Simulation results during reverse power flow control. (a) Microgrid MVAC voltages. (b) ST-1 MV converter currents. (c) Main grid MVAC voltages. (d) ST-2 MV converter currents. (e) MVDC link voltages. (f) PV, ST-1 MV converter and microgrid MVAC active powers. (g) ST-2 MV converter and MVDC active powers.

5.4.2 Operation During Peak PV Generation

In the second case shown in Fig. 5.7, the reverse power flow control operation is demonstrated. Till t = 10 s, the ST-1 and ST-2 MV converters supply their own LVAC loads. At t = 10 s, the PV output power increases. The ST-1 absorbs the active power from microgrid MVAC bus. As the BESS is not available in this condition, the active power from MVAC microgrid is transferred to the main grid through MVDC line. Fig. 5.7(a) and (c) show the microgrid and main grid MVAC voltages, respectively. The ST MV converter currents are shown in Fig. 5.7(b) and (d) for ST-1 and ST-2, respectively. The ST-1 MV converter currents increase due to extra power absorption. Fig. 5.7(e) shows MVDC link voltages of ST-1 and ST-2. The ST-1 MVDC link voltage increases above nominal value to control the power transfer. Fig. 5.7(f) shows PV, ST-1 MV and microgrid MVAC active powers. The microgrid MVAC active power remains nearly

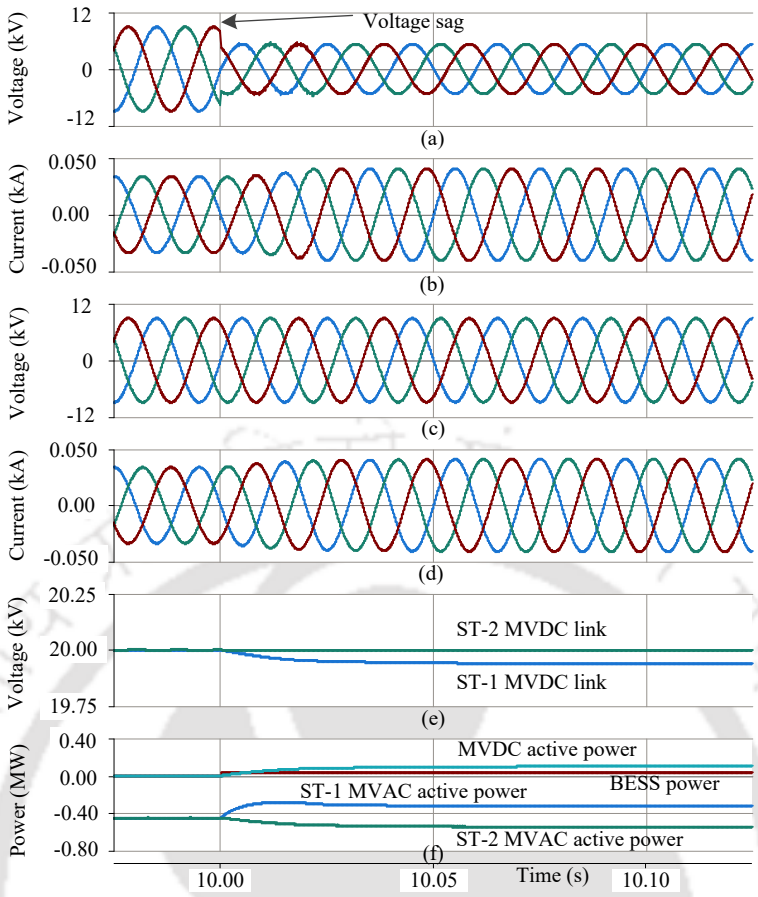

Fig. 5.8 Simulation results during microgrid MVAC voltage sag. (a) Microgrid MVAC voltages. (b) ST-1 MV converter currents. (c) Main grid MVAC voltages. (d) ST-2 MV converter currents. (e) MVDC link voltages. (f) Different active powers.

constant due to the increased absorption by ST-1 MV converter thereby avoiding reverse power flow. Fig. 5.7(g) shows the ST-2 MVAC and MVDC active powers. The ST-2 MVAC active power reduces due to the active power transfer through MVDC link from microgrid.

5.4.3 Operation During Microgrid MVAC Voltage Sag

In the third case shown in Fig. 5.8, the voltage sag operation is analyzed. Till t = 10 s, the ST-1 and ST-2 LVAC loads are supplied from the respective MV converters. Fig. 5.8(a) and (c) show the microgrid and main grid MVAC voltages, respectively. The microgrid MVAC voltages decrease after experiencing a 40% sag at t = 10 s. The ST MV converter currents are shown in Fig. 5.8(b) and (d) for ST-1 and ST-2. The ST-1 MV converter currents increase to the maximum rating. Fig. 5.8(e) shows MVDC link voltages of ST-1 and ST-2. The ST-1 MVDC link voltage decreases to transfer the

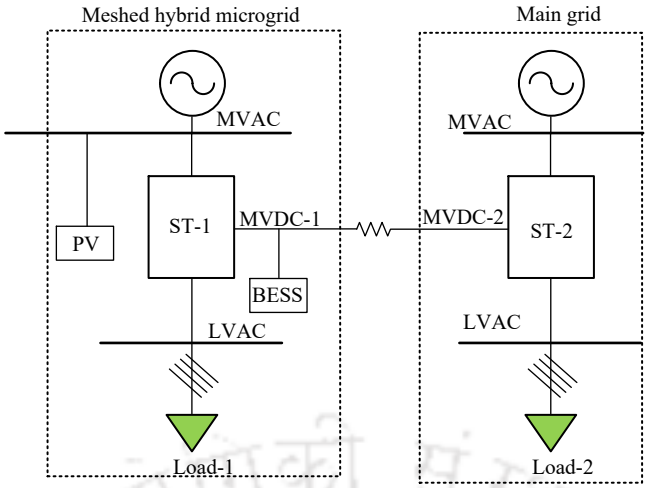

Fig. 5.9 Experimental setup schematic.

Table 5.3 Experimental Parameters

System quantities	Values
MVAC grid voltage	150 V
LVAC grid voltage	110 V
ST MV converters	L_{mv} = 13 mH
ST LV converters	L_{lv} = 5 mH, C_{lv} = 10 μF
DC link voltage	V_{dc} = 275 V

demanded power from main grid. Fig. 5.8(f) shows different active powers. The ST-1 and ST-2 MV converter active powers are shown. The active power is transferred from the main grid. Since it reaches the maximum transferable power, BESS is also activated to supply the remaining power. The ST-1 MVAC active power reduces to maintain the currents within the maximum rating. The ST-2 MVAC active power increases after the voltage sag to support ST-1 LVAC loads.

5.5 EXPERIMENTAL RESULTS

Fig. 5.9 shows the schematic diagram of the experimental prototype. The experimental parameters are shown in Table 5.3. The experiment analysis shows all the cases described in the simulation analysis.

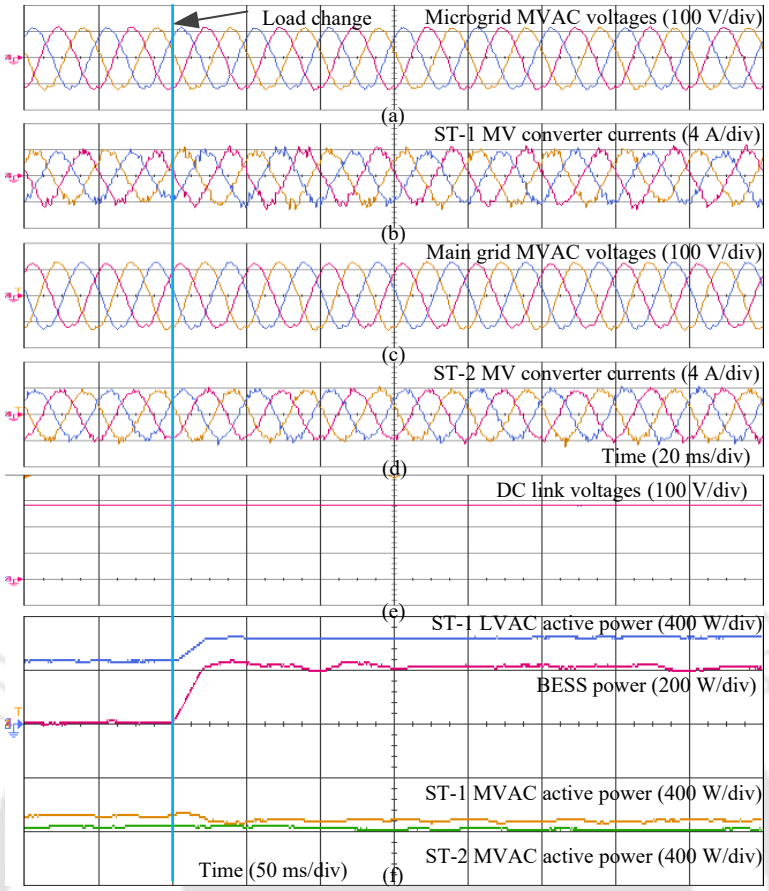

Fig. 5.10 Experimental results for peak load shaving operation. (a) Microgrid MVAC voltages. (b) ST-1 MV converter currents. (c) Main grid MVAC voltages. (d) ST-2 MV converter currents. (e) MVDC link voltages. (f) Different active powers.

5.5.1 Operation During Peak Load

In the first case, the peak load operation is analyzed. Fig. 5.10 shows the results for the peak load operation. The ST-1 and ST-2 operate to supply their own LVAC loads. The ST-1 LVAC load is increased beyond the predefined peak load limit, and the BESS supports the ST-1 LVAC loads. Fig. 5.10(a) and (c) show the three-phase voltages of microgrid and main grid MVAC bus, respectively. Fig. 5.10(b) and (d) show the MVAC currents for ST-1 and ST-2, respectively. The load change is marked in the Fig. 5.10, and DC link voltages are shown in Fig. 5.10(e). Different powers are shown in Fig. 5.10(f). The ST-1 LVAC load power increase is visible from the Fig. 5.10(f). The load increase is not reflected on the ST-1 MV active power, and this shows that the BESS power support lowers the peak demand on microgrid MVAC bus. This smooths the load curve.

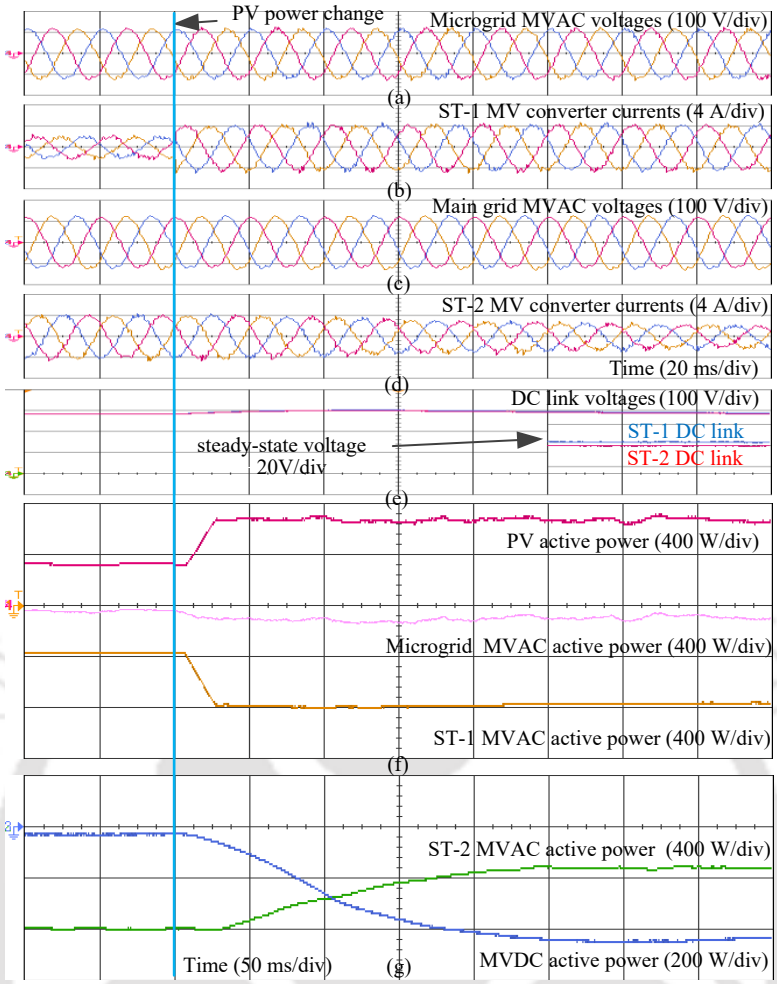

Fig. 5.11 Experimental results during reverse power flow control. (a) Microgrid MVAC voltages. (b) ST-1 MV converter currents. (c) Main grid MVAC voltages. (d) ST-2 MV converter currents. (e) MVDC link voltages. (f) PV, ST-1 MV converter and microgrid MVAC active powers. (g) ST-2 MV converter and MVDC active powers.

5.5.2 Operation During Peak PV Generation

In the second case, PV injection increase scenario is considered to show the reverse power flow case. Fig. 5.11 shows different waveforms. Fig. 5.11(a) and (c) show MVAC voltages for microgrid and main grid, respectively. The ST-1 MVAC currents increase after the absorption of extra active power from PV source, and it is shown in Fig. 5.11(b). The ST-2 MVAC currents decrease due to extra active power support from MVDC line as shown in Fig. 5.11(d). The DC link voltages are shown in Fig. 5.11(e). The ST-1 MVDC link voltage increases to facilitate the active power transfer. Fig. 5.11(f) shows PV, ST-1 MV converter and microgrid MVAC active powers. The microgrid MVAC active power remains nearly constant even after the PV active power increase. The ST-1 MV active power increases to absorb extra power from microgrid.

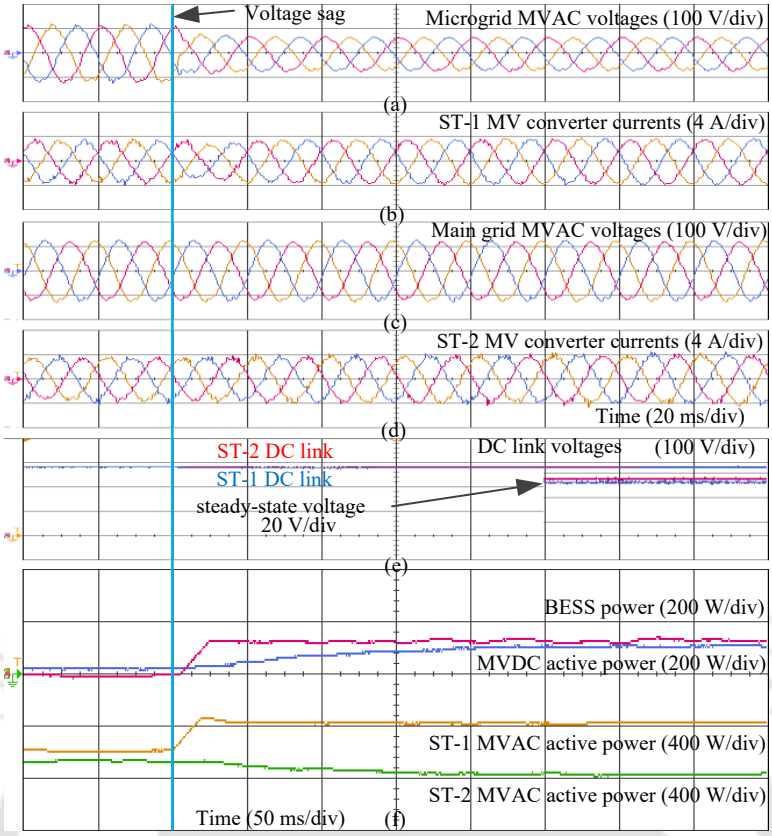

Fig. 5.12 Experimental results during microgrid MVAC voltage sag. (a) Microgrid MVAC voltages. (b) ST-1 MV converter currents. (c) Main grid MVAC voltages. (d) ST-2 MV converter currents. (e) MVDC link voltages. (f) Different active powers.

Fig. 5.11(g) shows the ST-2 MVAC and MVDC line active powers. The reverse power control capability shows the ability of the system to reduce the voltage rise conditions.

5.5.3 Operation During Microgrid MVAC Voltage Sag

In the third case, the microgrid MVAC bus experiences a voltage sag and ST-1 active power is supported by the ST-2 and BESS. Till the sag, the ST-1 and ST-2 LVAC loads are supplied from the respective MV converters. Fig. 5.12(a) shows the microgrid MVAC voltages and the voltage sag is visible in the waveform. Fig. 5.12(b) shows the ST-1 MVAC currents. Fig. 5.12(c) shows the main grid MVAC voltages and Fig. 5.12(d) shows ST-2 MVAC currents. The DC link voltages are shown in Fig. 5.12(e). The ST-1 MVDC link voltage decreases to import active power through MVDC line. Different active powers are shown in Fig. 5.12(f). The MVDC line active power increases due to the power transfer from main grid. The BESS supports the remaining load of ST-1 LVAC bus. The ST-1 MV converter active power reduces to limit the

converter currents within the rating. The ST-2 MV converter active power increases to transfer the power demand from ST-1. The uninterrupted operation during voltage sag improves the overall reliability of the system.

5.6 CONCLUSIONS

This chapter proposes operation of an MVDC interconnected meshed hybrid microgrid configuration enabled by ST and BESS during adverse grid conditions. The following advantages are achieved: (1) lower peak power demand from MVAC grid smooths the load curve and reduces the unmanageable high-load conditions on the grid, (2) reverse power flow control reduces the voltage rise conditions without the PV active power curtailment, and this helps in maximizing the energy extraction from PV sources, and (3) continuous operation of loads during grid voltage sags are helpful in reducing power interruption-hours in the system and this improves the reliability of power supply to the customers. The simulation and experimental results verify the findings.

CHAPTER 6

CONCLUSIONS

6.1 SUMMARY

With integration of more renewable energy sources (RESs) and electric vehicles (EVs), the power system is under major transformation. Due to this change, different new challenges also need to be addressed for maintaining continuous and stable operation of the power system. Voltage magnitude variations, limited hosting capability of power distribution systems, operation and management of islanded and grid-connected micro-grids, intermittent power production from RESs, etc. are considered to be major issues that need immediate attention. Some of the available solutions for addressing these challenges are: on-load tap changers (OLTCs), improved control of distributed generation (DG) operation, AC/DC hybrid distribution grids, custom power devices, etc. The operating range of OLTC is limited, and the integration of additional control with DG increases its complexity. The operational freedom of custom power devices is limited depending upon the nature of grid impedance. For coordinating and addressing various challenges, the need for a central controller is identified by the researchers due to the limitations of these existing solutions.

In this scenario, a solid-state transformer (SST) is proposed, which is a power electronic-based transformer. The SST with the necessary control and communication features is termed as a smart transformer (ST). The ST has the potential to feature as a central controller in the electric distribution grids. A three-stage ST has emerged as a suitable candidate in distribution grid that has DC-link availability at low voltage (LV) and medium voltage (MV) levels. It consists of a three-phase AC-DC converter as the first stage, a DC-DC converter with high-frequency isolation transformer as the second stage, and a three-phase DC-AC converter as the third stage. In addition to the isolation and voltage transformation operation similar to conventional power transformer (CPT), the basic ST operation can perform unity power factor current absorption at the MVAC grid irrespective of the LVAC load. It also maintains a three-phase balanced sinusoidal

voltage at the LVAC side irrespective of the MVAC grid condition. More importantly, CPT is a high efficient, cost-effective solution. Therefore, replacement of CPT with ST can only be justified with the additional features it can offer to the distribution system.

This thesis has explored the capabilities of ST in a distribution grid. The reactive power injection capability is vital in a distribution grid during voltage variations. The ST MV converter has the capability to exchange reactive power with the MVAC distribution grid. A method is proposed to improve the reactive power injection capability of ST MV converter with the help of ST LV converter and battery energy storage system (BESS). The load control features of ST LV converter is used during MVAC grid voltage sag/swell to reduce the active power loading on ST MV converter. The proposed method achieves the required voltage support with the help of a reduced rated BESS.

The ST integrated BESS is capable of exchanging active and reactive powers with the grid. A sensitivity-based converter sizing study is proposed for improving the load and generation hosting capability using ST integrated with the BESS. The proposed method is validated in a 5-bus radial feeder with comparable resistance and reactance values. This method can flexibly inject active and reactive powers independently or a combination of both. Therefore, the method can be applied to AC distribution grids irrespective of the grid parameters.

The AC-DC hybrid grids are getting importance due to their capability to integrate sources and loads both at AC and DC voltage levels. The MVDC based distribution grids are gaining momentum to solve many issues related to the interconnection of microgrids. The ST MVDC links are used to establish a meshed hybrid microgrid configuration. A renewable-rich microgrid is integrated to the main grid through the MVDC links of ST and different operating scenarios are analyzed. The ST MV converter and grid failure conditions are analyzed to verify the reliability of distribution system. The flexibility for power management in the proposed microgrid reduces the DG re-synchronization requirements during the failure of MVAC feeder. Moreover, this system offers a higher reactive power capability at the MVAC bus and lower line active power loss for inter-grid active power transfer.

In the presence of PV and BESS, the ST based meshed hybrid configuration is also analyzed for its operation during adverse grid conditions. The peak load shaving, reverse power flow control, and voltage sag operations are tested in the configuration. The peak

load shaving operation is achieved with the power management strategy, and this helps in reducing the spikes in the load curve. The reverse power flow control during high generation time reduces the voltage rise phenomenon in the MVAC distribution grid. Moreover, the operation during an MVAC microgrid voltage sag shows the capability of the proposed system to continue the power supply to LVAC loads even during deep MVAC grid voltage sags. This improves the reliability of the power supply for the LVAC loads.

The simulation study is conducted for different cases in PSCAD/EMTDC software. An experimental setup is developed in the laboratory to validate the major theoretical findings in the real-time hardware prototype. The major contributions of this thesis are:

- A control scheme is proposed for the coordinated operation of ST MV converter, ST LV converter, and BESS during MVAC grid voltage sag and swell. This strategy improves the voltage support capability of ST in MVAC grid with a reduced rated BESS.
- A converter sizing method is proposed for BESS integrated ST for improving the load and generation hosting capability of a radial MVAC distribution system.
- An ST based meshed hybrid microgrid is proposed with MVDC interconnection, and the operation is analyzed during MV converter and grid failure conditions. Moreover, the system performance is compared with existing solutions for bringing out the advantages.
- The meshed hybrid microgrid operation is analyzed during various adverse conditions such as high PV generation, peak load, and voltage sag. The ST with BESS improves the performance of the system during these adverse grid conditions.
- An experimental prototype is developed in the laboratory. All the proposed methods are validated in both simulation and experimental environments.

6.2 SCOPE FOR FUTURE WORK

This thesis utilized the ST's capability for voltage support and hosting capability improvement with the integration of BESS to the LVDC link. In addition, the ST MVDC

links are used for establishing MVDC feeder and meshed hybrid microgrid. However, the RES integration is not realized with the MVDC link. The integration of RES to the MVDC link of ST can be an option to improve the performance of MVAC grid.

In this thesis, all the configurations replaces the CPT with ST. The integration of ST in parallel to the existing CPT can improve the operation of CPT. This hybrid configuration can reduce the rating of ST required for applications such as reactive and harmonic compensation features in the distribution grid. It can also improve the control of active, reactive and harmonic powers through the CPT, and thereby the efficiency-optimized operation of CPT can be realized. The BESS integrated to the LVDC link of ST further introduces extra options for the power management in LVAC microgrid.

The integration of EV charging stations to the ST DC links is an opportunity to address many challenges associated with the EV integration. The charging stations can be integrated to both MVDC and LVDC links of ST based on their operating power level. The ST can flexibly control the active and reactive powers from the different grids integrated with the ST MV and ST LV converters. This can avoid the problems with the extra charging power extraction from the heavily loaded grids.

APPENDIX A

EXPERIMENTAL SETUP DETAILS

The smart transformer (ST) implementation in laboratory environment requires multiple components. The power electronic converters and the control mechanisms are two of the major components. The power electronic converters are realized using SEMIKRON-make IGBT stack modules. The control mechanism is through a MicroLabBox controller. The different components of the developed experimental prototype are explained as follows.

A.1 EXPERIMENTAL SETUP

The experimental setup block-diagram is shown in Fig. A.1. The actual voltages and currents from the distribution system are converted to low-level voltage signals using Hall effect current and voltage transducers. These signals are used in the control algorithm embedded in MicroLabBox controller. The switching pulses generated from the MicroLabBox is given to the level-shifter circuit, and the output gate pulses are provided to the power electronic converters. The power electronic converters are connected to the distribution system through appropriate filters. Details of the system components are given in the following sub-section.

A.1.1 Power Distribution System

In the experimental setup, a three-phase AC power distribution system is considered. The actual voltage levels are stepped-down using autotransformer to realize MVAC voltage levels. The LVAC grid consists of loads that are realized using diode bridge rectifier (for nonlinear loads) and resistive load bank. The DC grid measuring quantities are also considered for the control input. Fig. A.2 shows the MVAC grid photograph realized using autotransformers and line impedance. Fig. A.3 shows the photograph of LVAC loads.

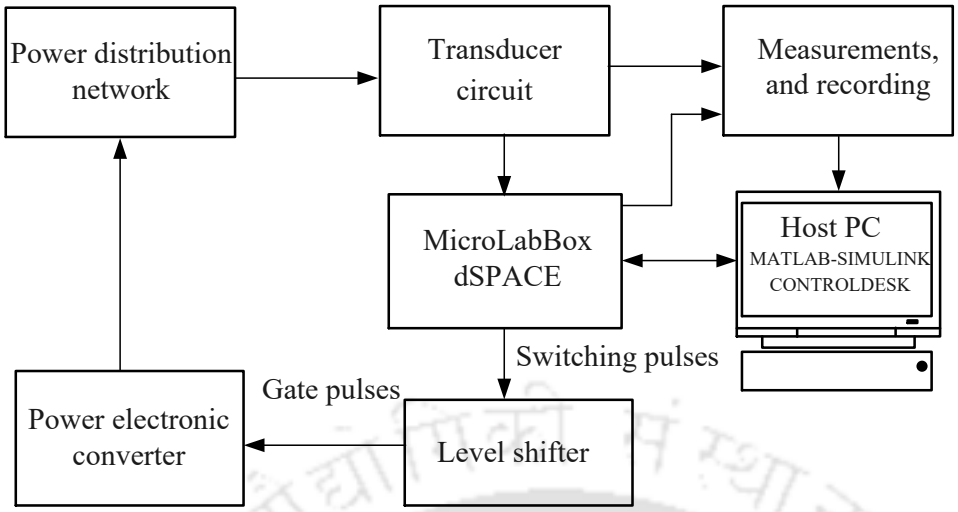

Fig. A.1 Block-diagram of the experimental prototype developed.

A.1.2 Power Electronic Converters

In this study, the SEMIKRON-make voltage source converters are used to realize the ST converters. The ST MV converter is connected between the MVAC grid and the DC line. The ST LV converter is connected to the LVAC grid. The BESS is realized using an AC/DC converter, and the DG source is realized using a DC/AC converter with a constant DC source at the DC terminal. The converter drivers are supplied with + 15 V through switched-mode power supply (SMPS) based 15 V, 5 A, power supply. The overall experimental setup photograph is shown in Fig. A.4. The photograph of the DC source used to realize DG source is shown in Fig. A.5.

A.1.3 Transducer Circuit

The current transducers (LA 55-P) and the voltage transducers (LV 25-P) are used to convert the actual circuit currents and voltages to its low power equivalent for making it compatible with the MicroLabBox controller circuit. A 32 V, 2 A regulated DC power supply is used for the generation of ± 15 V power supply required for the transducer circuits. The actual voltage and current signals are converted to ± 5 V voltage signals by the transducers as the MicroLabBox controller is not capable of handling the actual voltage levels. Fig. A.6(a) and (b) show the photographs of voltage and current transducer circuits, respectively.

A.1.4 MicroLabBox Controller

MicroLabBox is a user-programmable FPGA based controller with more than 100 channels for input/output (I/O). This is supported by a dSPACE software package for Simulink, which enables model-based I/O integration. This controller has eight numbers of 14-bit analogue to digital converter (ADC) channels and 24 numbers of 16-bit ADC channels for different signal inputs. It has 16 numbers of 16-bit digital to analogue converter (DAC) for measurement and control purposes. It has 60 digital I/O channels, which provide flexibility for the switching pulse generation. One of the advantages of the dSPACE based controller is that its ADC pins can be connected with the $\pm$ 10 V supply and this avoids the extra signal conditioning circuit between transducer and controller. A photograph is given in Fig. A.7.

A.1.5 Host Computer

The MicroLabBox is connected to a host computer for realizing the required control algorithms in MATLAB-Simulink environment. The ControlDesk is a controlling platform for MicroLabBox, where the real time control can also be implemented. For any testing, the power electronic converters are protected through the logic circuit designed in MATLAB-Simulink model for over-current, over-voltage, and higher DC-link voltage. Fig. A.8 shows the photograph.

A.1.6 Measurements and Recording

The measurement and display of different quantities are important for ensuring the operation of the control algorithm. Multiple digital storage oscilloscopes (DSOs) are used for this purpose. In Fig. A.8, different measuring and recording instruments used are shown.

A.1.7 Level Shifter Circuit

The dedicated digital I/O pins of MicroLabBox can be configured with different voltage levels (2.5 V/3.3 V/5 V). However the power electronic converter drivers require 15

V voltage level gate pulses. The switching pulses generated from MicroLabBox are boosted to 15 V DC level using a level shifter CD4504 circuit and supplied to the power electronic converter driver circuits. The level shifter circuit is shown in Fig. A.9.

A.2 PHOTOGRAPHS OF THE SETUP

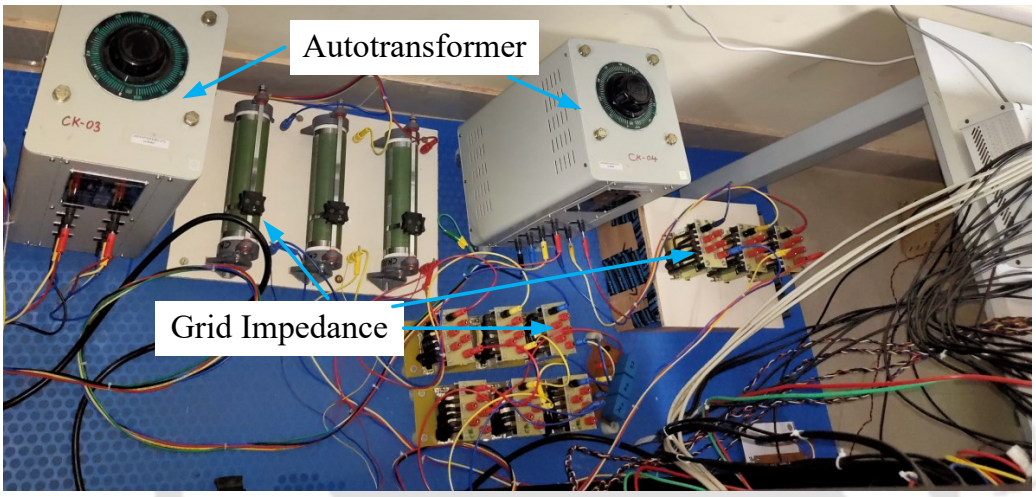

Fig. A.2 MVAC grid realization with autotransformers and line impedance.

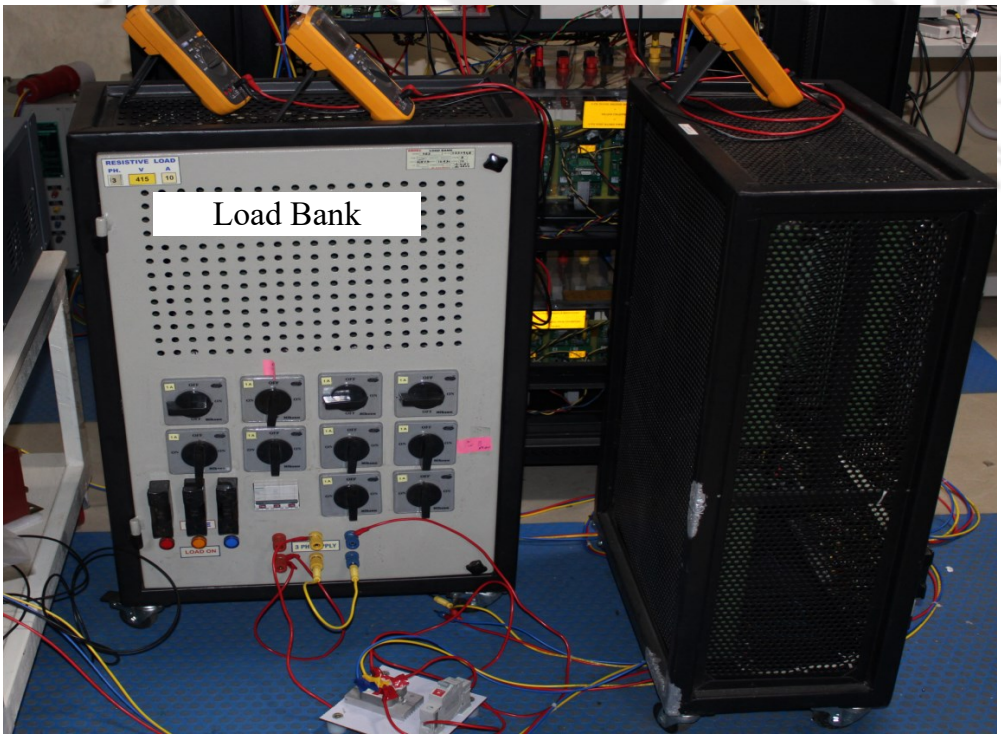

Fig. A.3 LVAC loads (linear and nonlinear).

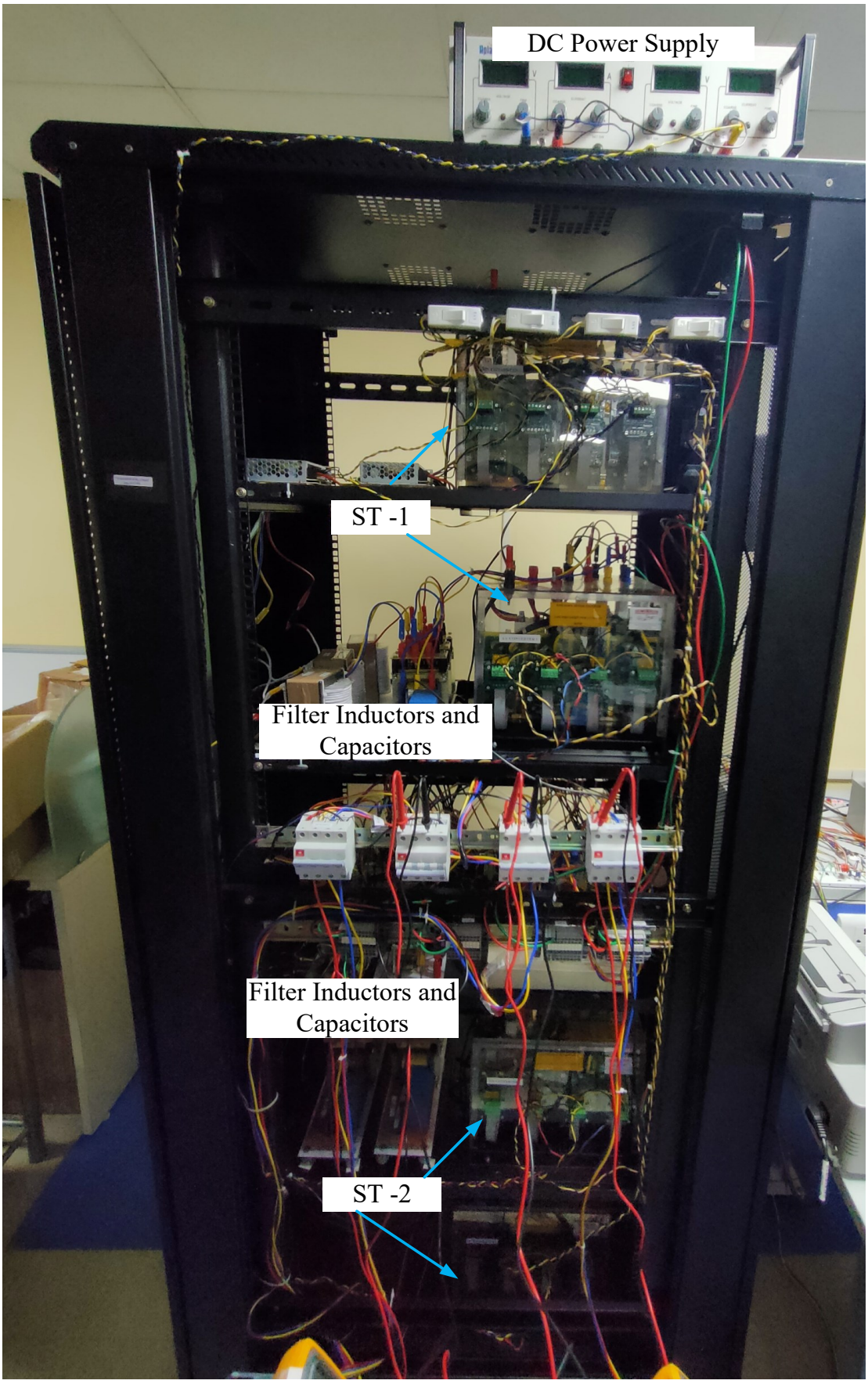

Fig. A.4 Overall experimental setup with power electronic converters.

Fig. A.5 High voltage DC power source used to realize DG.

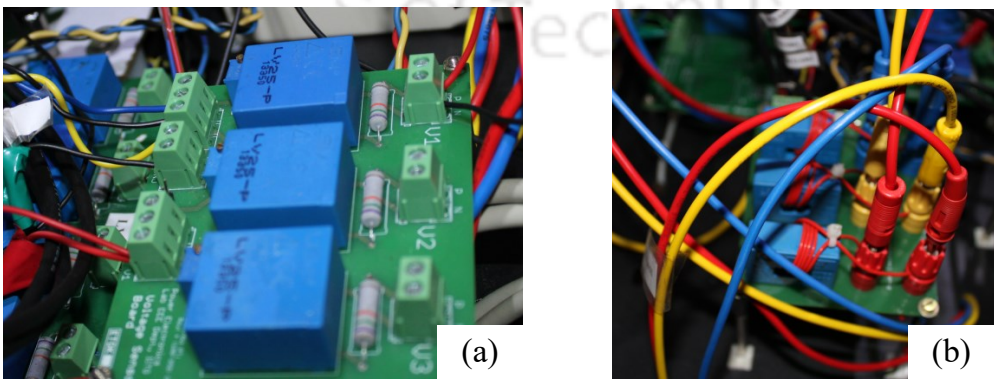

Fig. A.6 Transducer circuits. (a) Voltage transducers. (b) Current transducers.

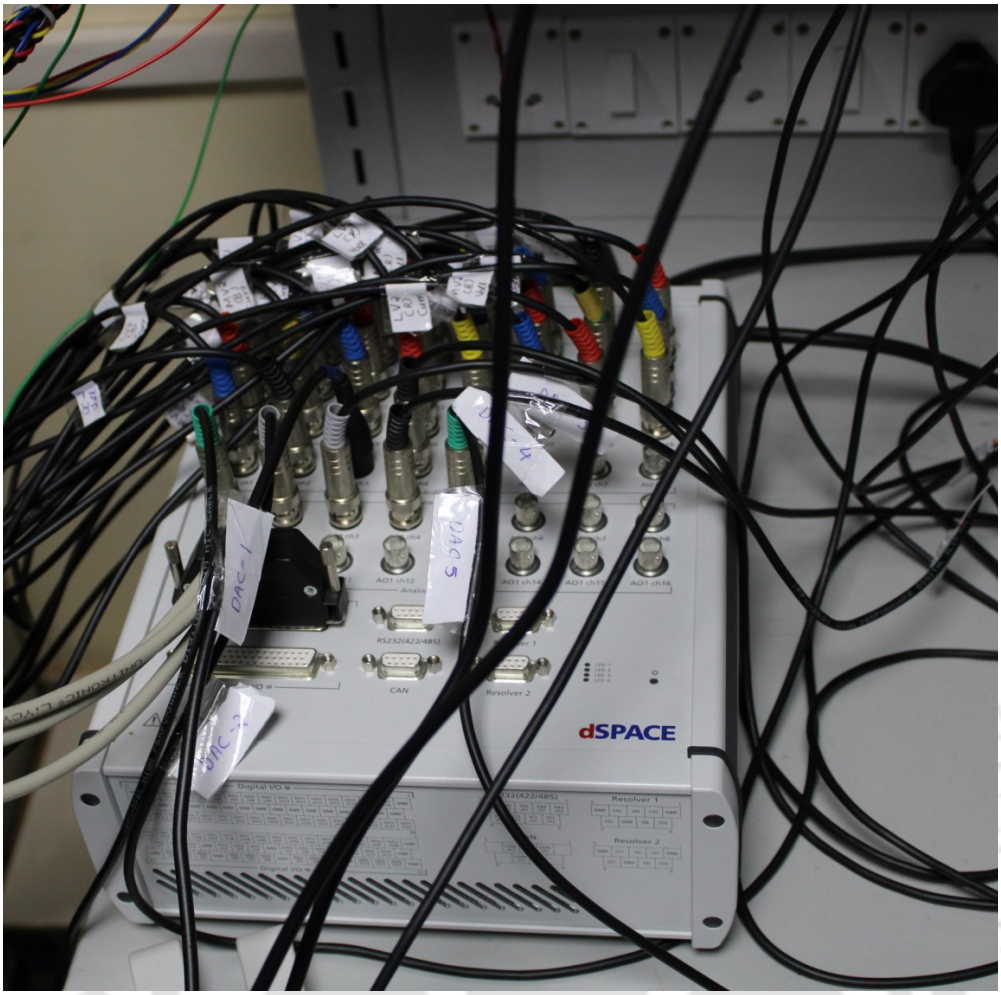

Fig. A.7 MicroLabBox with ADC and DAC connections.

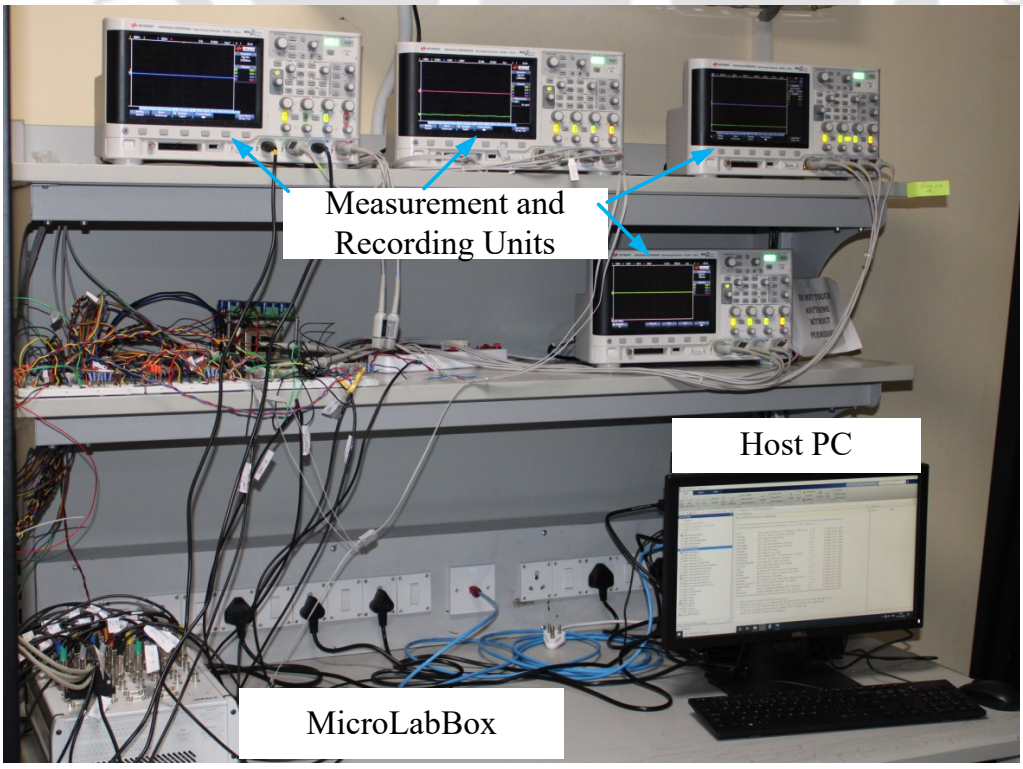

Fig. A.8 Host PC, measuring and recording units.

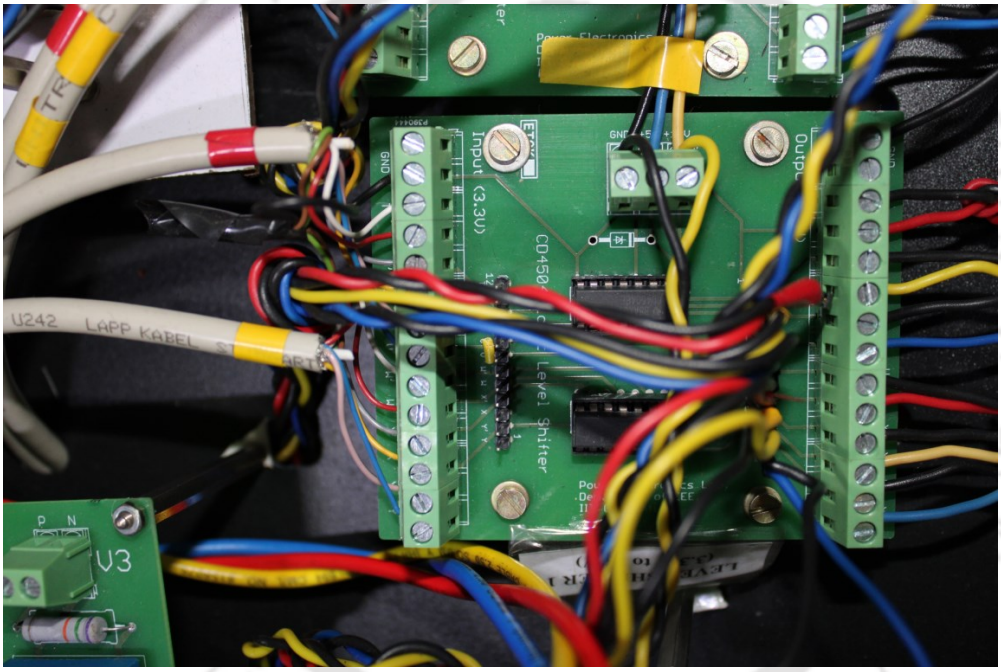

Fig. A.9 Level shifter circuit.

REFERENCES

[1] R. A. Walling, R. Saint, R. C. Dugan, J. Burke, and L. A. Kojovic, "Summary of distributed resources impact on power delivery systems," *IEEE Transactions on Power Delivery*, vol. 23, no. 3, pp. 1636–1644, July 2008.

[2] F. Blaabjerg, Y. Yang, D. Yang, and X. Wang, "Distributed power-generation systems and protection," *Proceedings of the IEEE*, vol. 105, no. 7, pp. 1311–1331, July 2017.

[3] P. N. Vovos, A. E. Kiprakis, A. R. Wallace, and G. P. Harrison, "Centralized and distributed voltage control: Impact on distributed generation penetration," *IEEE Transactions on Power Systems*, vol. 22, no. 1, pp. 476–483, Feb. 2007.

[4] F. Blaabjerg, R. Teodorescu, M. Liserre, and A. V. Timbus, "Overview of control and grid synchronization for distributed power generation systems," *IEEE Transactions on Industrial Electronics*, vol. 53, no. 5, pp. 1398–1409, Oct. 2006.

[5] J. M. Guerrero, J. C. Vasquez, J. Matas, L. G. de Vicuna, and M. Castilla, "Hierarchical control of droop-controlled ac and dc microgrids-a general approach toward standardization," *IEEE Transactions on Industrial Electronics*, vol. 58, no. 1, pp. 158–172, Jan. 2011.

[6] C. A. Hill, M. C. Such, D. Chen, J. Gonzalez, and W. M. Grady, "Battery energy storage for enabling integration of distributed solar power generation," *IEEE Transactions on Smart Grid*, vol. 3, no. 2, pp. 850–857, June 2012.

[7] J. A. P. Lopes, F. J. Soares, and P. M. R. Almeida, "Integration of electric vehicles in the electric power system," *Proceedings of the IEEE*, vol. 99, no. 1, pp. 168–183, Jan. 2011.

[8] S. Parhizi, H. Lotfi, A. Khodaei, and S. Bahramirad, "State of the art in research on microgrids: A review," *IEEE Access*, vol. 3, pp. 890–925, 2015.

[9] J. Rocabert, A. Luna, F. Blaabjerg, and P. Rodriguez, "Control of power converters in ac microgrids," *IEEE Transactions on Power Electronics*, vol. 27, no. 11, pp. 4734–4749, Nov. 2012.

[10] M. R. Alam, K. M. Muttaqi, and A. Bouzerdoum, "Characterizing voltage sags and swells using three-phase voltage ellipse parameters," *IEEE Transactions on Industry Applications*, vol. 51, no. 4, pp. 2780–2790, July 2015.

[11] N. Jayasekara, M. A. S. Masoum, and P. J. Wolfs, "Optimal operation of distributed energy storage systems to improve distribution network load and generation hosting capability," *IEEE Transactions on Sustainable Energy*, vol. 7, no. 1, pp. 250–261, Jan. 2016.

[12] I. J. Balaguer, Q. Lei, S. Yang, U. Supatti, and F. Z. Peng, "Control for grid-connected and intentional islanding operations of distributed power generation," *IEEE Transactions on Industrial Electronics*, vol. 58, no. 1, pp. 147–157, Jan 2011.

[13] F. C. L. Trindade, T. S. D. Ferreira, M. G. Lopes, and W. Freitas, "Mitigation of fast voltage variations during cloud transients in distribution systems with pv solar farms," *IEEE Transactions on Power Delivery*, vol. 32, no. 2, pp. 921–932, Apr. 2017.

[14] K. Qian, C. Zhou, M. Allan, and Y. Yuan, "Modeling of load demand due to ev battery charging in distribution systems," *IEEE Transactions on Power Systems*, vol. 26, no. 2, pp. 802–810, May 2011.

[15] T. Ghanbari and E. Farjah, "Development of an efficient solid-state fault current limiter for microgrid," *IEEE Transactions on Power Delivery*, vol. 27, no. 4, pp. 1829–1834, Oct. 2012.

[16] V. F. Corasaniti, M. B. Barbieri, P. L. Arnera, and M. I. Valla, "Hybrid active filter for reactive and harmonics compensation in a distribution network," *IEEE Transactions on Industrial Electronics*, vol. 56, no. 3, pp. 670–677, Mar. 2009.

[17] J. C. Gomez and M. M. Morcos, "Impact of ev battery chargers on the power quality of distribution systems," *IEEE Transactions on Power Delivery*, vol. 18, no. 3, pp. 975–981, July 2003.

[18] C. L. Masters, "Voltage rise: the big issue when connecting embedded generation to long 11 kv overhead lines," *Power Engineering Journal*, vol. 16, no. 1, pp. 5–12, Feb. 2002.

[19] X. Liang, "Emerging power quality challenges due to integration of renewable energy sources," *IEEE Transactions on Industry Applications*, vol. 53, no. 2, pp. 855–866, Mar. 2017.

[20] R. Tonkoski, D. Turcotte, and T. H. M. EL-Fouly, "Impact of high pv penetration on voltage profiles in residential neighborhoods," *IEEE Transactions on Sustainable Energy*, vol. 3, no. 3, pp. 518–527, July 2012.

[21] M. Hasheminamin, V. G. Agelidis, V. Salehi, R. Teodorescu, and B. Hredzak, "Index-based assessment of voltage rise and reverse power flow phenomena in a distribution feeder under high pv penetration," *IEEE Journal of Photovoltaics*, vol. 5, no. 4, pp. 1158–1168, July 2015.

[22] M. F. McGranaghan, D. R. Mueller, and M. J. Samotyj, "Voltage sags in industrial systems," *IEEE Transactions on Industry Applications*, vol. 29, no. 2, pp. 397–403, Mar. 1993.

[23] P. Rodriguez, A. V. Timbus, R. Teodorescu, M. Liserre, and F. Blaabjerg, "Flexible active power control of distributed power generation systems during grid faults," *IEEE Transactions on Industrial Electronics*, vol. 54, no. 5, pp. 2583–2592, Oct. 2007.

[24] S. Alepuz, S. Busquets-Monge, J. Bordonau, J. A. Martinez-Velasco, C. A. Silva, J. Pontt, and J. Rodriguez, "Control strategies based on symmetrical components for grid-connected converters under voltage dips," *IEEE Transactions on Industrial Electronics*, vol. 56, no. 6, pp. 2162–2173, June 2009.

[25] L. Yang, Z. Xu, J. Ostergaard, Z. Y. Dong, and K. P. Wong, "Advanced control strategy of dfig wind turbines for power system fault ride through," *IEEE Transactions on Power Systems*, vol. 27, no. 2, pp. 713–722, May 2012.

[26] A. Dubey and S. Santoso, "Electric vehicle charging on residential distribution systems: Impacts and mitigations," *IEEE Access*, vol. 3, pp. 1871–1893, 2015.

[27] K. Clement-Nyns, E. Haesen, and J. Driesen, "The impact of charging plug-in hybrid electric vehicles on a residential distribution grid," *IEEE Transactions on Power Systems*, vol. 25, no. 1, pp. 371–380, Feb. 2010.

[28] S. Deilami, A. S. Masoum, P. S. Moses, and M. A. S. Masoum, "Real-time coordination of plug-in electric vehicle charging in smart grids to minimize power losses and improve voltage profile," *IEEE Transactions on Smart Grid*, vol. 2, no. 3, pp. 456–467, Sep. 2011.

[29] F. Ding and B. Mather, "On distributed pv hosting capacity estimation, sensitivity study, and improvement," *IEEE Transactions on Sustainable Energy*, vol. 8, no. 3, pp. 1010–1020, July 2017.

[30] A. Dubey and S. Santoso, "On estimation and sensitivity analysis of distribution circuit's photovoltaic hosting capacity," *IEEE Transactions on Power Systems*, vol. 32, no. 4, pp. 2779–2789, July 2017.

[31] A. G. Boulanger, A. C. Chu, S. Maxx, and D. L. Waltz, "Vehicle electrification: Status and issues," *Proceedings of the IEEE*, vol. 99, no. 6, pp. 1116–1138, June 2011.

[32] M. Yilmaz and P. T. Krein, "Review of the impact of vehicle-to-grid technologies on distribution systems and utility interfaces," *IEEE Transactions on Power Electronics*, vol. 28, no. 12, pp. 5673–5689, Dec. 2013.

[33] O. Sundstrom and C. Binding, "Flexible charging optimization for electric vehicles considering distribution grid constraints," *IEEE Transactions on Smart Grid*, vol. 3, no. 1, pp. 26–37, Mar. 2012.

[34] V. Levi, M. Kay, and I. Povey, "Reverse power flow capability of tap-changers," in *CIRED 2005 - 18th International Conference and Exhibition on Electricity Distribution*, June 2005, pp. 1–5.

[35] L. M. Cipcigan and P. C. Taylor, "Investigation of the reverse power flow requirements of high penetrations of small-scale embedded generation," *IET Renewable Power Generation*, vol. 1, no. 3, pp. 160–166, Sep. 2007.

[36] S. Munir and Y. W. Li, "Residential distribution system harmonic compensation using pv interfacing inverter," *IEEE Transactions on Smart Grid*, vol. 4, no. 2, pp. 816–827, June 2013.

[37] C. Qi, K. Wang, Y. Fu, G. Li, B. Han, R. Huang, and T. Pu, "A decentralized optimal operation of ac/dc hybrid distribution grids," *IEEE Transactions on Smart Grid*, vol. 9, no. 6, pp. 6095–6105, Nov. 2018.

[38] X. Liu, A. Aichhorn, L. Liu, and H. Li, "Coordinated control of distributed energy storage system with tap changer transformers for voltage rise mitigation under high photovoltaic penetration," *IEEE Transactions on Smart Grid*, vol. 3, no. 2, pp. 897–906, June 2012.

[39] S. Wang, S. Chen, L. Ge, and L. Wu, "Distributed generation hosting capacity evaluation for distribution systems considering the robust optimal operation of oltc and svc," *IEEE Transactions on Sustainable Energy*, vol. 7, no. 3, pp. 1111–1123, July 2016.

[40] P. M. S. Carvalho, P. F. Correia, and L. A. F. M. Ferreira, "Distributed reactive power generation control for voltage rise mitigation in distribution networks," *IEEE Transactions on Power Systems*, vol. 23, no. 2, pp. 766–772, May 2008.

[41] A. Samadi, R. Eriksson, L. Söder, B. G. Rawn, and J. C. Boemer, "Coordinated active power-dependent voltage regulation in distribution grids with pv systems," *IEEE Transactions on Power Delivery*, vol. 29, no. 3, pp. 1454–1464, June 2014.

[42] F. Nejabatkhah and Y. W. Li, "Overview of power management strategies of hybrid ac/dc microgrid," *IEEE Transactions on Power Electronics*, vol. 30, no. 12, pp. 7072–7089, Dec. 2015.

[43] R. Majumder, "A hybrid microgrid with dc connection at back to back converters," *IEEE Transactions on Smart Grid*, vol. 5, no. 1, pp. 251–259, Jan. 2014.

[44] A. A. Eajal, M. A. Abdelwahed, E. F. El-Saadany, and K. Ponnambalam, "A unified approach to the power flow analysis of ac/dc hybrid microgrids," *IEEE Transactions on Sustainable Energy*, vol. 7, no. 3, pp. 1145–1158, July 2016.

[45] H. Akagi, "Active harmonic filters," *Proceedings of the IEEE*, vol. 93, no. 12, pp. 2128–2141, Dec. 2005.

[46] B. Singh, K. Al-Haddad, and A. Chandra, "A review of active filters for power quality improvement," *IEEE Transactions on Industrial Electronics*, vol. 46, no. 5, pp. 960–971, Oct. 1999.

[47] B. Singh and J. Solanki, "A comparison of control algorithms for dstatcom," *IEEE Transactions on Industrial Electronics*, vol. 56, no. 7, pp. 2738–2745, July 2009.

[48] A. Ghosh and G. Ledwich, "Compensation of distribution system voltage using dvr," *IEEE Transactions on Power Delivery*, vol. 17, no. 4, pp. 1030–1036, Oct. 2002.

[49] H. Fujita and H. Akagi, "The unified power quality conditioner: the integration of series- and shunt-active filters," *IEEE Transactions on Power Electronics*, vol. 13, no. 2, pp. 315–322, Mar. 1998.

[50] E. R. Ronan, S. D. Sudhoff, S. F. Glover, and D. L. Galloway, "A power electronic-based distribution transformer," *IEEE Transactions on Power Delivery*, vol. 17, no. 2, pp. 537–543, Apr. 2002.

[51] X. She, A. Q. Huang, and R. Burgos, "Review of solid-state transformer technologies and their application in power distribution systems," *IEEE Journal of Emerging and Selected Topics in Power Electronics*, vol. 1, no. 3, pp. 186–198, Sep. 2013.

[52] J. E. Huber and J. W. Kolar, "Solid-state transformers: On the origins and evolution of key concepts," *IEEE Industrial Electronics Magazine*, vol. 10, no. 3, pp. 19–28, Sep. 2016.

[53] M. Liserre, G. Buticchi, M. Andresen, G. D. Carne, L. F. Costa, and Z. X. Zou, "The smart transformer: Impact on the electric grid and technology challenges," *IEEE Industrial Electronics Magazine*, vol. 10, no. 2, pp. 46–58, June 2016.

[54] S. Madhusoodhanan, A. Tripathi, D. Patel, K. Mainali, A. Kadavelugu, S. Hazra, S. Bhattacharya, and K. Hatua, "Solid-state transformer and mv grid tie applications enabled by 15 kv sic igbts and 10 kv sic mosfets based multilevel converters," *IEEE Transactions on Industry Applications*, vol. 51, no. 4, pp. 3343–3360, July 2015.

[55] L. Wang, D. Zhang, Y. Wang, B. Wu, and H. S. Athab, "Power and voltage balance control of a novel three-phase solid-state transformer using multilevel cascaded h-bridge inverters for microgrid applications," *IEEE Transactions on Power Electronics*, vol. 31, no. 4, pp. 3289–3301, Apr. 2016.

[56] J. D. O. Pacheco, D. D. A. Honório, and D. D. S. Oliveira, "An ac-dc isolated mmc-based structure suitable for mv sst traction applications," *IEEE Access*, vol. 7, pp. 106 395–106 406, 2019.

[57] H. Qin and J. W. Kimball, "Solid-state transformer architecture using ac-ac dual-active-bridge converter," *IEEE Transactions on Industrial Electronics*, vol. 60, no. 9, pp. 3720–3730, Sep. 2013.

[58] J. E. Huber, J. Miniböck, and J. W. Kolar, "Generic derivation of dynamic model for half-cycle dcm series resonant converters," *IEEE Transactions on Power Electronics*, vol. 33, no. 1, pp. 4–7, Jan. 2018.

[59] S. Falcones, R. Ayyanar, and X. Mao, "A dc-dc multiport-converter-based solid-state transformer integrating distributed generation and storage," *IEEE Transactions on Power Electronics*, vol. 28, no. 5, pp. 2192–2203, May 2013.

[60] D. Dujic, A. Mester, T. Chaudhuri, A. Coccia, F. Canales, and J. K. Steinke, "Laboratory scale prototype of a power electronic transformer for traction applications," in *Proceedings of the 2011 14th European Conference on Power Electronics and Applications*, Aug. 2011, pp. 1–10.

[61] J. E. Huber and J. W. Kolar, "Volume/weight/cost comparison of a 1mva 10 kv/400 v solid-state against a conventional low-frequency distribution transformer," in *2014 IEEE Energy Conversion Congress and Exposition (ECCE)*, Sep. 2014, pp. 4545–4552.

[62] A. Q. Huang, M. L. Crow, G. T. Heydt, J. P. Zheng, and S. J. Dale, "The future renewable electric energy delivery and management (freedm) system: The energy internet," *Proceedings of the IEEE*, vol. 99, no. 1, pp. 133–148, Jan. 2011.

[63] X. She, X. Yu, F. Wang, and A. Q. Huang, "Design and demonstration of a 3.6-kv-120-v/10-kva solid-state transformer for smart grid application," *IEEE Transactions on Power Electronics*, vol. 29, no. 8, pp. 3982–3996, Aug. 2014.

[64] L. F. Costa, G. D. Carne, G. Buticchi, and M. Liserre, "The smart transformer: A solid-state transformer tailored to provide ancillary services to the distribution grid," *IEEE Power Electronics Magazine*, vol. 4, no. 2, pp. 56–67, June 2017.

[65] F. Ruiz, M. A. Perez, J. R. Espinosa, T. Gajowik, S. Stynski, and M. Malinowski, "Surveying solid-state transformer structures and controls: Providing highly efficient and controllable power flow in distribution grids," *IEEE Industrial Electronics Magazine*, vol. 14, no. 1, pp. 56–70, Mar. 2020.

[66] A. Milczarek and M. Malinowski, "Comparison of classical and smart transformers impact on mv distribution grid," *IEEE Transactions on Power Delivery*, vol. 35, no. 3, pp. 1339–1347, June 2020.

[67] J. E. Huber and J. W. Kolar, "Applicability of solid-state transformers in today's and future distribution grids," *IEEE Transactions on Smart Grid*, vol. 10, no. 1, pp. 317–326, Jan. 2019.

[68] X. She, A. Q. Huang, F. Wang, and R. Burgos, "Wind energy system with integrated functions of active power transfer, reactive power compensation, and voltage conversion," *IEEE Transactions on Industrial Electronics*, vol. 60, no. 10, pp. 4512–4524, Oct. 2013.

[69] M. P. Kazmierkowski and L. Malesani, "Current control techniques for three-phase voltage-source pwm converters: a survey," *IEEE Transactions on Industrial Electronics*, vol. 45, no. 5, pp. 691–703, Oct. 1998.

[70] R. Teodorescu, M. Liserre, and P. Rodriguez, *Grid converters for photovoltaic and wind power systems*. John Wiley & Sons, 2011, vol. 29.

[71] A. Ghosh and G. Ledwich, *Power quality enhancement using custom power devices*. Springer Science & Business Media, 2012.

[72] S. Srikanthan, M. K. Mishra, and R. K. V. Rao, "Improved hysteresis current control of three-level inverter for distribution static compensator application," *IET Power Electronics*, vol. 2, no. 5, pp. 517–526, Sep. 2009.

[73] I. Syed and V. Khadkikar, "Replacing the grid interface transformer in wind energy conversion system with solid-state transformer," *IEEE Transactions on Power Systems*, vol. 32, no. 3, pp. 2152–2160, May 2017.

[74] R. Zhu, G. D. Carne, F. Deng, and M. Liserre, "Integration of large photovoltaic and wind system by means of smart transformer," *IEEE Transactions on Industrial Electronics*, vol. 64, no. 11, pp. 8928–8938, Nov. 2017.

[75] G. D. Carne, G. Buticchi, M. Liserre, and C. Vournas, "Load control using sensitivity identification by means of smart transformer," *IEEE Transactions on Smart Grid*, vol. 9, no. 4, pp. 2606–2615, July 2018.

[76] G. De Carne, G. Buticchi, M. Liserre, and C. Vournas, "Real-time primary frequency regulation using load power control by smart transformers," *IEEE Transactions on Smart Grid*, vol. 10, no. 5, pp. 5630–5639, Sep. 2019.

[77] G. De Carne, M. Langwasser, R. Zhu, and M. Liserre, "Smart transformer-based single phase-to-neutral fault management," *IEEE Transactions on Power Delivery*, vol. 34, no. 3, pp. 1049–1059, June 2019.

[78] Z. Zou, G. Buticchi, and M. Liserre, "Analysis and stabilization of a smart transformer-fed grid," *IEEE Transactions on Industrial Electronics*, vol. 65, no. 2, pp. 1325–1335, Feb. 2018.

[79] G. D. Carne, G. Buticchi, Z. Zou, and M. Liserre, "Reverse power flow control in a st-fed distribution grid," *IEEE Transactions on Smart Grid*, vol. 9, no. 4, pp. 3811–3819, July 2018.

[80] Z. Zou, G. Buticchi, and M. Liserre, "Grid identification and adaptive voltage control in a smart transformer-fed grid," *IEEE Transactions on Power Electronics*, vol. 34, no. 3, pp. 2327–2338, Mar. 2019.

[81] Z. Zou, M. Liserre, Z. Wang, and M. Cheng, "Modeling and stability analysis of a smart transformer-fed grid," *IEEE Access*, vol. 8, pp. 91 876–91 885, 2020.

[82] C. Kumar, R. Zhu, G. Buticchi, and M. Liserre, "Sizing and soc management of a smart-transformer-based energy storage system," *IEEE Transactions on Industrial Electronics*, vol. 65, no. 8, pp. 6709–6718, Aug. 2018.

[83] D. Shah and M. L. Crow, "Online volt-var control for distribution systems with solid-state transformers," *IEEE Transactions on Power Delivery*, vol. 31, no. 1, pp. 343–350, Feb. 2016.

[84] I. Syed, V. Khadkikar, and H. H. Zeineldin, "Loss reduction in radial distribution networks using a solid-state transformer," *IEEE Transactions on Industry Applications*, vol. 54, no. 5, pp. 5474–5482, Sep. 2018.

[85] X. She, A. Q. Huang, S. Lukic, and M. E. Baran, "On integration of solid-state transformer with zonal dc microgrid," *IEEE Transactions on Smart Grid*, vol. 3, no. 2, pp. 975–985, June 2012.

[86] X. Yu, X. She, X. Zhou, and A. Q. Huang, "Power management for dc microgrid enabled by solid-state transformer," *IEEE Transactions on Smart Grid*, vol. 5, no. 2, pp. 954–965, Mar. 2014.

[87] A. Agrawal, C. S. Nalamati, and R. Gupta, "Hybrid dc-ac zonal microgrid enabled by solid-state transformer and centralized esd integration," *IEEE Transactions on Industrial Electronics*, vol. 66, no. 11, pp. 9097–9107, Nov. 2019.

[88] X. Yu, X. She, X. Ni, and A. Q. Huang, "System integration and hierarchical power management strategy for a solid-state transformer interfaced microgrid system," *IEEE Transactions on Power Electronics*, vol. 29, no. 8, pp. 4414–4425, Aug. 2014.

[89] X. Gao, F. Sossan, K. Christakou, M. Paolone, and M. Liserre, "Concurrent voltage control and dispatch of active distribution networks by means of smart transformer and storage," *IEEE Transactions on Industrial Electronics*, vol. 65, no. 8, pp. 6657–6666, Aug. 2018.

[90] C. Kumar and M. Liserre, "A new prospective of smart transformer application: Dual microgrid (dmg) operation," in *IECON-41st Annu. Conf. IEEE Industrial Electronics Society*, Nov. 2015, pp. 004 482–004 487.

[91] C. Kumar and M. Liserre, "Operation and control of smart transformer for improving performance of medium voltage power distribution system," in *IEEE 6th Int. Symp. Power Electronics Distributed Generation Systems (PEDG)*, June 2015, pp. 1–6.

[92] C. Kumar, Z. Zou, and M. Liserre, "Smart transformer-based hybrid grid loads support in partial disconnection of mv/hv power system," in *IEEE Energy Conversion Congr. Expo. (ECCE)*, Sep. 2016, pp. 1–8.

[93] P. H. Divshali and L. Söder, "Improving pv dynamic hosting capacity using adaptive controller for statcoms," *IEEE Transactions on Energy Conversion*, vol. 34, no. 1, pp. 415–425, Mar. 2019.

[94] S. K. Chaudhary, J. M. Guerrero, and R. Teodorescu, "Enhancing the capacity of the ac distribution system using dc interlinks - a step toward future dc grid," *IEEE Transactions on Smart Grid*, vol. 6, no. 4, pp. 1722–1729, July 2015.

[95] J. K. Steinke, P. Maibach, G. Ortiz, F. Canales, and P. Steimer, "Mvdc applications and technology," in *PCIM Europe 2019; International Exhibition Conference Power Electronics, Intelligent Motion, Renewable Energy Energy Management*, May 2019, pp. 1–8.

[96] C. Kumar and M. K. Mishra, "A multifunctional dstatcom operating under stiff source," *IEEE Transactions on Industrial Electronics*, vol. 61, no. 7, pp. 3131–3136, July 2014.

[97] R. Kabiri, D. G. Holmes, B. P. McGrath, and L. G. Meegahapola, "Lv grid voltage regulation using transformer electronic tap changing, with pv inverter reactive power injection," *IEEE Journal of Emerging and Selected Topics in Power Electronics*, vol. 3, no. 4, pp. 1182–1192, Dec. 2015.

[98] M. Pradhan and M. K. Mishra, "Dual *p- q* theory based energy-optimized dynamic voltage restorer for power quality improvement in a distribution system," *IEEE Transactions on Industrial Electronics*, vol. 66, no. 4, pp. 2946–2955, Apr. 2019.

[99] J. M. Rey, M. Castilla, J. Miret, A. Camacho, and R. Guzman, "Adaptive slope voltage control for distributed generation inverters with improved transient performance," *IEEE Transactions on Energy Conversion*, vol. 34, no. 3, pp. 1644–1654, Sep. 2019.

[100] A. Camacho, M. Castilla, J. Miret, L. G. de Vicuña, and G. L. Miguel Andrés, "Control strategy for distribution generation inverters to maximize the voltage support in the lowest phase during voltage sags," *IEEE Transactions on Industrial Electronics*, vol. 65, no. 3, pp. 2346–2355, Mar. 2018.

[101] A. Camacho, M. Castilla, J. Miret, A. Borrell, and L. G. de Vicuña, "Active and reactive power strategies with peak current limitation for distributed generation inverters during unbalanced grid faults," *IEEE Transactions on Industrial Electronics*, vol. 62, no. 3, pp. 1515–1525, Mar. 2015.

[102] J. Krata and T. K. Saha, "Real-time coordinated voltage support with battery energy storage in a distribution grid equipped with medium-scale pv generation," *IEEE Transactions on Smart Grid*, vol. 10, no. 3, pp. 3486–3497, May 2019.

[103] H. Markiewicz and A. Klajn, "Standard EN 50160 - Voltage Characteristics in Public Distribution Systems," Tech. Rep., Jul. 2004.

[104] Central Electricity Authority, "Technical Standards for Connectivity to the Grid Regulations 2007 (Amendment) Regulations," Available at https://cea.nic.in/wp-content/uploads/2020/02/notified_regulations.pdf (2021/03/31).

[105] H. Akagi, E. Watanabe, and M. Aredes, *Instantaneous Power Theory and Applications to Power Conditioning*. Wiley, 2007.

[106] G. D. Carne, G. Buticchi, M. Liserre, P. Marinakis, and C. Vournas, "Coordinated frequency and voltage overload control of smart transformers," in *2015 IEEE Eindhoven PowerTech*, June 2015, pp. 1–5.

[107] S. Kotra and M. K. Mishra, "A supervisory power management system for a hybrid microgrid with hess," *IEEE Transactions on Industrial Electronics*, vol. 64, no. 5, pp. 3640–3649, May 2017.

[108] A. Q. Huang, "Medium-voltage solid-state transformer: Technology for a smarter and resilient grid," *IEEE Industrial Electronics Magazine*, vol. 10, no. 3, pp. 29–42, Sep. 2016.

[109] E. Vega-Fuentes and M. Denai, "Enhanced electric vehicle integration in the uk low-voltage networks with distributed phase shifting control," *IEEE Access*, vol. 7, pp. 46 796–46 807, 2019.

[110] P. Hasanpor Divshali and L. Söder, "Improving hosting capacity of rooftop pvs by quadratic control of an lv-central bss," *IEEE Transactions on Smart Grid*, vol. 10, no. 1, pp. 919–927, Jan. 2019.

[111] S. Hashemi and J. østergaard, "Efficient control of energy storage for increasing the pv hosting capacity of lv grids," *IEEE Transactions on Smart Grid*, vol. 9, no. 3, pp. 2295–2303, May 2018.

[112] F. Tamp and P. Ciufo, "A sensitivity analysis toolkit for the simplification of mv distribution network voltage management," *IEEE Transactions on Smart Grid*, vol. 5, no. 2, pp. 559–568, Mar. 2014.

[113] R. Tonkoski, L. A. C. Lopes, and T. H. M. El-Fouly, "Coordinated active power curtailment of grid connected pv inverters for overvoltage prevention," *IEEE Transactions on Sustainable Energy*, vol. 2, no. 2, pp. 139–147, Apr. 2011.

[114] R. G. Wandhare and V. Agarwal, "Reactive power capacity enhancement of a pv-grid system to increase pv penetration level in smart grid scenario," *IEEE Transactions on Smart Grid*, vol. 5, no. 4, pp. 1845–1854, July 2014.

[115] P. Kundur, *Power System Stability and Control*. McGraw-Hill.

[116] A. Gupta, S. Doolla, and K. Chatterjee, "Hybrid ac-dc microgrid: Systematic evaluation of control strategies," *IEEE Transactions on Smart Grid*, vol. 9, no. 4, pp. 3830–3843, July 2018.

[117] T. M. Haileselassie and K. Uhlen, "Impact of dc line voltage drops on power flow of mtdc using droop control," *IEEE Transactions on Power Systems*, vol. 27, no. 3, pp. 1441–1449, Aug. 2012.

[118] Y. Wang, W. Wen, C. Wang, H. Liu, X. Zhan, and X. Xiao, "Adaptive voltage droop method of multiterminal vsc-hvdc systems for dc voltage deviation and power sharing," *IEEE Transactions on Power Delivery*, vol. 34, no. 1, pp. 169–176, Feb. 2019.

[119] Mvdc plus - the grid connector. [Online]. Available: https://new.siemens.com/global/en/products/energy/medium-voltage/solutions/mvdc.html

[120] R. Bernacchi, "Mvdc and grid interties : enabling new features in distribution , sub-transmission and industrial networks." [Online]. Available: https://search-ext.abb.com/library/Download.aspx?DocumentID=9AKK107680A0196&LanguageCode=en&DocumentPartId=&Action=Launch

[121] P. Khamphakdi, M. Nitta, M. Hagiwara, and H. Akagi, "Zero-voltage ride-through capability of a transformerless back-to-back system using modular multilevel cascade converters for power distribution systems," *IEEE Transactions on Power Electronics*, vol. 31, no. 4, pp. 2730–2741, Apr. 2016.

[122] D. Sciano, A. Raza, R. Salcedo, M. Diaz-Aguilo, R. E. Uosef, D. Czarkowski, and F. de León, "Evaluation of dc links on dense-load urban distribution networks," *IEEE Transactions on Power Delivery*, vol. 31, no. 3, pp. 1317–1326, June 2016.

[123] L. Zhang, J. Liang, W. Tang, G. Li, Y. Cai, and W. Sheng, "Converting ac distribution lines to dc to increase transfer capacities and dg penetration," *IEEE Transactions on Smart Grid*, vol. 10, no. 2, pp. 1477–1487, Mar. 2019.

[124] K. Mahmud, M. J. Hossain, and G. E. Town, "Peak-load reduction by coordinated response of photovoltaics, battery storage, and electric vehicles," *IEEE Access*, vol. 6, pp. 29 353–29 365, 2018.

[125] S. Inoue and H. Akagi, "A bidirectional dc-dc converter for an energy storage system with galvanic isolation," *IEEE Transactions on Power Electronics*, vol. 22, no. 6, pp. 2299–2306, Nov. 2007.

LIST OF PAPERS BASED ON THESIS

PUBLICATIONS IN REFEREED JOURNALS

1. Hrishikesan V M, Dwijasish Das, Chandan Kumar, Hoay Beng Gooi, Saad Mekhilef and Xiaoqiang Guo, "Increasing Voltage Support Using Smart Power Converter Based Energy Storage System and Load Control" *IEEE Transactions on Industrial Electronics*, 2020, DOI: 10.1109/TIE.2020.3042165.

2. Hrishikesan V M, Anup Kumar Deka, and Chandan Kumar, "Capacity Enhancement of a Radial Distribution Grid Using Smart Transformer," *IEEE Access* , vol. 8, pp. 72411-72423, 2020.

3. Hrishikesan V M, Chandan Kumar and Marco Liserre, "An MVDC Based Meshed Hybrid Microgrid Enabled Using Smart Transformers," Accepted for publication in *IEEE Transactions on Industrial Electronics*, 2021.

4. Hrishikesan V M and Chandan Kumar "Operation of Meshed Hybrid Microgrid During Adverse Grid Conditions with Storage Integrated Smart Transformer," Accepted for publication in *IEEE Open Journal of the Industrial Electronics Society*, 2021.

PUBLICATIONS IN REFEREED CONFERENCES

1. Hrishikesan V M and Chandan Kumar, "Smart Transformer Based Meshed Hybrid Microgrid with MVDC Interconnection,"' *46th Annual Conference of IEEE Industrial Electronics Society (IECON)*, Singapore, 18-21 October, 2020, pp. 4961-4966.

2. Hrishikesan V M, Dwijasish Das and Chandan Kumar, "A Flexible and Coordinated Voltage Control Strategy for Smart Transformer," *IEEE International Conference on Power Electronics, Drives and Energy Systems (PEDES)*, IIT Madras, Chennai, India, 18-21 December, 2018, pp. 1-6.

3. Hrishikesan V M, Chandan Kumar and Marco Liserre, "Flexible Power Transfer in Smart Transformer Interconnected Microgrids," *44th Annual Conference of the IEEE, Industrial Electronics Society (IECON)*, Washington D.C., USA, 21-23 October, 2018, pp. 5535-5540.

4. Hrishikesan V M and Chandan Kumar, "Power Management in a ST Integrated Medium Voltage Grid," *8th National Power Electronics Conference (NPEC)*, Pune, India, 18-20 December, 2017, pp. 141-146 .

5. Hrishikesan V M, Chandan Kumar and Marco Liserre, "Voltage Quality Improvement in Smart Transformer Integrated Distribution Grid," *43rd Annual Conference of the IEEE, Industrial Electronics Society (IECON)*, Beijing, China, 29 October - 1 November, 2017, pp. 5386-5391.